

Tunable Lasers on a Polymer-Based Hybrid Photonic Integration Platform

vorgelegt von

Ingeniero de Telecomunicación

David de Felipe Mesquida

ORCID: 0000-0002-6050-7626

von der Fakultät IV – Elektrotechnik und Informatik

der Technischen Universität Berlin

zur Erlangung des akademischen Grades

Doktor der Ingenieurwissenschaften

– Dr.-Ing. –

genehmigte Dissertation

Promotionsausschuss:

Vorsitzender: Prof. Dr. rer. nat. Günther Tränkle, TU Berlin

Gutachter: Prof. Dr.-Ing. Dr. h. c. Klaus Petermann, TU Berlin

Prof. Dr. rer. nat. Martin Schell, TU Berlin

Prof. Dr.-Ing. Franko Küppers, Skolkovo Institute of Science and Technology

Tag der wissenschaftlichen Aussprache: 21. November 2019

Berlin 2020

Eidesstattliche Erklärung

Hiermit erkläre ich an Eides statt, dass ich die Dissertation selbstständig verfasst habe. Alle benutzten Quellen und Hilfsmittel sind aufgeführt und die Angaben zu den Eigenanteilen bei Co-Autorschaft sind zutreffend.

Berlin, den 17 Juni 2020

Zusammenfassung

Durchstimmbare Halbleiterlaser als miniaturisierte optische Quellen mit der Fähigkeit bei verschiedenen Wellenlängen zu emittieren sind Schlüsselemente in diversen Anwendungen, von Telekommunikation bis Sensorik. Viele Ansätze wurden in der Literatur untersucht um integrierte Lösungen anzubieten, die sowohl ihre Miniaturisierung als auch ihre Kointegration mit anderen optischen Funktionalitäten in photonischen integrierten Schaltkreisen ermöglichen. Diese integrierten Elemente beruhen typischerweise auf einer kontrollierten Änderung des Brechungsindizes der abstimmbaren Abschnitte durch Ladungsträgerinjektion oder dem thermo-optischen Effekt. Eine weitere Methode ist die Veränderung der physikalischen Länge des Resonators unter Verwendung mikromechanischer Systeme.

In dieser Arbeit wird die Implementierung von im C-band durchstimmbaren Lasern auf der Grundlage eines hybriden photonischen Integrationsansatzes untersucht, der aktive Abschnitte auf InP-Basis und thermooptisch abstimmbare Strukturen auf Polymerbasis kombiniert. Wellenleiter auf Polymerbasis ermöglichen die Implementierung hocheffizienter, abstimmbarer, wellenlängenselektiver Filter und Reflektoren, die die positiven Eigenschaften der Polymermaterialien wie ihren großen thermo-optischen Koeffizienten und ihre geringe Wärmeleitfähigkeit nutzen.

Die betrachtete Implementierung ist ein Distributed Bragg Reflector (DBR)-Laser, und es werden Durchstimmbarkeiten von 20 nm demonstriert. Die Designstrategien des DBR-Lasers werden untersucht, um entweder seine Hochgeschwindigkeitsmodulationseigenschaften, seine Linienbreite oder die maximal erreichbare kontinuierliche Abstimmung zu optimieren. Eine erste Design-Implementierung für die Hochgeschwindigkeitsmodulation zeigt eine Modulationsbandbreite von 8.6 GHz und Ausgangsleistungen von mehr als 9.5 dBm. Ein zweites Device, welches auf schmale Linienbreiten ausgerichtet ist, zeigt Linienbreitenwerte bis zu 130 kHz und Ausgangsleistungen von 8.45 dBm. Ein drittes Design, das auf maximal erreichbare kontinuierliche Durchstimmbarkeit abzielt, zeigt die Möglichkeit einer Durchstimmung von 9 nm ohne Modensprung.

Auch die Aspekte der Wellenlängeneinstellung und -stabilisierung werden behandelt, was zeigt, dass Wellenlängenstabilisierungsgenauigkeiten von ± 2.5 GHz erreicht werden können. Zusätzlich werden erste Zuverlässigkeitstests vorgestellt, die die potenzielle Langzeitzuverlässigkeit von Abstimmbereichen von 20 nm zeigen.

Schließlich wird die Anwendbarkeit der vorgeschlagenen abstimmbaren Laserimplementierung in vier konkreten Anwendungsbereichen untersucht: wellenlängenmultiplex (WDM) passiven optischen Netzwerken für Glasfaser-Hausanschlüsse und 5G-Netze, Kohärente WDM-Metro/Kern- und Rechenzentrumsnetze, photonische Erzeugung der ultrahochfrequenten drahtlosen Verbindungen für zukünftigen 5G, und die photonische Erzeugung von Terahertz (THz) Frequenzdurchstimmungen für Spektroskopiesysteme.

Abstract

Semiconductor tunable lasers as miniaturized optical sources with the agility to operate at different wavelengths are key elements in a large variety of applications, ranging from telecom to sensing. Many approaches have been investigated in literature in order to offer integrated solutions that allow both their miniaturization and their co-integration with other optical functionalities in photonic integrated circuits. Those integrated devices typically rely on a controlled change in the refractive index of the tunable sections by means of carrier injection or the thermo-optical effect, or on a change of the physical length of the resonator using micromechanical systems.

This work investigates the implementation of C-band tunable lasers based on hybrid photonic integration approach combining InP-based active sections and polymer-based thermo-optically tunable structures. Polymer-based waveguides allow implementing highly-efficient tunable wavelength selective filters and reflectors using beneficial features of the polymer materials such as their large thermo-optical coefficient and low thermal conductivity.

The cavity structure considered in this work is a three-section distributed Bragg reflector (DBR) laser, whereby tunabilities of 20 nm are demonstrated. The design strategies of the DBR laser in order to optimize either its high-speed modulation characteristics, linewidth, or maximum achievable continuous tuning, are investigated. A first design targeting high-speed modulation shows a modulation bandwidth of 8.6 GHz and output powers of more than 9.5 dBm. A second device targeting narrow linewidths shows linewidth values as low as 130 kHz, and output powers of 8.45 dBm. A third design targeting maximum achievable swept-tuning provides the possibility of 9 nm tuning without the occurrence of mode-hops.

The wavelength setting and stabilization aspects are also covered, showing that wavelength accuracies of ± 2.5 GHz can be achieved. Additionally, preliminary reliability tests are presented, showing the potential long-term reliability of tuning ranges of 20 nm.

Finally, the applicability of the proposed tunable laser implementation in different application fields is investigated. The possibility of transmitting at 10 Gb/s over fiber links of 11 km shows its potential usability in wavelength-division-multiplexed (WDM) passive optical networks for Fiber-to-the-home and future 5G networks. Furthermore, hybrid photonic integrated circuits comprising the DBR lasers co-integrated with I/Q Mach-Zehnder modulators allow for high-order coherent modulation formats such as 64-QAM at 25 GBaud, demonstrating the potential of the DBR lasers as key optical building blocks in coherent optoelectronic transceivers for WDM metro/core and data-center networks. Additionally, the DBR lasers are used for the photonic generation of terahertz (THz) carriers for ultra-high-frequency wireless links at 18 Gb/s data rates, showing its potential use in the high-speed wireless links envisioned in future 5G networks. Finally, the DBR laser are tested as continuously tuned sources for the photonic generation of THz frequency-sweeps for spectroscopy systems, proving the possibility of achieving frequency-scans along more than 1 THz.

Contents

1.	Introduction.....	1
1.1	Why and where are tunable lasers needed?.....	1
1.2	Principle and state of the art of semiconductor tunable lasers	3
1.3	Scope of this work	5
1.4	Structure of this work.....	6
2.	Theory of External Cavity Semiconductor Tunable Lasers.....	7
2.1	General model of an external cavity tunable laser	7
2.2	Round-trip conditions	7
2.3	Principles of tuning	10
2.3.1	Tuning of the frequency-selective reflector	11
2.3.2	Tuning of the longitudinal modes	12
2.3.3	Discontinuous and continuous tuning	13
2.4	Steady-state characteristics	14
2.4.1	Rate equations	14
2.4.2	Threshold current	16
2.4.3	Output power.....	17
2.4.4	Side-mode suppression ratio	17
2.5	Dynamic characteristics	18
2.5.1	Re-visiting the rate equations.....	18
2.5.2	Relaxation oscillation and damping rate	20
2.5.3	Relative intensity noise	22
2.5.4	Chirp	23
2.5.5	Linewidth	25
2.6	Conclusions of the chapter	26
3.	Principles of III-V/Polymer Tunable DBR Lasers.....	29
3.1	Device structure and operation principle	29
3.2	External cavity laser model.....	30
3.2.1	Basic theory of Bragg gratings.....	31

3.2.1	Mirror losses, longitudinal modes, and mode spacing	33
3.2.2	External cavity parameters A and B	34
3.3	InP-based multi-quantum-well active sections	35
3.4	Polymer-based thermo-optically tunable sections	36
3.4.1	Fabrication	38
3.4.2	Tunable Bragg gratings	38
3.4.3	Phase shifters	40
3.5	III-V/polymer hybrid integration	41
3.5.1	Description of the automatic alignment process	41
3.5.2	Coupling losses and alignment tolerances	41
3.6	Conclusions of the chapter	43
4.	Design Strategies and Performance of III-V/Polymer Tunable DBR Lasers	45
4.1	High-speed direct modulation	45
4.1.1	Output power and tuning behavior	47
4.1.2	Basic small-signal modulation performance	48
4.1.3	Effect of detuning	50
4.1.4	Considerations towards optimization of the modulation performance	52
4.2	Narrow linewidth	52
4.2.1	Output power and tuning behavior	52
4.2.2	Linewidth and effect of detuning	54
4.2.3	Considerations towards further reduction of the linewidth	56
4.3	Enhanced continuous tuning	57
4.3.1	Theory of continuous tuning in thermo-optically tunable DBR lasers	58
4.3.2	Experimental results	61
4.4	Conclusions of the chapter	63
5.	Wavelength Setting, Stabilization, and Device Reliability	65
5.1	Effect of temperature variations on the lasing wavelength	65
5.2	Wavelength correction under temperature variations	67
5.3	The voltage drop in the active section as a monitoring signal	68
5.4	Method for wavelength setting and stabilization	69
5.5	Experiments on wavelength stabilization	71
5.5.1	Stabilization at a constant device temperature	72

5.5.2	Uncooled stabilization in a laboratory environment	72
5.5.3	Stabilization under forced temperature variations	72
5.6	Initial studies on long-term reliability.....	73
5.7	Conclusions of the chapter	75
6.	Study of Performance in Different Application Scenarios.....	77
6.1	Passive optical networks for FTTH and 5G	77
6.2	Coherent data-center and metro/core networks.....	78
6.2.1	Tunable I/Q transmitter	78
6.2.2	Re-configurable multi-wavelength I/Q transmitter	80
6.3	THz communications for next-generation wireless systems.....	82
6.4	THz spectroscopy systems	86
6.5	Conclusions of the chapter	87
7.	Conclusions and Outlook.....	89
7.1	Conclusions.....	89
7.2	Outlook	90
A.	List of Patents and Publications	91
A.1.	Patents.....	91
A.2.	Articles in journals	91
A.3.	Conference contributions	92
B.	List of Abbreviations	95
C.	List of Symbols	99
D.	List of Physical Constants	105
E.	Parameters considered for the InGaAsP multi-quantum well active section.....	107
References	109

1. Introduction

With the rapid growth of the services offered over the internet, and in the advent of the holistic interconnection paradigm that is envisioned in the future 5G Networks, the data volumes on the internet are forecasted to amount to between 2 and 4 Zettabytes per year by 2020 [1]. Furthermore, 5G Networks are envisioned to provide disruptive changes in the industry, giving rise to a new industrial revolution coined by the term Industry 4.0 [2]. These changes in the industry will not only be enabled by the ultra-broadband communications that will allow exchanging large amounts of data in the production processes, but also by means of novel sensing methods to be installed in the production lines in order to acquire that data. In this context, integrated photonics are envisioned to play a crucial role both in the ultra-high speed optoelectronic transceivers demanded to cope with the expected data volumes, and in the conceptualization of novel optical sensing methods.

1.1 Why and where are tunable lasers needed?

Within the photonic integrated circuits (PICs) that are envisioned to enable 5G networks and Industry 4.0, the need of semiconductor tunable lasers as miniaturized optical sources in the C-band (1550 nm) with the agility to operate at different wavelengths can be identified in different scenarios, some of which are reviewed in the following.

A key milestone for the next-generation 5G communication networks is the deployment of Fibre-to-the-home (FTTH). In order to cope with the requirements of the ever increasing bandwidth-hungry services provided to the end users, wavelength-division multiplexed (WDM) passive optical networks (PONs) till the end-user locations have attracted a great deal of attention due to their ease of scalability and their flexibility in providing different data rates and protocols [3]. Within this technology, optoelectronic transceivers at the end-user side with the flexibility to operate at different wavelengths allows simplifying the network operation, reducing installation costs, and keeping the maintenance efforts under control [4]. In this context, low-cost, power-efficient and reliable tunable laser sources with the capability of high-speed data modulation are envisioned to be key enabling components in those transceivers.

Furthermore, in 5G Networks, wireless data transmission of above 10 Gbit/s is targeted as one of the key goals [5]. Merging optics and wireless systems provides benefits in the network infrastructure such as exploiting the bandwidths achievable with WDM-PONs in the links between the radio units and the optical network, as well as between different radio units [6, 7]. In this context, tunable lasers with high-speed data modulation capability are again envisioned to be the key elements in optoelectronic transceivers [8]. Additionally, the high data rates targeted in the wireless links (i.e. high bandwidths of the transmitted signals) requires an increase in the carrier frequencies, and a free region of the electromagnetic spectrum where multiple wireless channels can be transmitted. The use of the Terahertz (THz) spectrum range (300 GHz – 3 THz), which is still unexplored for wireless communication systems, is an attractive alternative to cover those two needs [9]. The photonic generation of THz signals by means of photomixing allows

1. Introduction

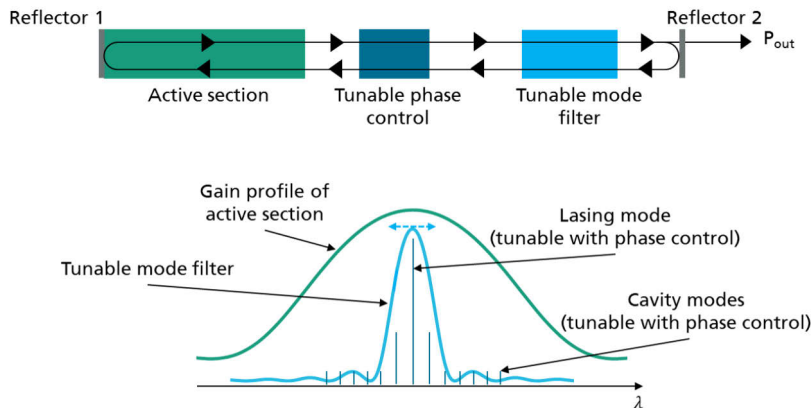


Figure 1.1. General schematic of a single-mode tunable laser.

overcoming the limitations of electronics for generating frequencies in the millimeter wave range and beyond. Photonics make available high-speed optoelectronic components developed in the last decades for optical communications such as modulators and photodiodes, which can be combined in PICs together with laser sources for the integration of photonic wireless transmitters. In those transmitters, the use of tunable lasers can enable to freely-adjust the frequency of the wireless carrier, what would provide to the wireless scheduling algorithms the flexibility to allocate a frequency available at the time of transmission.

Moving the focus to the core of the Internet, the nodes in metro/regional core networks and data centers will need to deal with data streams in the order of Tb/s and beyond [10]. In order to overcome this challenge, exploiting dense WDM (DWDM) in edge-switches and data-center gateways is an attractive option, since in combination with high-order coherent modulation formats, high aggregated data rates can be achieved. In this context, tunable lasers are envisioned to be key elements in metro/core and datacenter transceivers, since they provide the possibility to transmit and/or detect signals in freely-adjustable DWDM channels. Beyond tunability, the phase noise (and hence linewidth) of those tunable lasers is a crucial parameter in this application scenario, since sources with low phase noise allow exploiting high-order coherent modulation formats with high spectral efficiency such as quadrature phase-shift keying (QPSK) and quadrature amplitude modulation (QAM).

Finally, PICs are envisioned to allow for new optical measurement methods that can enable the Industry 4.0. In the concrete case of optical spectroscopy, the possibility of using tunable lasers to perform continuous wavelength scans allows extracting the spectral fingerprint of different materials and gases. In this context, integrated tunable lasers that provide the possibility of continuous wavelength sweeps play a key role. A special mention can be made to the spectroscopy systems operating at THz frequencies, which have attracted a great deal of attention in applications such as biology and medical sciences, non-destructive testing, security, quality control of food and agricultural products, and global environmental monitoring [11]. With the availability of photonic sources for the THz generation operating at the C-band, miniaturized tunable lasers in combination with other components developed for telecom applications can potentially contribute to the miniaturization of the sensing systems, making them more attractive for their deployment on production lines.

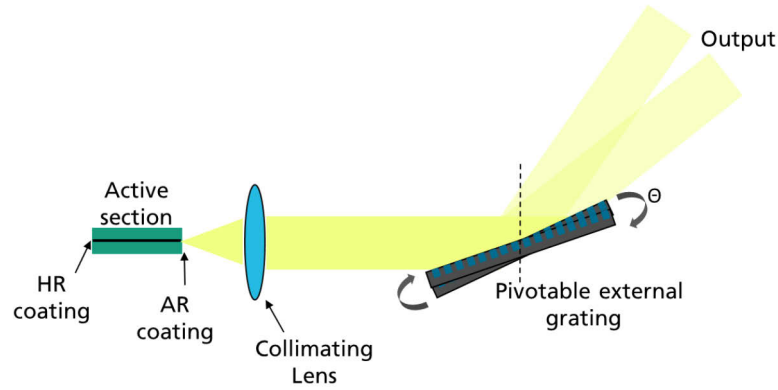


Figure 1.2 Littrow configuration for external-cavity semiconductor tunable lasers.

1.2 Principle and state of the art of semiconductor tunable lasers

Even though many distinct implementations for tunable lasers have been reported in literature, the general structure of a single-mode tunable laser can be described by the schematic shown in Figure 1.1. A semiconductor active section with a high-reflection (HR) on its rear-end (Reflector 1) provides optical gain. The front-end of the active section features an anti-reflection (AR coating), and is faced towards a passive

TABLE 1.1. STATE OF THE ART OVERVIEW OF INTEGRATED SEMICONDUCTOR TUNABLE LASERS OPERATING IN THE C-BAND

INSTITUTION / REFERENCE	TECHNOLOGY	TUNING (NM)	TUNING METHOD	OUTPUT POWER (DBM)	LINEWIDTH (KHZ)	f_{3dB} (GHZ)	FOOTPRINT (MM ²)
Infinera [15, 16]	InP	50	(Not specified)	-	200	-	-
NEC [21]	III-V/Si	65	Thermo-optical	20	15	-	4.5 x 3.5
UCSB [22]	III-V/Si	40	Thermo-optical	10	200	-	7 x 1
Nokia Bell Labs [23]	III-V/Si	95	Thermo-optical	13	550	-	-
LioniX [24]	III-V/Si ₃ N ₄	81	Thermo-optical	11	65	-	-
TU Darmstadt [18, 19]	InP (VCSEL)	60	MEMS	1.5	98000	7	0.42 x 0.42
ETRI [26, 27]	III-V/polymer	11.2	Thermo-optical	4.2	-	8	-

1. Introduction

section. This passive section comprises a tunable phase shifter that allows tuning the longitudinal modes, a tunable mode-selective filter that ensures single-mode operation and can be tuned to different longitudinal modes, and a second reflector at its end to close the resonator (Reflector 2).

A well-known implementation of tunable lasers is the so-called Littrow configuration [12], depicted in Figure 1.2. These devices are based on an external-cavity diode laser (ECDL) configuration, and rely on an active section coupled by means of free-space optics to a pivotable external grating acting both as a tunable mode filter and reflector. By means of rotating the grating, the central wavelength of the wavelength filter is modified, and hence the lasing wavelength tuned. This configuration, together with a slight implementation variation known as the Littman-Metcalf configuration [13], are the basis of most of the commercially-available ECDLs.

Many approaches have followed in order to offer an integrated solution that allows miniaturization of tunable lasers operating in the C-band, as well as their co-integration with other optical functionalities in PICs. Those integrated devices typically rely on a controlled change in the refractive index of the tunable sections by means of carrier injection or the thermo-optical effect, or on a change of the physical length of the resonator using micromechanical systems (MEMS). During the most recent years, two integration methods have focused the most attention: monolithically integrated tunable lasers on III-V semiconductors such as InP, and hybrid-integrated lasers, which combine III-V active sections with passive tunable filters on e.g. Si, SiN, and polymer materials. In Table 1.1, an overview of the state of the art of monolithic and hybrid tunable lasers is shown. Monolithic implementations provide the advantage that large numbers of tunable laser can be fabricated on the same wafer, whereas the hybrid photonic integration allows combining III-V active sections with other materials that are attractive for the implementation of the tunable sections, not only regarding performance metrics such as tuning properties or propagation losses, but also regarding processability and finally cost.

Typical designs for monolithically integrated tunable lasers are the so-called multi-section distributed Bragg reflector (DBR) lasers, which rely on tunable grating structures as wavelength filters and reflectors [14]. The company Infinera has integrated such lasers into coherent transmitter and receiver PICs, showing a tuning range of 50 nm and linewidths narrower than 200 kHz [15, 16]. Tunable vertical-cavity surface-emitting lasers (VCSELs) are another possible monolithic implementation, which make use of a membrane Bragg reflector which is tunable using a micromechanical system (MEMS) [17]. Those devices have shown tuning ranges of around 60 nm, and a 3-dB small signal modulation bandwidth f_{3dB} of around 7 GHz which can enable 10 Gb/s direct modulation [18]. Nevertheless, VCSELs present some limitations regarding output power (1.5 dBm [18]) and achievable linewidth (98 MHz [19]) due to the short active sections and resonator lengths achievable in integrated vertical cavities.

Hybrid integrated tunable lasers based on silicon photonics have attracted a great deal of attention during the recent years. III-V active sections can be coupled to the silicon photonics (SiP) chip by means of die bonding or wafer bonding [20]. The SiP chips provide the tunability, where the tunable wavelength selective mirrors are achieved by means of thermo-optically tunable micro-ring resonators or gratings structures. The use of micro-ring resonators with high Q-factors allows for long photon lifetimes and hence narrow linewidth. Following this approach, the Japanese company NEC Corp. has demonstrated a tunable laser with an output power of 20 dBm (assisted by a booster at the output), a tuning range of 65 nm, and optical linewidths narrower than 15 kHz along the tuning range [21]. The University of California Santa

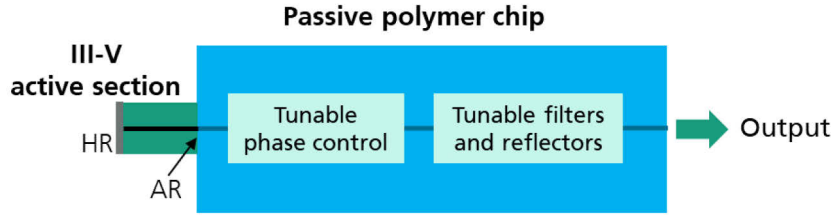


Figure 1.3. Hybrid III-V/polymer integrated tunable laser.

Barbara (UCSB) has also demonstrated tunable lasers using a similar approach, showing output powers of around 10 dBm, tuning ranges around 40 nm, and laser linewidths narrower than 200 kHz [22]. Nokia Bell Labs has also demonstrated a III-V/Si tunable laser implementation showing 95 nm tunability along C and L band, 13 dBm output power, and linewidths of 550 kHz [23].

Hybrid integration of tunable lasers using platforms other than silicon photonics have also been investigated. The Dutch company LioniX has demonstrated tunable lasers comprising III-V gain sections coupled to a TriPlexTM chip comprising thermo-optically tunable micro-ring resonators on low-loss waveguides (<0.2 dB/cm) [24]. An output power of 16 mW (~ 11.8 dBm), a tuning range of 50 nm, and linewidths as narrow as 65 kHz, have been demonstrated [24]. Furthermore, the South Korean institute ETRI demonstrated for the first time in 2008 a DBR tunable laser combining a III-V active section and a thermo-optically tunable polymer-based Bragg reflector [25]. Tuning ranges of 11 nm have been demonstrated, showing f_{3dB} of around 8 GHz at 1550 nm and capability for 10 Gb/s direct modulation [26, 27], and maximum output powers of 2.6 mW (4.2 dBm) [26].

1.3 Scope of this work

This work investigates the III-V/polymer hybrid photonic integration of DBR C-band tunable lasers following a similar approach as the one demonstrated by ETRI. The proposed implementation is based on Fraunhofer HHI's polymer-based hybrid photonic integration platform, namely PolyBoard [28]. A schematic of the investigated approach is shown in Figure 1.3. The studied approach comprises an InP-based multi-quantum well (MQW) active section featuring an HR coating at its rear-end and AR coating against polymer on its front-end, which is end-fire coupled to a polymer chip featuring a thermo-optically tunable phase shifter and a Bragg grating that acts simultaneously as a wavelength filter and reflector. Two characteristics of polymers make them very attractive candidates for the implementations of thermo-optically tunable structures. Firstly, polymer materials show a fairly high thermo-optical coefficient of around $-1.1 \times 10^{-4} \text{ K}^{-1}$ [29], which is in the same order of magnitude than InP ($2 \times 10^{-4} \text{ K}^{-1}$ [30]) and Si ($1.86 \times 10^{-4} \text{ K}^{-1}$ [31]), and one order of magnitude larger than that of SiN ($2.51 \times 10^{-5} \text{ K}^{-1}$ [32]). Secondly, the low thermal-conductivity of polymer materials ($0.29 \text{ Wm}^{-1}\text{K}^{-1}$ [33]) is two orders of magnitude lower than that of InP ($68 \text{ Wm}^{-1}\text{K}^{-1}$ [34]) and SiN ($30 \text{ Wm}^{-1}\text{K}^{-1}$ [35]), and three orders of magnitude lower than that of Si ($156 \text{ Wm}^{-1}\text{K}^{-1}$ [31]). This makes polymers ideal candidates for highly-efficient thermo-optical tuning due to the high heat confinements achievable.

The goal of this work is to study their design strategy and performance when targeting high-speed direct modulation behavior, narrow linewidth, and wavelength-swept tuning. Besides that, this work aims to throw some light on other important practical aspects of tunable lasers such as wavelength stabilization and device reliability. Additionally, this work aims providing an initial study of applicability of the proposed

1. Introduction

implementation in different application scenarios relevant to the future 5G Networks and to the Industry 4.0.

1.4 Structure of this work

Chapter 2 introduces a general theory of external-cavity semiconductor tunable lasers, which can be applied to any material platform and to any tunable laser implementation. Starting from the round trip conditions, the principles of tuning are introduced, and the steady-state and dynamic characteristics described.

Chapter 3 describes the operation principle and model of a III-V/polymer DBR tunable laser. The active sections and polymer-based thermo-optically tunable structures are introduced. The III-V/polymer hybrid integration method is described, and the coupling between active and passive sections evaluated.

In Chapter 4, the design strategies and performance of the DBR tunable laser when targeting high-speed direct-modulation, linewidth reduction and, maximum achievable continuous wavelength tuning, are studied. An outlook on optimization potential in all those aspects is provided.

Chapter 5 is devoted to theoretical and experimental aspects regarding the wavelength setting and stabilization of the III-V/polymer DBR tunable lasers, and initial experiments on long-term tuning reliability.

Chapter 6 covers preliminary application studies of the DBR tunable lasers on PONs, coherent communication systems for metro/core and data-center networks, photonic generation of wireless links, and THz spectroscopy systems. Different PICs comprising the DBR tunable laser as key building block are presented.

Finally, Chapter 7 concludes this work with a discussion of the results and an outlook.

2. Theory of External Cavity

Semiconductor Tunable Lasers

This chapter is devoted to the theory that describes the operation principle and lasing behavior of tunable lasers. A general model for external cavity semiconductor tunable lasers, which aims describing any tunable laser implementation on any material system, is presented, and the key aspects of frequency/wavelength tuning described. Furthermore, the methodology to describe static and dynamic characteristics of external cavity tunable lasers is developed.

2.1 General model of an external cavity tunable laser

The general schematic of a tunable laser introduced in Figure 1.1 can be modelled as an external cavity semiconductor laser as shown in Figure 2.1. An active section with a length L_a featuring on its rear-end an HR coating with reflectance r_1 is coupled with a power coupling efficiency α_c to a passive section with a length L_p , which features at its end a frequency dependent reflector with a complex reflectance $r_2(\omega)$. Being ω the angular frequency, $r_2(\omega)$ can be expressed in terms of amplitude and phase as

$$r_2(\omega) = |r_2(\omega)|e^{-j\phi_{r_2(\omega)}}. \quad (2.1)$$

This reflectance on the passive side of the cavity accounts for the mode-selective filtering and reflection, and is tunable in the frequency by means of a certain mechanism. Notice that the different conceivable tunable laser structures rely on different implementations of $r_2(\omega)$. In this work, it will be considered that no reflections take place at the interface between the active and passive sections, which is a good approximation for implementations that feature an AR coating at the front-end of the active section.

2.2 Round-trip conditions

In order to find the round-trip conditions, as well as for the theoretical developments presented in the following sections to discuss the steady-state and dynamic characteristics of external cavity lasers, it will be considered that the complex time- and space-varying electrical fields are transverse-electric (TE) polarized plane waves confined in the x (vertical) and y (horizontal) axis propagating along the z axis with a certain propagation constant β , taking the following general form

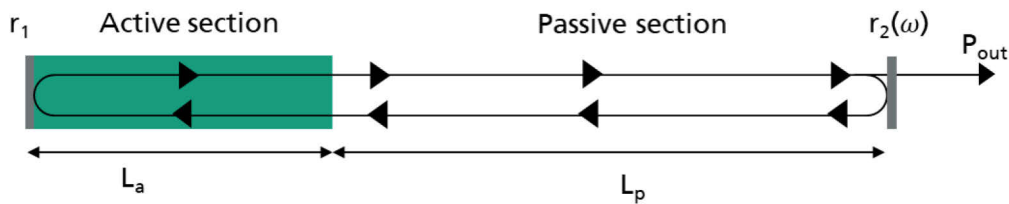


Figure 2.1. Model of an external cavity tunable laser with an arbitrary tunable frequency-selective reflector $r_2(\omega)$.

2. Theory of External Cavity Semiconductor Tunable Lasers

$$\vec{E}(x, y, z, t) = \hat{y} E_0 \psi(x, y) e^{j(\omega t - \beta z)}, \quad (2.2)$$

being \hat{y} the unitary vector in the y axis indicating the TE polarization, E_0 the electrical field amplitude, and $\psi(x, y)$ the normalized transverse electric field profile. With these considerations and using the external cavity tunable laser model shown in Figure 2.1, the round-trip conditions can be written as

$$r_1 |r_2(\omega)| \sqrt{\alpha_c} \sqrt{\alpha_c} e^{-j\beta_a 2L_a} e^{-j\beta_p 2L_p} e^{-j\phi_{r2}(\omega)} = 1, \quad (2.3)$$

recalling that α_c is the power coupling efficiency between the active and passive sections, $\phi_{r2}(\omega)$ is the argument of the complex reflectance $r_2(\omega)$, and considering β_a and β_p the propagation constants in the active and passive sections, respectively, which can be written as

$$\beta_a = k_0 \mu_a + j \frac{g - \alpha_a}{2} \quad (2.4)$$

$$\beta_p = k_0 \mu_p - j \frac{\alpha_p}{2}, \quad (2.5)$$

being $k_0 = \omega/c$ the wavenumber in vacuum, μ_a and μ_p the effective refractive indices in the active and passive sections, respectively, g the modal gain, which is related to the gain provided by the active section g_{st} and the mode confinement in the active section Γ by the expression $g = \Gamma g_{st}$, and α_a and α_p the power attenuation constants of the active and passive sections, respectively. From the argument of the round-trip expression provided by eq. (2.3), the phase round-trip condition, which defines the longitudinal modes in the cavity, can be extracted. On the other hand, the modulus of eq. (2.3) provides the gain round-trip condition, which ultimately defines which longitudinal modes will lase.

Let us consider firstly the argument of eq. (2.3), which considering the propagation constants given by eqs. (2.4) and (2.5), results in the following phase round-trip condition

$$k_0 \mu_a 2L_a + k_0 \mu_p 2L_p + \phi_{r2}(\omega) = 2\pi m, \quad (2.6)$$

where m is an integer. Considering that $k_0 = \omega/c$, being c the speed of light in vacuum, and doing some basic algebra, the frequency ω can be isolated, resulting in the following expression

$$\omega_m = \frac{2\pi m - c \cdot \phi_{r2}(\omega)}{2(\mu_a L_a + \mu_p L_p)}. \quad (2.7)$$

The integer number m identifies the frequencies of the longitudinal modes that satisfy the phase round-trip condition. The spacing between a certain longitudinal mode with index m , located at a frequency ω_m , and its neighbor modes with indices $m + 1$ and $m - 1$, located at frequencies $\omega_{m\pm 1}$, can be noted as $\delta\omega_{m,m\pm 1}$ and obtained from eq. (2.7) to be

$$\delta\omega_{m,m\pm 1} = |\omega_m - \omega_{m\pm 1}| = \frac{2\pi - c[\phi_{r2}(\omega_m) - \phi_{r2}(\omega_{m\pm 1})]}{2(\mu_{g,a} L_a + \mu_{g,p} L_p)}, \quad (2.8)$$

where $\mu_{g,a}$ and $\mu_{g,p}$ are the group effective refractive indices in the active and passive sections, respectively.

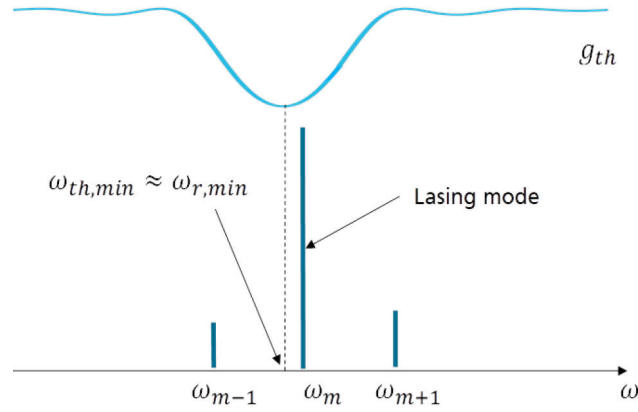


Figure 2.2. Depiction of the longitudinal selection in a laser for single-mode operation.

Considering now the modulus of the round-trip equation in eq. (2.3), as well as the propagation constants given by eqs. (2.4) and (2.5), the following expression for the gain round-trip condition results

$$r_1 |r_2(\omega)| \alpha_c e^{(g_{th} - \alpha_a)L_a} e^{-\alpha_p L_p} = 1, \quad (2.9)$$

where g_{th} is the threshold gain, which corresponds to the gain needed to equalize the cavity roundtrip losses, henceforth noted as α_{tot} . Applying natural logarithms in eq. (2.9) and isolating g_{th} yields to the following expression

$$g_{th} = \alpha_{tot} = \alpha_a + \frac{1}{L_a} \ln \left(\frac{1}{r_1 \alpha_c e^{-\alpha_p L_p} |r_2(\omega)|} \right). \quad (2.10)$$

The second term on the right-hand side of the previous equation corresponds to what can be considered as a distributed mirror loss, which accounts for the losses of the mirrors, the coupling losses between active and passive sections, and the attenuation along the passive section. Therefore, the distributed mirror losses, from now on noted as $\langle \alpha_m \rangle$, can be defined as

$$\langle \alpha_m \rangle = \frac{1}{L_a} \ln \left(\frac{1}{r_1 \alpha_c e^{-\alpha_p L_p} |r_2(\omega)|} \right). \quad (2.11)$$

Notice that the g_{th} provided by eq. (2.10) is frequency dependent due to the frequency dependence of the reflector in the passive section $|r_2(\omega)|$. The wavelength at which the threshold reaches its minimum value can be noted as $\omega_{th,min}$, and fulfills the following relation:

$$g_{th}(\omega_{th,min}) = \min[g_{th}(\omega)]. \quad (2.12)$$

Considering that the losses in the active section α_a will have a certain frequency dependence, but that this frequency dependence will be typically much lower than that of the reflector $r_2(\omega)$, the wavelength at which the threshold reaches its minimum value $\omega_{th,min}$ can be approximated by the value at which the reflector reaches its maximum reflectance, which can be noted as $\omega_{r,max}$ and satisfies

$$|r_2(\omega_{r,max})| = \max|r_2(\omega)|. \quad (2.13)$$

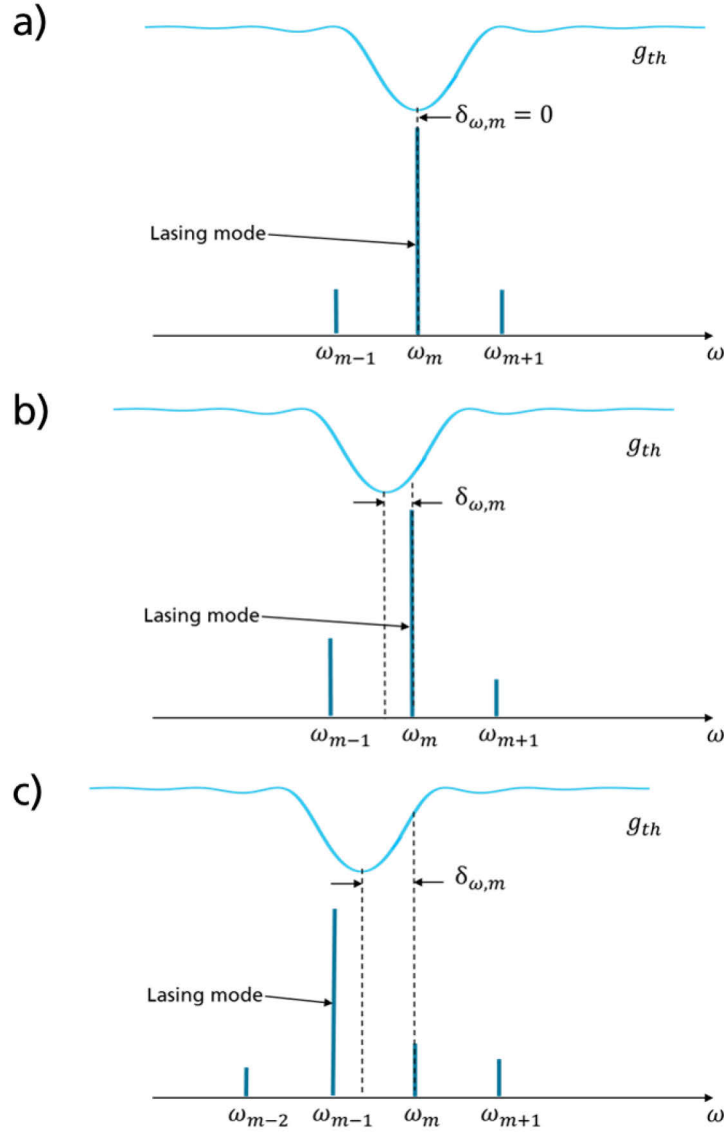


Figure 2.3. Depiction of the threshold gain g_{th} and the longitudinal modes for different detunings between and the frequency-selective reflector and a certain mode with order m , induced by means of tuning reflector: (a) the detuning ($\delta_{\omega,m}$) is zero, (b) detuning non-zero, and (c) the detuning is large enough to produce a mode-hop towards the longitudinal mode with order $m-1$.

Hence, if the reflector $r_2(\omega)$ is adequately designed, only the longitudinal modes ω_m located at the frequency that shows the smallest deviation from the frequency $\omega_{r,max}$ will be able to lase. This is intuitively depicted in Figure 2.2. Tuning in the frequency either the longitudinal modes or $r_2(\omega)$ will allow changing the round-trip phase and gain conditions hence allowing the tuning of the lasing frequency.

2.3 Principles of tuning

Changes in the round-trip conditions provided by eqs. (2.6) and (2.7) will result in a change of the lasing frequency. This can be achieved either by means of changing the central frequency of the reflector in the

passive section, by means of changing the frequency of the longitudinal modes, or by a combination of both methods.

2.3.1 Tuning of the frequency-selective reflector

Let us consider first the effect of tuning the passive reflector with complex reflectance $r_2(\omega)$, parting from an initial condition where the frequency at which the second reflector $r_2(\omega)$ reaches its maximum absolute reflectance, $\omega_{r,max}$, is the same as the frequency of a certain lasing longitudinal mode, ω_m . This is depicted graphically in Figure 2.3 (a). To provide generality to the operation point of the lasing mode with order m , it is useful to define the term detuning as the difference between the frequency of minimum gain threshold and the frequency of the mode. Noting the detuning as $\delta_{\omega,m}$ (do not confuse with the spacing between neighbor longitudinal modes $\delta\omega_{m,m\pm1}$), and approximating the frequency of minimum threshold to the frequency of maximum reflectance $\omega_{r,max}$ (i.e. neglecting the wavelength dependence of the losses in the active section), the detuning can be mathematically defined as

$$\delta_{\omega,m} = \omega_{r,max} - \omega_m. \quad (2.14)$$

If $r_2(\omega)$ is tuned in the frequency by an amount $\Delta\omega_{r,max}$, the newly found expression for the reflectance can be provided by $|r_2(\omega + \Delta\omega_{r,max})| \exp(\phi_{r_2}(\omega + \Delta\omega_{r,max}))$. The central frequency of the passive filter will be now at $\omega_{r,max} + \Delta\omega_{r,max}$. Due to the change in the phase of the passive reflector, the phase-round trip condition given by eq. (2.6) will generally change. This will induce a variation in the frequency of the m -th longitudinal mode, noted as $\Delta\omega_m$, positioning the mode at the frequency $\omega_m + \Delta\omega_m$. In the most general case, $\Delta\omega_m$ will not be equal to the change in the filter frequency $\Delta\omega_{r,max}$. Hence, generally speaking, the detuning defined by eq. (2.14) will be now show a value $\delta_{\omega,m} = (\omega_{r,max} + \Delta\omega_{r,max}) - (\omega_m + \Delta\omega_m)$. This detuning will also induce changes in the gain round trip condition provided by eq. (2.9), since the new mirror losses in the cavity at $\omega_m + \Delta\omega_m$ will increase, causing the threshold gain of the m -th longitudinal mode to vary.

The same procedure can be applied to evaluate the effect of the tuning by $\Delta\omega_{r,max}$ on any longitudinal mode in the cavity. With the change in the central frequency of the reflector, there will be a certain longitudinal mode, which without the loss of generality will be exemplary noted as the mode with order $m - 1$, where its new phase and gain round-trip conditions at its new frequency $\omega_{m-1} + \Delta\omega_{m-1}$ will result in a decrease of the threshold gain g_{th} due to the lower mirror losses. This is graphically depicted in Figure 2.3 (b). With the newly-found lasing conditions for the modes with order m and $m - 1$, the side-mode suppression ratio (SMSR) will be generally varied due to the changes in the threshold gain at the frequencies of the two longitudinal modes.

When the tuning of the passive reflector $\Delta\omega_{r,max}$ induces a detuning $\delta_{\omega,m}$ such that the threshold gain in the secondary-mode is lower than that of the m -th mode, the $m - 1$ -th mode will become dominant, whereas the m -th mode will be suppressed. This effect is known as mode-hop, and is depicted graphically in Figure 2.3 (c).

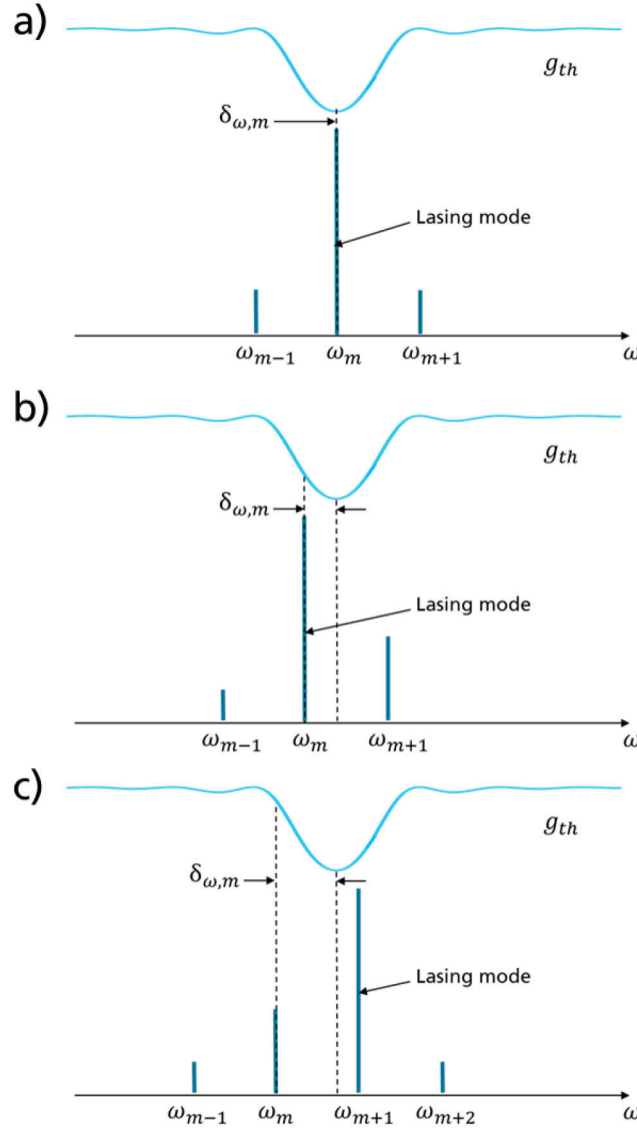


Figure 2.4. Depiction of the threshold gain g_{th} and the longitudinal modes for different detunings between and the frequency-selective reflector and a certain mode with order m , induced by means of tuning the longitudinal modes: (a) the detuning ($\delta_{\omega,m}$) is zero, (b) detuning non-zero, and (c) the detuning is large enough to produce a mode-hop towards the longitudinal mode with order $m + 1$.

2.3.2 Tuning of the longitudinal modes

A second mechanism for achieving tuning is modifying the frequency of the longitudinal modes, which can be achieved by e.g. changing the refractive index or the optical length of the passive section. Let us consider again an initial case with no detuning between the reflector $r_2(\omega)$ and a lasing longitudinal mode ω_m , as shown in Figure 2.4 (a). Changing the effective optical length of the cavity will change the denominator of the phase round-trip condition (2.6), causing a wavelength change of the longitudinal mode. This, added to the effect of the frequency-dependent phase term of the passive reflector $\phi_{r_2}(\omega)$, will cause a change in the nominator of the phase-round trip condition. The combination of both effects will generally contribute

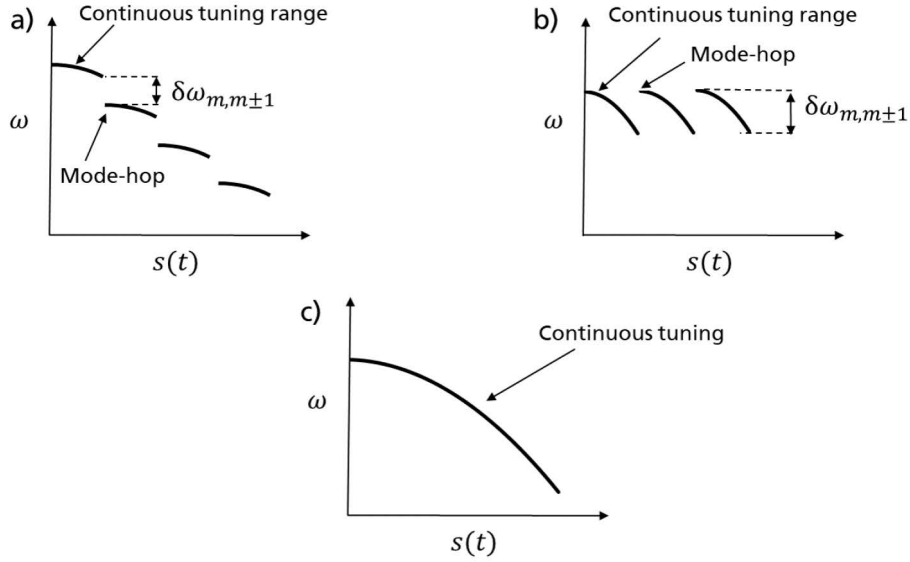


Figure 2.5. Emission frequency versus a certain tuning control signal $s(t)$ for the cases of (a) tuning only the external cavity reflector, (b) tuning the frequency of the longitudinal modes, and (c) tuning achieved by means of adequate tuning of the external cavity reflector and the frequency of the longitudinal modes yielding mode-hop-free (i.e. continuous) tuning.

$\delta\omega_{m,m\pm1}$ denotes the frequency spacing between longitudinal modes

to change the frequency of the lasing mode to reach a certain value $\omega_m + \Delta\omega_m$. If the tunable reflector $r_2(\omega)$ remains untuned (i.e. $\Delta\omega_{r,max} = 0$), a detuning $\delta\omega_{\omega,m} = \Delta\omega_m$ will be induced. This effect is depicted in Figure 2.4 (b). The induced detuning will translate to higher mirror losses for the mode m , since the reflectivity provided by $r_2(\omega)$ will be lower than that compared to the initial condition with detuning $\delta\omega_{\omega,m} = 0$. This will induce g_{th} of the lasing mode m to increase. At the same time, a certain mode will experience now lower mirror losses (in Figure 2.4 (b), this is the case for the mode with order $m + 1$), and hence decrease its threshold gain. Those conditions will cause the SMSR to decrease. When the induced detuning $\delta\omega_{\omega,m}$ is large enough, the newly set round-trip gain conditions allow a neighbor longitudinal mode to lase, thus producing a mode hop, as depicted in Figure 2.4 (c). Notice that the achievable tuning range using this method is typically small due to the narrow bandwidth of $r_2(\omega)$, needed to ensure single-mode operation.

2.3.3 Discontinuous and continuous tuning

From the tuning effects described in the previous subsections, two types of tunings can be distinguished. The first type of tuning is the so-called discontinuous tuning, when mode-hops occur due to the induced detuning. As it was described above, mode-hops typically occur when tuning only the passive reflector. A typical resulting tuning curve is the one shown in in Figure 2.5 (a), where the dependence of the lasing frequency on a certain time dependent control signal $s(t)$ applied to the passive reflector is shown. The frequency jump induced in the tuning will be equal to the spacing between longitudinal modes, noted as $\delta\omega_{m,m\pm1}$, and can be analytically extracted from eq. (2.8). Notice that tuning the passive reflector will provide the possibility of lasing at different longitudinal modes, with the potential of covering a large wavelength range.

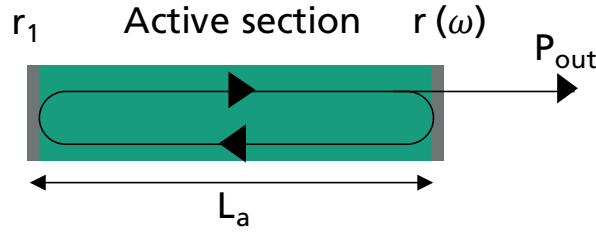


Figure 2.6. Equivalent semiconductor laser model of an external cavity tunable laser. The effective reflectance $r(\omega)$ accounts for the effect of the coupling between active and passive sections, the propagation along the passive section, and the reflectance of the frequency selective reflector.

Discontinuous tuning also occurs when tuning only the position of the longitudinal modes by means of changing the optical length of the cavity, as it has been discussed in the previous subsection. If the reflector in the passive section remains unchanged, the tuning range will be defined limited by the mode spacing in the cavity $\delta\omega_{m,m\pm 1}$ due to the periodicity of the phase round trip condition. The typical tuning behavior of a tunable external cavity laser by means of changing the optical length of the passive section using a certain control signal $s(t)$ is shown in Figure 2.5 (b). Due to the typical small value of $\delta\omega_{m,m\pm 1}$ in external cavity lasers, the achievable tuning range is usually small. The tuning behavior is periodic due to the periodicity of the phase.

The second type of tuning is the mode-hop-free tuning, also known as continuous tuning, where the lasing mode is maintained above the gain threshold and the neighbor modes below threshold for the whole tuning range. In order to ensure this operation mode, the detuning $\delta\omega_m$ needs to be kept constant, or at least with a variation that is small enough to not to induce to a mode-hop. To ensure this along a large frequency or wavelength range, both the reflector and the frequency of the longitudinal modes need to be changed in a very controlled way so that the condition $\Delta\omega_{r,max} \approx \Delta\omega_m$ is satisfied along the tuning. This will result in a tuning curve as shown in Figure 2.5 (c) by means of adequately tuning both the frequency-dependent reflector and the optical length of the resonator using a certain control signal $s(t)$.

2.4 Steady-state characteristics

Characteristics such as the threshold current, output power, and SMSR can be obtained from the well-known rate equations in semiconductor lasers in their time-independent form (i.e. all time derivatives equal to zero) in combination with the laser round-trip conditions developed in Section 2.2. In order to apply the rate equations to an external cavity laser, it is convenient to define an effective semiconductor laser as the one shown in Figure 2.6, on which the effect of the passive section is accounted for by an effective reflectance $r(\omega)$ at the front facet of the active section, and that can be given by the following expression

$$r(\omega) = |r(\omega)|e^{-j\phi_r(\omega)} = \alpha_c e^{-j\beta_p 2L_p} |r_2(\omega)|e^{-j\phi_{r2}(\omega)}. \quad (2.15)$$

2.4.1 Rate equations

The complex time-dependent electric field in the active section of a certain longitudinal mode with order m can be expressed as $E_m(t) \exp(j\omega_m t)$, where ω_m is the angular frequency of the lasing mode given by

eq. (2.7), and $E_m(t)$ is a slow-varying amplitude. Let us start recalling the well-known rate equation of $E_m(t)$ in a semiconductor laser, which can be written as [36]

$$\frac{dE_m(t)}{dt} = \left(j(\omega - \omega_m) + \frac{1}{2}(gv_{g,a} - \tau_p^{-1}) \right) E_m(t), \quad (2.16)$$

where τ_p is the photon lifetime in the cavity, and $v_{g,a}$ is the group velocity in the active section. It will be considered that this slow-varying field amplitude $E_m(t)$ is normalized in such a way that its absolute square corresponds to the photon number of mode m in the laser cavity, noted as $S_m(t)$, a related to the field amplitude by $S_m(t) = |E_m(t)|^2$.

In order to obtain the single-mode rate equation as a function of the photon number S_m , the spontaneous emission of photons needs to be taken into account. This can be done considering the spontaneous emission rate R_{sp} , which is defined as [36]:

$$R_{sp} = n_{sp}v_{g,a}g \quad (2.17)$$

, where n_{sp} is the so-called population inversion factor. Petermann demonstrated in [37] that, for the case of gain guided lasers, the spontaneous emission rate is increased by a factor K_{xy} , known as the transversal spontaneous emission factor, which accounts for the additional spontaneous emission captured by large far fields of gain guided lasers. This factor can be considered to be equal to 1 in index-guided lasers due to the smaller far-fields. Additionally, Henry showed in [38] that, for the case of lasers with strongly asymmetric and low reflectivities, Petermann's spontaneous emission enhancement factor can also be extended to the longitudinal axis in order to account for the non-homogeneous distribution of photons along the cavity length. This effect can be accounted for by a second spontaneous emission enhancement factor K_z , which for a laser cavity with reflectivities $R_1 = r_1^2$ and $R = r^2$, is defined as

$$K_z = \left[\frac{(\sqrt{R_1} + \sqrt{R})(1 - \sqrt{R_1 R})}{2\sqrt{R_1 R} \ln(1/R_1 R)} \right]^2. \quad (2.18)$$

Notice that this parameter is significantly larger than 1 for lasers that show very low reflectivities ($< 10\%$), but close to 1 for typically used reflectivities ($> 10\%$) [38]. With the definition of the spontaneous emission enhancement factors K_{xy} and K_z , the total spontaneous emission rate will then be provided by $K_{xy}K_zR_{sp}$. Therefore, considering the rate equation (2.16) for the electrical field $E_m(t)$, and recalling that $S_m(t) = |E_m(t)|^2$, the rate equation for the photon number S_m can be written as [36]

$$\frac{dS_m}{dt} = S_m(v_{g,a}g - 1/\tau_p) + K_{xy}K_zR_{sp}. \quad (2.19)$$

With regards to the carrier density n , the rate equation is given by the following well known expression

$$\frac{dn}{dt} = \frac{I_a}{qV} - v_{g,a}g(n) \frac{S_m}{V} - R(n), \quad (2.20)$$

where I_a is the injected current in the active section, q is the electron charge, V is the volume of the active section, and $R(n)$ is the recombination rate which accounts for the total spontaneous and the non-radiative recombination.

2. Theory of External Cavity Semiconductor Tunable Lasers

In order to adapt the rate equations (2.19) and (2.20) to the case of external cavity lasers, the photon lifetime τ_p needs to be adequately defined in order to account for the effect of the propagation along the passive section and the wavelength-selective reflector. Recalling that the photon lifetime in a solitary semiconductor laser with group velocity v_g and total losses α_{tot} is defined by $\tau_p = 1/(v_g \alpha_{tot})$, it is needed to find new expression for the group velocity and a total loss which accounts also for the propagation and mirror losses in the passive section.

Let us focus first on finding an expression for the group velocity, which is defined as $v_g = d\omega/dk$, being k the wave number. To account for the external cavity, it is needed to re-define a distributed wavenumber $\langle k \rangle$ in such a way that, when multiplying by twice the length of the active section L_a (what can be intuitively seen as an effective round-trip) it will provide the same phase round-trip condition as provided by eq. (2.6). Therefore, considering eq. (2.6), the distributed wavenumber $\langle k \rangle$ can be defined as

$$\langle k \rangle = \frac{\omega}{c} \mu_a + \frac{\omega}{c} \mu_p \frac{L_p}{L_a} + \frac{\phi_{r_2}(\omega)}{2L_a}, \quad (2.21)$$

where it can be very easily seen that, multiplying this expression by $2L_a$ the same phase shift as the one provided by the phase round-trip condition in eq. (2.6) results. This newly found distributed wavenumber $\langle k \rangle$ allows defining a distributed group velocity $\langle v_g \rangle = d\omega/d\langle k \rangle$. Using the value of $\langle k \rangle$ given by eq. (2.21), the following expression for $\langle v_g \rangle$ results:

$$\langle v_g \rangle^{-1} = \frac{d\langle k \rangle}{d\omega} = \frac{\mu_{g,a}}{c} + \frac{\mu_{g,p}}{c} \frac{L_p}{L_a} + \frac{1}{2L_a} \frac{d\phi_{r_2}(\omega)}{d\omega}. \quad (2.22)$$

This expression for the distributed group velocity allows defining the photon lifetime as $\tau_p = \langle v_g \rangle \alpha_{tot}$, where the total losses in the external cavity laser α_{tot} provided by eq (2.10) have to be considered. The photon lifetime τ_p in the cavity can therefore be expressed as a function of a distributed group velocity $\langle v_g \rangle$ given by eq. (2.22) as

$$\tau_p = \left(\frac{\mu_{g,a}}{c} + \frac{\mu_{g,p}}{c} \frac{L_p}{L_a} + \frac{1}{2L_a} \frac{d\phi_{r_2}(\omega)}{d\omega} \right) \alpha_{tot}^{-1}. \quad (2.23)$$

With this adequate definition of the photon lifetime τ_p , the steady-state characteristics such as threshold current, output power and side-mode suppression ratio can be developed from the rate eqs. (2.19) and (2.20) considering all time derivatives equal to zero.

2.4.2 Threshold current

The relation between the current density in the active section I_a and the stimulated and non-stimulated-emission factors can be obtained from the rate-equation for the carriers provided by eq. (2.20), which by means of doing some basic algebra, can be expressed as:

$$I_a = qV \left[v_{g,a} g(n) \frac{S}{V} + R(n) \right]. \quad (2.24)$$

The threshold current density I_{th} , defined as the injection current needed to reach stimulated emission, can be obtained from the previous equation considering that the stimulated emission equals zero (i.e. $S=0$):

$$I_{th} = qVR(n_{th}) , \quad (2.25)$$

being n_{th} the carrier density achieved at threshold.

2.4.3 Output power

To obtain an expression for the output power above threshold, let us obtain first an expression for the energy stored in the equivalent semiconductor laser cavity shown in Figure 2.6. Provided that S_m is the number of photons in the active section for the mode m , the equivalent energy in the active section, noted as $E_{a,m}$, is provided by

$$E_{a,m} = h\nu S_m , \quad (2.26)$$

where h is the Planck constant, and $\nu = \omega/2\pi$ is the frequency. Multiplying the energy in the active section $E_{a,m}$ by the energy loss rate through the reflectors r_1 and $r(\omega)$, an expression of the total output power can be obtained. For the case of an external cavity laser, the energy loss rate through the reflectors can be obtained by means of multiplying the distributed mirror loss $\langle\alpha_m\rangle$ provided by eq. (2.11) and the distributed group velocity $\langle v_g \rangle$ provided by eq. (2.22). The total output power P_{tot} can be therefore obtained from the energy in the active section provided by eq. (2.26), yielding to the following expression

$$P_{tot} = \langle v_g \rangle \langle \alpha_m \rangle h\nu S_m . \quad (2.27)$$

Notice that, from eq. (2.24) for the injection current I_a , an expression of the photon number S_m as a function of the injection current I_a and the parameters of the active section can be obtained. Plugging this into eq. (2.27), an expression of the output power P_{tot} that will only depend on the injection current I_a , as well as on material and cavity design parameters, can be obtained.

2.4.4 Side-mode suppression ratio

The SMSR is defined as the ratio between the output powers of a certain dominant lasing mode and the second mode with the highest optical intensity. Considering that the dominant mode has a certain order i and the secondary mode an order j , the output powers can be noted as $P_{tot,i}$ and $P_{tot,j}$, respectively. The SMSR is hence given by the following expression:

$$SMSR = \frac{P_{tot,i}}{P_{tot,j}} . \quad (2.28)$$

To obtain an expression for the SMSR, the single-mode rate equations provided by eqs. (2.19) and (2.20) need to be extended to the multimode case, yielding to the so-called multimode rate equations in their steady-state form, which can be written as [36]

$$\frac{dS_m}{dt} = S_m(v_{g,a}g - 1/\tau_{p,m}) + K_{xy}K_zR_{sp,m} \quad (2.29)$$

$$\frac{dn}{dt} = \frac{I_a}{qV} - \sum_m v_{g,a}g \frac{S_m}{V} - R(n) , \quad (2.30)$$

2. Theory of External Cavity Semiconductor Tunable Lasers

being m the order of the longitudinal modes. Since the photon lifetime τ_p given by eq. (2.23) is dependent of the frequency of the longitudinal mode ω_m due to the wavelength dependence of the reflector in the passive section, the subscript m has been introduced.

Considering eq. (2.27) for the output power P_{out} , and given that each longitudinal mode will have a different distributed group velocities $\langle v_g \rangle$ (defined in eq. (2.22)) and mirror losses $\langle \alpha_m \rangle$ (defined in eq. (2.11)) due to the frequency dependence of the reflector in the passive section, the SMSR defined by eq. (2.28) can be expressed as

$$SMSR = \frac{S_i \langle v_{g,i} \rangle \langle \alpha_{m,i} \rangle}{S_j \langle v_{g,j} \rangle \langle \alpha_{m,j} \rangle}, \quad (2.31)$$

where the mode sub-indices i and j have been included in $\langle v_g \rangle$ and $\langle \alpha_m \rangle$ in order to account for their frequency dependence.

Notice that, from eq. (2.24) for the injection current I_a , an expression of the photon number S_m as a function of I_a and the parameters of the active section can be obtained. Plugging this into eq. (2.31), an expression of the SMSR that will only depend on the injection current I_a , as well as on material and cavity design parameters, can be obtained.

2.5 Dynamic characteristics

Having covered the basics of the steady state characteristics of external cavity lasers, studying the dynamic characteristics will allow modelling their modulation and noise behavior. In the following subsections, the relaxation oscillation frequency, damping rate, chirp, relative intensity noise and linewidth of external cavity semiconductor lasers are discussed starting from a different formulation of the rate equations that accounts for the effect of the passive section of the cavity and the frequency-dependent reflector.

2.5.1 Re-visiting the rate equations

In the developments of the steady-state conditions of a tunable semiconductor laser covered in Section 2.4, the standard rate equations of a semiconductor lasers have been used as a starting point, and some adjustments have been performed in order to account for the propagation along the passive section and the frequency dependence of the tunable reflector. In order to develop the dynamic characteristics, a similar approach could be followed using the rate-equations in their time dependent form. Nevertheless, in this work, the formalism followed by Kazarinov and Henry in [39] and by Agrawal and Henry in [40] will be followed for re-writing the new rate equations for an external cavity semiconductor laser. Their formulation is very convenient due to its elegant and intuitive description of the influence of the passive section by means of two simple parameters, A and B , which account for the phase delay induced by the passive section and the frequency dependence of the reflector at the lasing wavelength, respectively.

Kazarinov and Henry started from the rate equations of a reference solitary semiconductor laser comprising the active section of length L_a and real and non-frequency-dependent reflectances r_1 and r at its rear and front-end facets, respectively. A schematic of this reference solitary semiconductor laser is shown in Figure 2.7 (a). To ease the direct comparison between this reference semiconductor laser and the external cavity laser, the reflectivity at r will be defined as

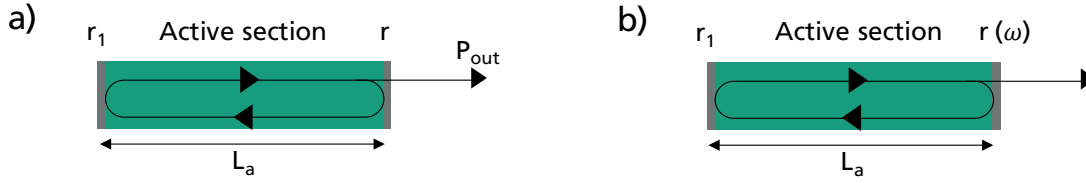


Figure 2.7. Schematics of (a) a reference solitary semiconductor laser comprising the active section in a Fabry-Pérot configuration with reflectors r_1 and r , and (b) equivalent external-cavity semiconductor tunable laser model comprising the active section with real reflectance r_1 at its rear-end, and a complex frequency dependent reflectance $r(\omega)$ at its front-end that accounts for the propagation along the passive section and the frequency-dependent reflector.

$$r = \max(|r(\omega)|), \quad (2.32)$$

, where $r(\omega)$ is given by eq. (2.15) and accounts for the coupling losses between the active and passive section, the propagation along the passive section, and the effect of the frequency-selective reflector. Accounting for the fluctuations due to spontaneous emission in both the optical amplitude and carrier density by means of considering Langevin noise sources [41], respectively symbolized as $F_E(t)$ and $F_n(t)$, the single-mode rate equation for the electrical field $E_m(t)$ of a certain mode with order m and the carrier density n can be re-written as [39]

$$\frac{dE_m(t)}{dt} = \frac{1}{2}(1 + j\alpha)(gv_{g,a} - \tau_{p,s}^{-1})E_m(t) + F_E(t) \quad (2.33)$$

$$\frac{dn}{dt} = \frac{I}{qV} - v_{g,a}g(n)\frac{|E_m(t)|^2}{V} - R(n) + F_n(t), \quad (2.34)$$

where $\tau_{p,s}$ is the photon lifetime of the solitary active section comprising reflectors with real reflectances r_1 and r , which is defined as

$$\tau_{p,s} = [v_{g,a}(\alpha_a + \alpha_m)]^{-1} \quad (2.35)$$

$$\alpha_m = \frac{1}{L_a} \ln\left(\frac{1}{r_1 r}\right), \quad (2.36)$$

, being α_m the mirror losses of the solitary semiconductor laser, and α the Henry linewidth enhancement factor (also known as the chirp factor), which accounts for the coupled phase-intensity fluctuations that occur in the active section [42].

From this point, Kazarinov and Henry considered the external cavity semiconductor laser model used in the previous section and shown again in Figure 2.7 (b). Solving the rate equation (2.33) for the electrical field considering a frequency-selective reflector with reflectance $r(\omega)$ given by eq. (2.15), and expanding in Taylor series $r(\omega)$ around the lasing frequency for the definition of the round-trip boundary conditions, Kazarinov and Henry demonstrated that the new rate equation for the complex electrical field $E_m(t)$ can be obtained easily from eq. (2.33) by means of multiplying the left hand side by a complex factor, yielding the following expression [39]

2. Theory of External Cavity Semiconductor Tunable Lasers

$$\left(1 + A + j\frac{B}{\alpha}\right)\frac{dE_m(t)}{dt} = \frac{1}{2}(1 + j\alpha)\left(gv_{g,a} - \frac{1}{\tau_{p,s}}\right)E_m(t) + F_E(t), \quad (2.37)$$

where $E_m(t)$ is the optical field in the active section, and the parameters A and B are defined as

$$A = \frac{1}{\tau_a} \frac{d\phi_r(\omega)}{d\omega} \quad (2.38)$$

$$B = \frac{\alpha}{\tau_a} \frac{d \ln|r(\omega)|}{d\omega}, \quad (2.39)$$

being $\tau_a = 2\mu_{g,a}L_a/c$ the roundtrip time of the solitary active section. The parameter A accounts for the increase in the photon lifetime due to the propagation along the passive section, and increases monotonically with the optical length of the passive section. The parameter B accounts for the frequency dependence of the reflectance $r(\omega)$. B will show positive values for lasing frequencies which are lower than the frequency of maximum reflectivity of $r(\omega)$ (i.e. the frequency detuning $\delta_{\omega,m}$ given by eq. (2.14) is positive) due to the positive value of the derivative $d \ln|r(\omega)|/d\omega$. The larger is the frequency selectivity of the reflector, the larger will be $d \ln|r(\omega)|/d\omega$, and hence the larger will be B . At the wavelength of maximum reflectance, B will be equal to zero since $d \ln|r(\omega)|/d\omega$ will be zero. At frequencies which are lower than the frequency of maximum reflectivity of $r(\omega)$ (i.e. the frequency detuning $\delta_{\omega,m}$ given by eq. (2.14) is negative), $d \ln|r(\omega)|/d\omega$ will be negative and hence B will be negative too.

On a quick note, notice that, since the definition of $E_m(t)$ used in the solitary active section rate eqs. (2.33-2.34) is kept, the rate equation for carrier density n will be still provided by eq (2.34).

The presented formalism is advantageous since the dynamic characteristics of the lasers can be mathematically described as a function of two simple variables A and B that account for the cavity design of the passive section of the tunable laser. Additionally, it allows for a straightforward comparison between a reference solitary semiconductor laser comprising the active section featuring frequency-independent reflectances r_1 and r (recalling that $r = \max(|r(\omega)|)$), and the same active section in an external cavity configuration with reflectances r_1 and $r(\omega)$.

From this new formalism of the rate equations, the relaxation oscillation frequency, damping rate, chirp, relative intensity noise and linewidth of external cavity semiconductor laser will be developed

2.5.2 Relaxation oscillation and damping rate

In the absence of RC parasitics, the amplitude modulation bandwidth of laser is governed by its relaxation oscillation frequency. Considering the reference solitary semiconductor laser shown in Figure 2.7 (a), the angular relaxation oscillation frequency, from now on denoted as ω_{r0} , can be obtained performing a small-signal treatment of the rate equations (2.33) and (2.34), resulting in the following analytic expression [36]:

$$\omega_{r0} = \sqrt{\frac{P_{tot}(\partial g_{st}/\partial n)v_{g,a}}{h\nu(V/\Gamma)}\left(1 + \frac{\alpha_a}{\alpha_m}\right)}, \quad (2.40)$$

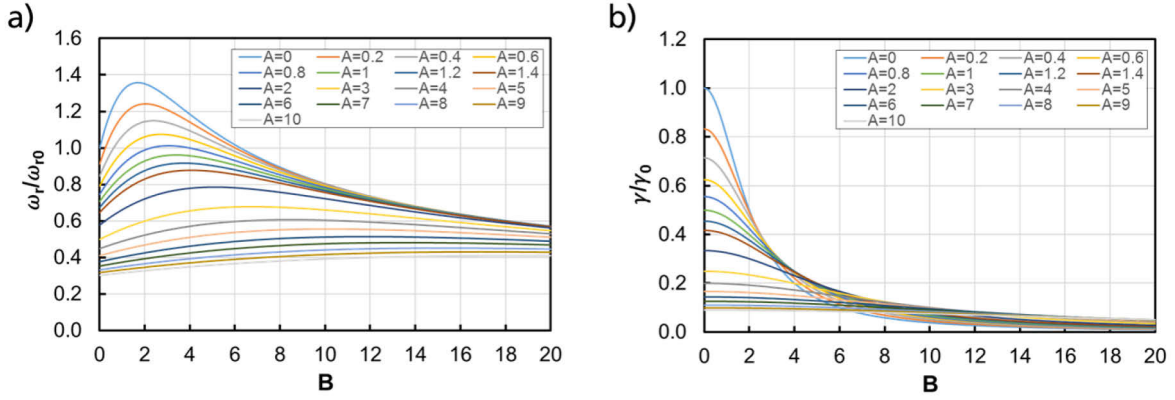


Figure 2.8. (a) Calculated ratio between the relaxation oscillation frequency ω_r in an external cavity configuration for different feedback parameters A and B , and the relaxation oscillation frequency ω_{r0} of the reference solitary laser comprising only the active section with ideal reflectors. (b) Calculated ratio between the damping rates for the same two cases as in (a). In both cases, a Henry linewidth enhancement factor $\alpha = 2.5$ has been considered.

where α_m is provided by eq. (2.36). The formalism used by Kazarinov and Henry was used by Agrawal and Henry in [43] in order to study the influence of the external cavity in the small signal modulation characteristics. They started from the rate equation (2.37) for the optical intensity in an external cavity resonator modelled as in Figure 2.7 (b) with reflectances r_1 and $r(\omega)$, and demonstrated that the relation between the relaxation oscillation frequency in case of an external cavity semiconductor laser, from now on noted as ω_r , and the relaxation oscillation frequency of the reference solitary semiconductor laser ω_{r0} , is given by

$$\frac{\omega_r}{\omega_{r0}} = \sqrt{\frac{1 + A + B}{(1 + A)^2 + \left(\frac{B}{\alpha}\right)^2} \frac{G}{G_0}}, \quad (2.41)$$

where $G_0 = v_{ga}g$ is the gain rate of stimulated emission in the reference solitary semiconductor laser, and G the gain rate of stimulated emission of the external cavity semiconductor laser. Considering the distributed group velocity of the external laser cavity $\langle v_g \rangle$ given by eq. (2.22), the gain rate of the external cavity laser can be expressed as

$$G = \langle v_g \rangle g \quad (2.42)$$

A second parameter that describes the performance in modulation is the damping coefficient, which defines the rate at which the intensity of the relaxation oscillations decay. In the case of the reference solitary semiconductor laser, the analytical expression for the damping coefficient γ_0 can also be obtained from the small-signal development of the rate equations rate equations (2.33) and (2.34) and expressed as [36]

$$\gamma_0 = \frac{K_{xy}K_z n_{sp}}{\langle S_m \rangle} + \kappa_s \langle S_m \rangle, \quad (2.43)$$

being $\langle S_m \rangle$ is the mean photon number under direct modulation, and κ_s gain compression coefficient.

2. Theory of External Cavity Semiconductor Tunable Lasers

Agrawal and Henry also demonstrated in [43] that the damping coefficient in an external cavity configuration, which will be noted as γ , is related to the damping rate γ_0 of the reference solitary semiconductor laser by the following expression

$$\frac{\gamma}{\gamma_0} = \frac{1}{(1 + A)^2 + \left(\frac{B}{\alpha}\right)^2}. \quad (2.44)$$

To evaluate the implications of equations (2.41) and (2.44) for the relaxation oscillation frequency and the damping rate, let us consider for simplicity that $G \approx G_0$, meaning that the external feedback does not modify significantly the photon lifetime in comparison to the case of the solitary active section (i.e., the optical length of the passive section of the cavity is short in comparison to the optical length of the active section). In Figure 2.8 (a), the calculated ratio ω_r/ω_{r_0} from eq. (2.41) is plotted for different external feedback parameters A and B , and considering a linewidth enhancement factor $\alpha=2.5$. As it can be observed, for small values of A (i.e. short external cavities) and values of B close to the linewidth enhancement factor α , an increase in the modulation bandwidth with respect to the case of the reference solitary semiconductor laser can be achieved. This implies that, in order to achieve high relaxation oscillation frequencies in an external cavity tunable laser, it should be targeted that the optical length of the external cavity is as short as possible (i.e. keep A small), and that the tunable laser is set to an operation point such that B is positive and reaching a value close to the linewidth enhancement factor. The setting of the parameter B can be performed by means of detuning the lasing mode from the maximum reflectivity of the reflector in such a way that the lasing frequency of the lasing mode is lower than the central frequency of the external cavity reflector. This operation condition is known as detuned-loading, and affects also the chirp of the laser and linewidth [44, 45], as it will be discussed in the following subsections. This effect can be physically understood as a variation in the effective differential gain (dg_{st}/dn) of the lasing mode due to the coupled phase and amplitude of the lasing field [46]. Nevertheless, it should be mentioned that, in practice, A and B cannot be chosen arbitrarily, since limitations will exist depending on the implementation used for the frequency-selective reflector, and on the design needed to achieve the targeted SMSR values. Therefore, generally speaking, the external cavity laser diodes show a smaller f_r than the solitary active section.

Figure 2.8 (b) shows for different values of the parameters A and B the calculated ratio using eq. (2.44) between the damping rate γ of an external cavity laser and the damping γ_0 of the reference solitary semiconductor laser. As it can be observed, the damping rate in an external cavity laser is always lower than that in the reference solitary laser diode. However, it can also be seen that keeping low values of A (i.e. short passive sections) and low values of B i.e. (detuning as small as possible), the reduction can be minimized.

2.5.3 Relative intensity noise

Under digital amplitude modulation of a semiconductor laser, the intensity noise plays a key role concerning the achievable bit error rate (BER). In semiconductor tunable lasers, one of the most predominant intensity noise sources is the relative intensity noise (RIN). The RIN is primarily induced by the fluctuations in the intensity caused by the spontaneous emission, and increases when increasing the modulation frequency, from now on noted as ω_{mod} , achieving a maximum at the relaxation oscillation frequency ω_r . From the

rate equations rate equations (2.33) and (2.34) for a solitary semiconductor laser, the following expression for RIN at ω_r for a given bandwidth Δf can be extracted from the rate equations [36]:

$$RIN|_{\omega_{mod}=\omega_r} = \frac{4K_{xy}K_z n_{sp} \tau_{p,s}}{\gamma_0^2 \langle S_m \rangle} \Delta f. \quad (2.45)$$

Notice that, for the case of an external cavity semiconductor laser, the photon lifetime will be increased, whereas the damping rate will be reduced (as it was discussed in the previous subsection). Therefore, it is quite intuitive to see from eq. (2.45) that the RIN of an external cavity laser will be always larger than that of the reference solitary semiconductor laser. However, to keep the increase of RIN to a minimum, the same design strategy as the one discussed in Subsection 2.5.2 for keeping the reduction of the damping rate to a minimum can be followed: keeping A (i.e. the length of the passive section) and B (i.e. the detuning) to a minimum.

2.5.4 Chirp

Under digital amplitude modulation of a semiconductor laser, the laser chirp, defined as the frequency modulation induced by a given amplitude modulation, induces a spectral broadening of the laser signal. This effect has a key role in digital transmission links, since due to the chromatic dispersion of glass fibers, a broadening of the signal in the time domain will take place along propagation, which after a certain transmission length, will induce inter-symbol interference and hence increase the BER. This effect implies that the modulation characteristics of a laser are not only defined by the relaxation oscillation frequency and damping rate described in the previous section, but also by its chirp. Being ν the frequency (related to the angular frequency by $\omega = 2\pi\nu$) the chirp $\delta\nu_0$ in the reference solitary semiconductor laser is defined as the frequency excursion that a certain m -th order mode of the laser experiences with respect to its lasing frequency at threshold ν_m (which can be calculated from eq. (2.7)), and is provided by the following expression [27]

$$\delta\nu_0 = \nu - \nu_m = \frac{1}{4\pi} \left[\alpha \frac{d \ln S_m}{dt} + \alpha \left(-v_{g,a} \frac{dg}{dS_m} S_m \right) \right], \quad (2.46)$$

recalling that g is the modal gain, α is Henry's linewidth enhancement factor, and S_m is the photon number of the longitudinal mode m , which varies with time in the case of amplitude modulation. The first term in the square brackets of eq. (2.46) accounts for the variation of the photon number S_m with time, and is hence a term that has a key role under amplitude modulation. For this reason, this term is commonly referred as the transient chirping of the laser, and becomes zero when S_m is constant. The second term in the square brackets corresponds to the chirping induced by the intensity-phase fluctuations that modify the wavelength of the longitudinal modes in the cavity, and is related to the linewidth of the laser in continuous-wave (CW) operation. This contribution is usually referred to as the adiabatic chirping.

To include the effect of the external cavity in the chirping, Choi et. al. used in [27] the notation from Kazarinov and Henry to re-write the chirping equation provided by Petermann in [36] for the case of semiconductor laser with an external cavity reflector, yielding the following expression

2. Theory of External Cavity Semiconductor Tunable Lasers

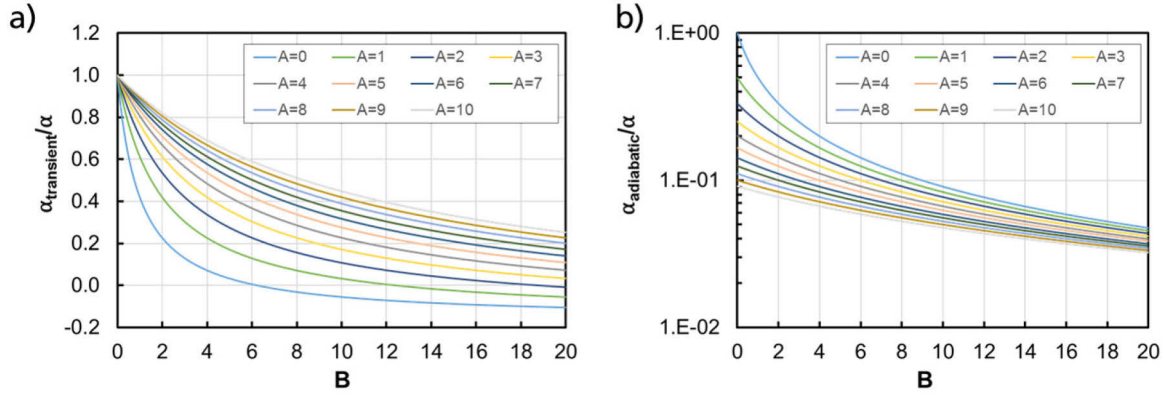


Figure 2.9. Calculated reduction of the (a) transient and (b) adiabatic linewidth enhancement factors of an external cavity laser for different values of A and B . Henry's linewidth enhancement factor α of the active section has been considered to be 2.5.

$$\delta\nu = \frac{1}{4\pi} \left[\alpha \frac{\left(1 + A - \frac{B}{\alpha^2}\right)}{1 + A + B} \frac{d \ln S_m}{dt} + \alpha \frac{1}{1 + A + B} \left(-v_{g,a} \frac{dg}{dS_m} S_m \right) \right]. \quad (2.47)$$

The two terms inside the square brackets comprise Henry's linewidth enhancement factor α multiplied by factors that depend on A and B . This can be understood as two different effective linewidth enhancement factors, which following the same nomenclature as by Choi et. al., can be named transient linewidth enhancement factor, from now on noted as $\alpha_{transient}$, and adiabatic linewidth enhancement factor, from now on noted as $\alpha_{adiabatic}$. Therefore, eq. (2.47) can be re-written as [27]

$$\delta\nu = \frac{1}{4\pi} \left[\alpha_{transient} \frac{d \ln S_m}{dt} + \alpha_{adiabatic} \left(-v_{g,a} \frac{dg}{dS_m} S_m \right) \right] \quad (2.48)$$

where

$$\alpha_{transient} = \alpha \frac{\left(1 + A - \frac{B}{\alpha^2}\right)}{1 + A + B} \quad (2.49)$$

$$\alpha_{adiabatic} = \alpha \frac{1}{1 + A + B}. \quad (2.50)$$

It is worth mentioning that the expression for $\alpha_{adiabatic}$ is the same that Kazarinov and Henry derived in [39].

In order to compare the transient and adiabatic linewidth enhancement factors in an external cavity semiconductor laser with respect to the case of the reference solitary semiconductor laser, the ratios $\alpha_{transient}/\alpha$ and $\alpha_{adiabatic}/\alpha$ are plotted in Figure 2.9 for different external cavity parameters A and B . Henry's linewidth enhancement factor α if the active section has been considered to be 2.5. As it can be seen in Figure 2.9 (a), $\alpha_{transient}$ is strongly reduced if A is small and B is large. This implies that low chirping under direct amplitude modulation will be achieved if the optical length of the passive section is

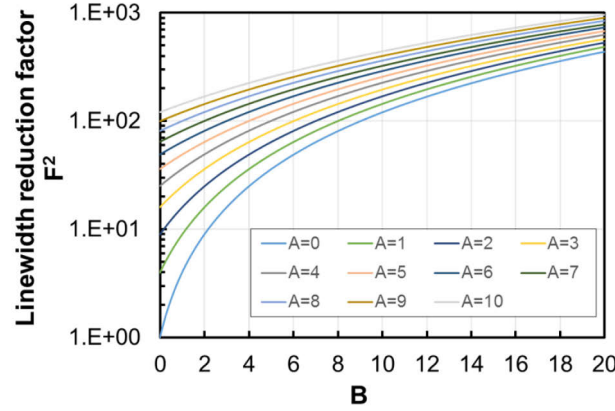


Figure 2.10. Linewidth reduction factor F^2 of an external cavity laser for different A and B parameters of the external cavity reflector. Henry's linewidth enhancement factor α of the active section has been considered to be 2.5.

as short as possible (i.e. small A), and the longitudinal mode is set at a frequency that is lower than the central frequency of the reflector (i.e. large B).

Regarding $\alpha_{adiabatic}$, the smallest values are achieved when both A and B are large, i.e. the optical length of the passive section is long with respect to the passive section, and the longitudinal mode is set at a frequency that is lower than the central frequency of the reflector $r(\omega)$. Notice that this behavior is opposite to the behavior of the $\alpha_{transient}$. However, as it has been mentioned, the adiabatic contribution is the one that dominates when the laser is operated in CW, and the transient contribution is the one that dominates under direct modulation. Hence, to optimizing the chirp performance for direct modulations, the strategies to reduce $\alpha_{transient}$ should be followed.

2.5.5 Linewidth

The linewidth of a laser, and more generally its phase noise characteristics, are key parameters to be taken into account when targeting optical coherent communications, on which information is carried by the amplitude and the phase of the optical signal. In this context, lasers with narrow linewidth and therefore low phase noise are required.

Henry provided for the first time in [42] an expression for the linewidth of a solitary semiconductor laser in CW operation considering the phase-intensity fluctuations in the active section due to spontaneous emission, accounted for by the linewidth enhancement factor α . Introducing the effect of asymmetric reflectances at both ends of the cavity, namely r_1 and r , Henry demonstrated in [38] that the linewidth $\Delta\nu_0$ can be written as:

$$\Delta\nu_0 = \frac{K_{xy}K_zR_{sp}}{4\pi I}(1 + \alpha^2) = \frac{v_{g,a}^2 h\nu K_{xy}K_z n_{sp} \alpha_m (\alpha_a + \alpha_m)(1 + \alpha^2)}{4\pi P_{out} \left(\frac{(r_1 + r)(1 - r_1 r)}{r_1(1 - r^2)} \right)}, \quad (2.51)$$

recalling that K_{xy} and K_z are respectively the transversal and longitudinal spontaneous emission enhancement factors, R_{sp} is the spontaneous emission rate, I the intensity of the optical field in the active section, $v_{g,a}$ the group index in the active section, h the Planck constant, ν the frequency, n_{sp} the spontaneous emission factor, α_m the mirror losses in a solitary semiconductor laser given by eq (2.36), α_a the losses in the active section, and P_{out} the output power that exits the reflector r . The bracketed term in

2. Theory of External Cavity Semiconductor Tunable Lasers

the denominator, which only depends on the reflectances and multiplies the output power P_{out} , accounts for the power emitted on the rear-end reflector. If the rear-end reflector can be approximated to a perfect reflector, this term will be close to 1. For lower reflectivities in the rear-end mirror, this value will be larger than 1. Notice that, from this expression, the linewidth of the reference solitary semiconductor laser (shown in Figure 2.7 (a)) can be calculated, which from now on will be also noted as $\Delta\nu_0$.

Kazarinov and Henry demonstrated in [39] that the linewidth in an external cavity, from now on noted as $\Delta\nu$, is a factor $F^2 = (1 + A + B)^2$ smaller than the linewidth $\Delta\nu_0$ of the reference solitary semiconductor laser. Considering this and the distributed mirror losses $\langle\alpha_m\rangle$ in an external cavity semiconductor laser (given by eq. (2.11)), the linewidth equation (2.51) can be adapted to the following expression:

$$\Delta\nu = \frac{v_{g,a}^2 h\nu K_{xy} K_z(\omega) n_{sp} \langle\alpha_m\rangle (\alpha_a + \langle\alpha_m\rangle) (1 + \alpha^2)}{4\pi P_{out} \left(\frac{(r_1 + |r(\omega)|)(1 - r_1 |r(\omega)|)}{r_1 (1 - |r(\omega)|^2)} \right)} \cdot \frac{1}{F^2}, \quad (2.52)$$

where the frequency dependence has been included in the longitudinal spontaneous emission enhancement factor $K_z(\omega)$ to account for the frequency dependence of the reflector in the passive section. In Figure 2.10, the linewidth reduction factor F^2 is plotted for different values of A and B . As it can be observed, a linewidth reduction of beyond two orders of magnitude is possible to achieve by means of increasing A , i.e. increasing the optical length of the passive section. However, it should be noted that, since the distributed mirror losses $\langle\alpha_m\rangle$ appear in the nominator, and they increase with increasing the length of the passive section, passive waveguides with low losses are desirable to achieve narrow linewidth. Notice also in Figure 2.10 that, increasing B (i.e. increasing the detuning $\delta_{\omega,m}$ defined by eq. (2.14)) allows for a further linewidth reduction.

2.6 Conclusions of the chapter

In this chapter, the general operation principle of a single-mode external cavity tunable laser has been presented. In its more general form, a tunable laser can be modelled as a laser cavity comprising an active element coupled to a passive section implementing a tunable complex reflectance. From this model, the principal lasing characteristics of the tunable lasers can be developed by means of extracting the round-trip conditions both in gain and in phase. With an adequate definition in some of the parameters involved in the rate-equations, the steady state characteristics such as threshold current, output power and SMSR, can be extracted. Additionally, using two parameters which account for the propagation time in the passive section and the effect of the wavelength selective reflectance of the passive reflector, named respectively A and B , the rate-equations can be developed in order to describe key dynamic characteristics such as its direct modulation bandwidth, chirp and linewidth.

It has been seen that, in order to keep values for the relaxation oscillation frequency as high as possible, low values of A (i.e. short passive sections) and values of B (detuning) close to the linewidth enhancement factor are desirable. On the other hand, to avoid a strong reduction of the damping rate, low values of A are also recommended, but low values of B are beneficial. This applies also for the RIN. Finally, with regards to the transient linewidth enhancement factor (related to the chirping induced under direct-modulation), low values of A and large values of B are beneficial. The previous relations between the different characteristics and the parameters A and B allows extracting the following conclusion: when

targeting an external cavity laser with enhanced direct modulation performance, it is always beneficial that the passive section is as short as possible (i.e. low values of A); inducing a certain detuning (i.e. increasing B) can be beneficial for the relaxation oscillation frequency and the transient linewidth enhancement factor (i.e. chirping), but will act negatively on the damping rate. Hence, the detuning can be used as a degree of freedom in order to set the operation point of the tunable laser for either enhancing the relaxation oscillation frequency and reducing chirp, maximizing the damping rate and minimizing the RIN, or for a trade-off between all parameters.

Finally, it has also been seen that, in CW operation, the linewidth of an external cavity laser reduces with a factor $F^2 = (1 + A + B)^2$. Therefore, as a design strategy to achieve narrow linewidths, the use of long passive sections (i.e. large A) and inducing detunings (i.e. large B) is recommendable.

3. Principles of III-V/Polymer Tunable DBR Lasers

After reviewing the general theory of external cavity semiconductor tunable lasers, this chapter introduces the III-V/polymer photonic integration for the implementation of integrated tunable lasers, focusing on the concrete case of a three-section DBR tunable laser operating in the C-band. The structure and modelling of the device, as well as the characteristics and basic performance of the InP-based actives and polymer-based thermo-optically tunable structures, are presented. Finally, aspects regarding the hybrid photonic integration are covered.

3.1 Device structure and operation principle

The schematic of the III-V/polymer three-section DBR tunable laser is shown in Figure 3.1 (a). An InP-based active section bonded on a submount for heat-sinking is end-fire coupled to a polymer waveguide chip, which comprises a thermo-optically tunable Bragg grating implemented by means of sidewall corrugations on the waveguide, and a phase shifter. The active section features an HR coating at its rear-end, and an AR coating in its front facet to avoid undesired back-reflections. Both the active and polymer waveguides are tilted at the coupling interface as an additional mechanism to avoid reflections. The schematic cross section of the active section on submount and the polymer chip are shown in Figure 3.1 (b) and (c), respectively. In the thermo-optically tunable sections of the polymer chip, buried electrodes underneath the waveguide and air trenches are used with the aim to generate a uniformly heated area around the optical mode.

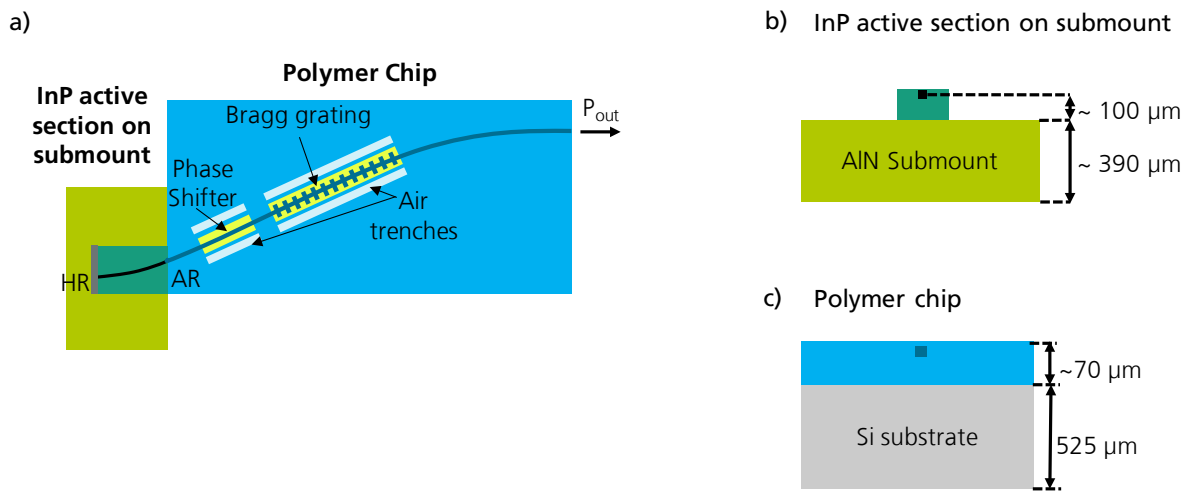


Figure 3.1. a) Top-view schematic of the III-V/polymer tunable DBR laser, consisting of an InP-based active section end-fire coupled to a polymer chip with a thermo-optically tunable phase shifter and Bragg grating. Cross sections at the coupling interface of the (b) InP active section on submount and (c) the polymer waveguide chip.

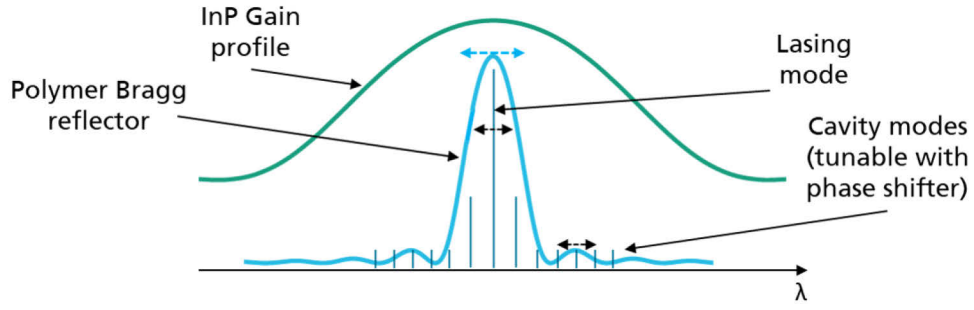


Figure 3.2. Depiction of the lasing and tuning principle in a three-section DBR laser.

The lasing and tuning principle of the proposed structure is shown in Figure 3.2. The Bragg reflector acts as a tunable mode-filter and reflector, enabling the single-mode operation of the laser. By means of tuning the Bragg reflector, different longitudinal modes can be selected to lase, providing a discontinuous coarse wavelength tuning mechanism. On the other hand, the phase shifter can tune the longitudinal modes, which provides a fine-tuning mechanism, and allows adjusting the SMSR.

3.2 External cavity laser model

Following the same procedure as in Chapter 2, the III-V/polymer DBR laser can be modelled as an external cavity semiconductor laser comprising an active section featuring a high reflectance r_1 at its rear end, coupled to a passive polymer-based external cavity section comprising a tunable Bragg reflector featuring a complex reflectance $r_{BG}(\omega)$. A schematic of the DBR laser model is shown in Figure 3.3. The InP active section has a length L_a , and the passive section features a phase shifter with a length L_{PS} , an interconnecting waveguide between the active section and the phase shifter of length L_{WG1} , and an interconnecting waveguide between the phase shifter and the Bragg grating of length L_{WG2} . The purpose of those two interconnecting waveguides is to thermally de-couple the active section, the phase shifter and the Bragg grating. In order to simplify the nomenclature in the following of this work, the total length of the interconnecting waveguides will be noted as L_{WG} , and defined as

$$L_{WG} = L_{WG1} + L_{WG2} \quad (3.1)$$

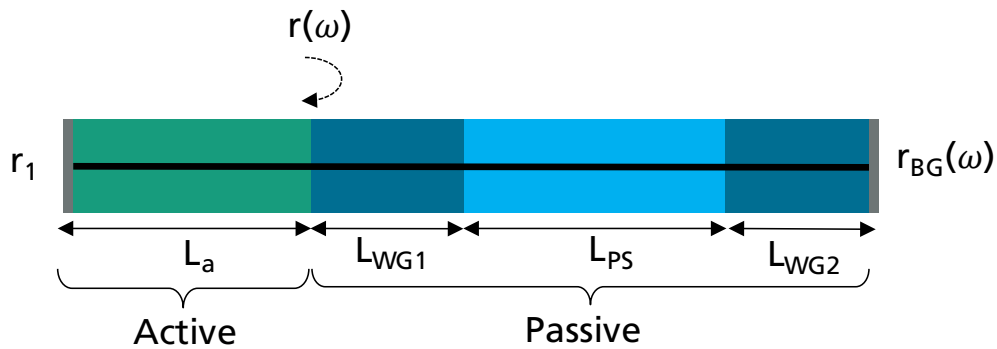


Figure 3.3. Equivalent external-cavity model of a III-V/polymer tunable DBR laser.

Hence, the length of the passive section until the Bragg grating can be defined as

$$L_p = L_{WG} + L_{PS} . \quad (3.2)$$

Notice also that, as it was discussed in Sections 2.4, the effect of the external cavity can be accounted for by an effective reflectance $r(\omega)$ defined by eq. (2.15). For the specific case of the DBR laser, this effective reflectance includes the effects coupling efficiency between the active and passive sections α_c , the propagation along the passive waveguide section with length L_p and power attenuation constant α_p , and the complex reflectance of the Bragg grating $r_{BG}(\omega)$, yielding the following expression

$$r(\omega) = \alpha_c e^{-\alpha_p L_p} r_{BG}(\omega) . \quad (3.3)$$

3.2.1 Basic theory of Bragg gratings

In this subsection, the basic theory of Bragg gratings necessary to describe their effect on the DBR laser model is covered. For a detailed coupled-mode-theory development of the transmission and reflection behavior of sidewall corrugated Bragg gratings, the interested reader is referred to the paper by Yariv and Nakamura [47].

Considering $\tilde{\beta}_{BG}$ the average propagation constant along a Bragg grating with corrugation period Λ , the phase condition for the coupling between the forward and backward waves is provided by [47]:

$$\tilde{\beta}_{BG} = m_{BG} \frac{\pi}{\Lambda} , \quad (3.4)$$

where m_{BG} is an integer, and is defined as the order of the Bragg grating. Considering that the average propagation constant along the Bragg grating can be expressed in its most general form as $\tilde{\beta}_{BG} = \tilde{\mu}_{BG} \omega / c = \tilde{\mu}_{BG} 2\pi / \lambda$, being $\tilde{\mu}_{BG}$ the average effective refractive index in the Bragg grating, the frequency ω_{BG} and wavelength λ_{BG} at which the phase condition provided by eq. (3.4) is fulfilled are given by

$$\omega_{BG} = m_{BG} \frac{c\pi}{\Lambda \tilde{\mu}_{BG}} \quad (3.5)$$

$$\lambda_{BG} = 2\tilde{\mu}_{BG} \frac{\Lambda}{m_{BG}} . \quad (3.6)$$

The reflectance of the Bragg grating can be expressed as [47]

$$r_{BG}(\omega) = |r_{BG}(\omega)| e^{-j\phi_{BG}(\omega)} = \frac{j\kappa \sinh(sL_{BG})}{(\alpha_{BG} + i\Delta\beta) \sinh(sL_{BG}) + s \cosh(sL_{BG})} \quad (3.7)$$

$$s = \sqrt{\kappa^2 + (\alpha_{BG} + i\Delta\beta)^2} , \quad (3.8)$$

where κ is the coupling coefficient of the grating and depends on the depth of the waveguide corrugation, α_{BG} is the power attenuation constant of the grating, and L_{BG} is the physical length of the Bragg grating. $\Delta\beta$ is the frequency deviation from the Bragg condition, and can be defined as $\Delta\beta = \tilde{\mu}_{BG} \omega / c - m_{BG} \pi / \Lambda$. The maximum reflectivity at the Bragg wavelength, defined as $R_{BG} = \max(|r_{BG}(\omega)|^2)$, can be extracted from eq. (3.7). Considering negligible losses in the Bragg grating (i.e. $\alpha_{BG} \approx 0$), the maximum reflectivity is given by the following expression [47]

3. Principles of III-V/Polymer Tunable DBR Lasers

$$R_{BG} = \tanh^2(|\kappa|L_{BG}). \quad (3.9)$$

The reflection bandwidth can be obtained finding the first two zeros of the reflectance provided by eq. (3.7) around ω_{BG} , and can be expressed in terms of frequency ($BW_{\omega,BG}$) and in wavelength ($BW_{\lambda,BG}$) by the following expressions [47]

$$BW_{\omega,BG} = \frac{2\kappa c}{\tilde{\mu}_{g,BG}} \quad (3.10)$$

$$BW_{\lambda,BG} = \frac{\lambda_{BG}^2 \kappa}{\pi \tilde{\mu}_{g,BG}}, \quad (3.11)$$

where $\tilde{\mu}_{g,BG}$ is the effective group index of the Bragg grating.

In order to find an intuitive analytic expression for the some basic characteristics of the DBR laser, it is convenient to treat the Bragg grating as an element with a certain equivalent physical length that induces the phase shift $\phi_{BG}(\omega)$. If the lasing wavelength is nearly equal to the Bragg frequency, the Bragg grating can be considered to be a waveguide section with a certain effective length, namely $L_{BG,eff}$ [48]. This effective length corresponds to the phase delay induced by the Bragg grating in the backwards-coupled wave (i.e. the argument of eq. (3.7)). Considering that the phase delay induced by the Bragg grating is approximated to have linear relation with $\Delta\beta$, the effective length will be frequency dependent and given by [49]

$$2L_{BG,eff}(\omega) = \frac{d \arg\{r_{BG}(\omega)\}}{d\Delta\beta} = \frac{d\phi_{BG}(\omega)}{d\Delta\beta}. \quad (3.12)$$

From eqs. (3.7) and (3.12), and considering $\Delta\beta = 0$ (i.e. the frequency of the propagating wave is equal to the Bragg frequency provided by eq. (3.5)), the following expression for L_{eff} can be obtained [48]

$$L_{BG,eff}|_{\omega_{BG}} = \frac{1}{2} \frac{\alpha_{BG} L_{BG} [\tanh(s_0 L_{BG}) / (s_0 L_{BG}) - 1 / \cosh(s_0 L_{BG})] + \tanh^2(s_0 L_{BG})}{\alpha_{BG} \tanh^2(s_0 L_{BG}) + s_0 \tanh(s_0 L_{BG})} \quad (3.13)$$

$$s_0^2 = \alpha_{BG}^2 + \kappa^2. \quad (3.14)$$

Assuming that the propagation losses along the Bragg grating are negligible (i.e. $\alpha_{BG} \approx 0$), the expression for $L_{BG,eff}$ can be simplified, yielding [50]

$$L_{BG,eff}|_{\omega_{BG}} \approx \frac{1}{2} L_{BG} \frac{\tanh(\kappa L_{BG})}{\kappa L_{BG}}. \quad (3.15)$$

For small values of κL_{BG} , and developing the Taylor series (around 0) of the hyperbolic tangent function, $\tanh(\kappa L_{BG})$ can be approximated by κL_{BG} . Hence, the effective length of the Bragg grating can then be approximated by half of the physical length of the Bragg grating

$$L_{BG,eff}|_{\omega_{BG}} \approx \frac{L_{BG}}{2}. \quad (3.16)$$

3.2.1 Mirror losses, longitudinal modes, and mode spacing

Taking into account the DBR model shown in Figure 3.3 and the theory of Bragg gratings discussed below, some key parameters of the DBR laser cavity such as the mirror losses, the wavelength of the longitudinal modes, and the spacing between longitudinal modes, can be obtained.

Considering the reflectance for the Bragg grating $r_{BG}(\omega)$ given by eq. (3.7), the distributed mirror losses $\langle\alpha_m\rangle$ defined by eq. (2.11) can be re-written for the case of the DBR laser as

$$\langle\alpha_m\rangle = \frac{1}{L_a} \ln \left(\frac{1}{r_1 \alpha_c e^{-\alpha_p L_p} |r_{BG}(\omega)|} \right). \quad (3.17)$$

Notice that, recalling the theory described in Sections 2.4 and 2.5, the distributed mirror losses $\langle\alpha_m\rangle$ play an important role in the equations that describe the steady-state and dynamic characteristics of the external cavity semiconductor lasers.

The DBR model presented in Figure 3.3 allows also describing the longitudinal modes. For the specific case where the detuning between lasing longitudinal mode and the Bragg grating reflector is zero, and considering the effective length of the Bragg grating $L_{BG,eff}$ the wavelength of the longitudinal modes of the cavity can be described in a first approximation as:

$$\lambda_m \approx \frac{2}{m} [\mu_a L_a + \mu_p L_p + \tilde{\mu}_{BG} L_{BG,eff}], \quad (3.18)$$

where m is the order of the longitudinal mode. The mode spacing $\delta\lambda_{m,m\pm 1}$ around a certain wavelength λ between a longitudinal mode λ_m and its neighbor modes λ_{m-1} and λ_{m+1} can be derived from expression (3.18), and written as:

$$\delta\lambda_{m,m\pm 1} \approx \frac{\lambda^2}{2[\mu_{g,a} L_a + \mu_{g,p} L_p + \tilde{\mu}_{g,BG} L_{BG,eff}]}, \quad (3.19)$$

For the case of Bragg gratings with low effective refractive indices and low coupling constants κ (which as it will be shown in the following sections, is the case for the polymer waveguides considered in this work), the effective and group refractive indices of the Bragg grating can be approximated to that of the non-corrugated polymer waveguide, i.e. $\mu_{BG} \approx \mu_p$ and $\mu_{g,BG} \approx \mu_{g,p}$. This allows defining an effective length of the passive section $L_{p,eff}$, which can be expressed as

$$L_{p,eff} = L_{WG} + L_{PS} + L_{BG,eff} \quad (3.20)$$

With this new definition of the effective passive length, equations (3.18) and (3.19) can be re-written as

$$\lambda_m \approx \frac{2}{m} [\mu_a L_a + \mu_p L_{p,eff}] \quad (3.21)$$

$$\delta\lambda_{m,m\pm 1} \approx \frac{\lambda^2}{2[\mu_{g,a} L_a + \mu_{g,p} L_{p,eff}]} \quad (3.22)$$

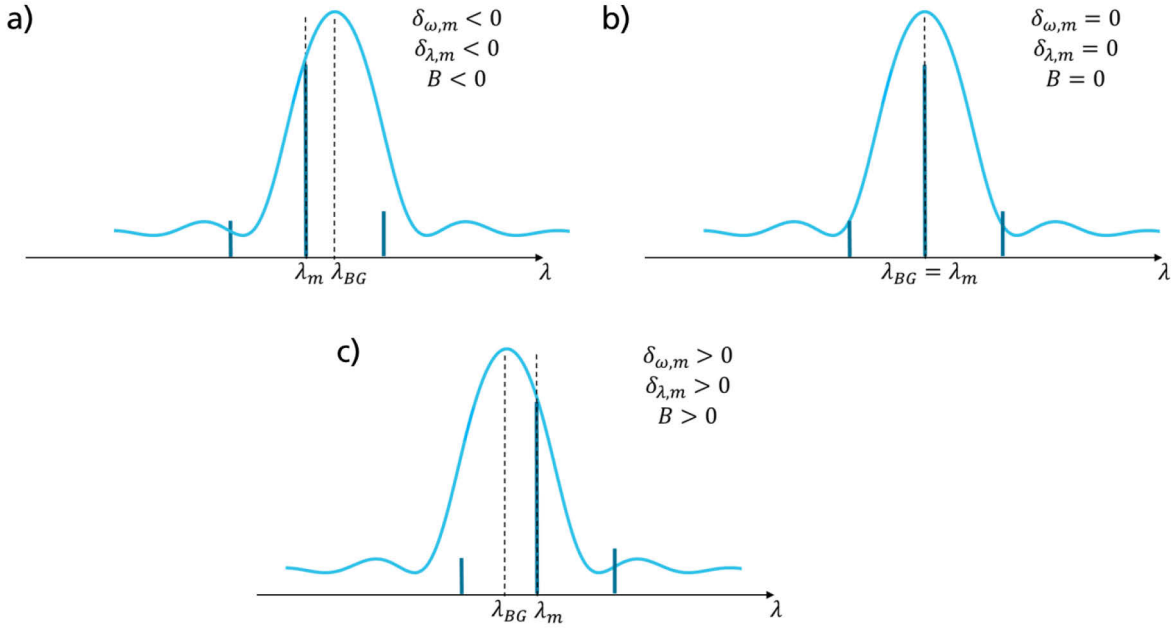


Figure 3.4. Relation between the detuning parameters in frequency ($\delta_{\omega,m}$) and in wavelength ($\delta_{\lambda,m}$), and their relation with the external cavity parameter B . Three different cases are considered: (a) the longitudinal mode is at a shorter wavelength than the Bragg wavelength λ_{BG} (b) the Bragg wavelength and longitudinal mode are at the same wavelength, and (c) the Bragg wavelength is at a longer wavelength than the longitudinal mode.

3.2.2 External cavity parameters A and B

In order to describe the dynamic characteristics of the DBR laser, the parameters A and B introduced in Section 2.5 can be used. From eq. (2.38) for the parameter A , it is straightforward to see that A is the ratio between the optical length of the passive section and the optical length of the active section. The value of A in the proposed DBR laser can be obtained in a first approximation considering the effective length of the passive section $L_{p,eff}$ given by eq. (3.20), which yields to the following expression:

$$A \approx \frac{\mu_{g,p} L_{p,eff}}{\mu_{g,a} L_a}. \quad (3.23)$$

Regarding the parameter B , let us recall that, considering the effective reflectivity seen at the front end of the active section $r(\omega)$ given by eq. (3.3), the parameter B is defined as $B = (\alpha/\tau_a) d \ln|r(\omega)|/d\omega$. Considering the frequency detuning $\delta_{\omega,m} = \omega_{BG} - \omega_m$, if the detuning between Bragg grating and longitudinal mode is such that the longitudinal mode is at a lower frequency (i.e. longer wavelength) than the Bragg grating, $\delta_{\omega,m}$ will be positive, and B will be also positive due to the positive value of the derivative $d \ln|r(\omega)|/d\omega$. On the other hand, if the detuning is such that the longitudinal mode is at a higher frequency (i.e. shorter wavelength) than the Bragg grating, $\delta_{\omega,m}$ will be negative, and B will also be negative due to the negative value of the derivative $d \ln|r(\omega)|/d\omega$. For the case of no detuning, $\delta_{\omega,m}$ will be zero, and B will be also equal to zero since the derivative $d \ln|r(\omega)|/d\omega$ at the Bragg frequency equals zero. To translate this into the wavelength domain, it is convenient to define a wavelength detuning $\delta_{\lambda,m}$ in an equivalent way as the frequency detuning $\delta_{\omega,m}$ of a certain mode with order m provided by eq. (2.14):

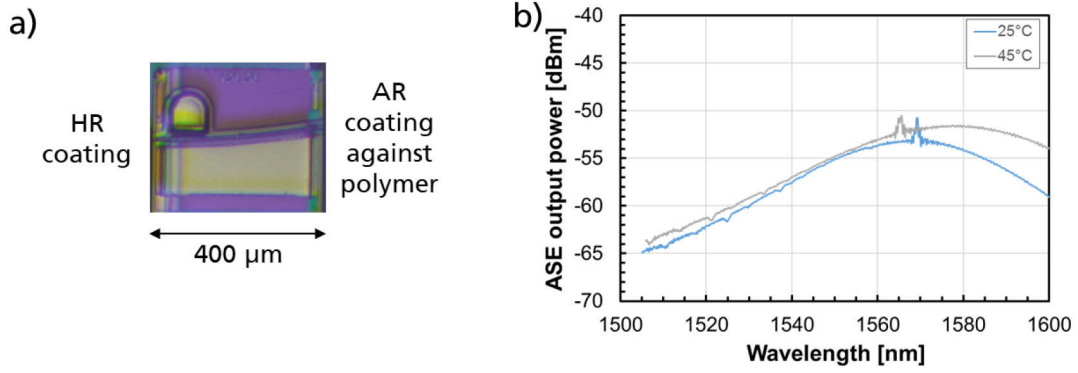


Figure 3.5. (a) Top picture of an InGaAsP multi-quantum-well active section, and (b) amplified spontaneous emission spectra at 25°C and 45°C measured after coupling to a polymer Bragg grating at setting the applied current to the lasing threshold.

$$\delta_{\lambda,m} = \lambda_m - \lambda_{BG} . \quad (3.24)$$

Notice that, for a given detuning condition, this definition of $\delta_{\lambda,m}$ provides always the same sign as $\delta_{\omega,m}$. This is depicted in Figure 3.4 for different detuning conditions, where the sign of the external cavity parameter B are also shown.

Those considerations for the parameters A and B will allow describing the dynamic characteristics of the DBR laser for different detuning conditions covered in Chapter 4.

3.3 InP-based multi-quantum-well active sections

The active sections used in this work were designed by the Lasers Group at Fraunhofer Heinrich Hertz Institute in Berlin, Germany, and fabricated at their InP processing line. The active sections are of TE-emitting buried-heterostructure (BH)-type, and comprise a metalorganic-vapor-phase-epitaxy (MOVPE)-grown InGaAsP multi-quantum well active region. The doping of the InGaAsP can be varied in order to set the photoluminescence wavelength. The BH is optimized to allow for high-speed modulation of the gain reducing the parasitic capacitance by e.g. using narrow active stripes. The rear-end of the active sections is HR coated in order to serve as a mirror in the hybrid laser resonator. The front facet features an AR coating towards polymer and a waveguide tilt angle of 9° in order to avoid back-reflections at the coupling interface. Furthermore, the waveguide front-facet is laterally tapered in order to optimize the mode-overlap towards the polymer-based waveguides.

In Figure 3.5 (a), the top picture of an active section is shown. In Figure 3.5 (b), the measured amplified spontaneous emission spectra (ASE) at 25°C and 45°C are plotted. The measurement was performed on a active section coupled to a polymer Bragg grating, and the injection current in the active section was set in order to operate at threshold. The peaks in the curve at around 1570 nm for the measurement at 25°C and 1568 nm for the measurement at 45°C correspond to the Bragg wavelength of the polymer-grating, which varies with the temperature due to the thermo-optical effect. As it can be observed, the photoluminescence (PL) wavelength at 25°C is around 1570 nm, while at 45°C the PL wavelength shifts towards 1580 nm. The full-width-half-maximum (FWHM) bandwidth exceeds 40 nm at both operation temperatures, showing

3. Principles of III-V/Polymer Tunable DBR Lasers

TABLE 3.1. PARAMETERS OF THE POLYMER WAVEGUIDES AT 1550 NM

PARAMETER	SYMBOL	VALUE
REFRACTIVE INDEX OF POLYMER CLADDING	μ_{cladd}	1.45
REFRACTIVE INDEX OF POLYMER CORE	μ_{core}	1.47
WAVEGUIDE CORE DIMENSIONS	$w_{core} \times h_{core}$	$3.5 \times 3.5 \mu\text{m}^2$
EFFECTIVE REFRACTIVE INDEX OF THE POLYMER WAVEGUIDE	μ_p	1.456
EFFECTIVE GROUP INDEX OF THE POLYMER WAVEGUIDE	$\mu_{g,p}$	1.456
PROPAGATION LOSSES OF THE POLYMER WAVEGUIDE	α_p	0.7 dB/cm
THERMO-OPTICAL COEFFICIENT OF THE POLYMER MATERIAL	TOC	$-1.1 \times 10^{-4}/\text{K}$
COEFFICIENT OF THERMAL EXPANSION	CTE	$2-3 \times 10^{-4}/\text{K}$

their suitability for tunable lasers in the C-band. Notice that the ASE in the case of the measurement at 45°C shows slightly larger power values than at 25°C. This is due to the fact that the injection current applied at 45°C was higher than the threshold current applied in the case of 25°C in order to achieve the threshold condition.

For the theoretical calculations performed in the remaining of this work, the parameters for the InGaAsP active sections summarized in Appendix E will be considered.

3.4 Polymer-based thermo-optically tunable sections

The single-mode polymer waveguide considered in this work is of buried-channel type and features a square core with width w_{core} and height h_{core} of $3.5 \mu\text{m}$ and a refractive index $\mu_{core} = 1.47$, and top and bottom

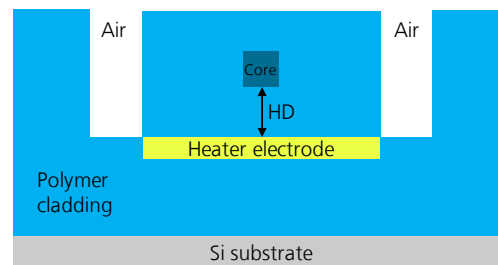


Figure 3.6. Cross-section view of the tunable polymer waveguide with buried micro-heater electrode and air trenches. HD is the distance between the micro-heater and the waveguide core.

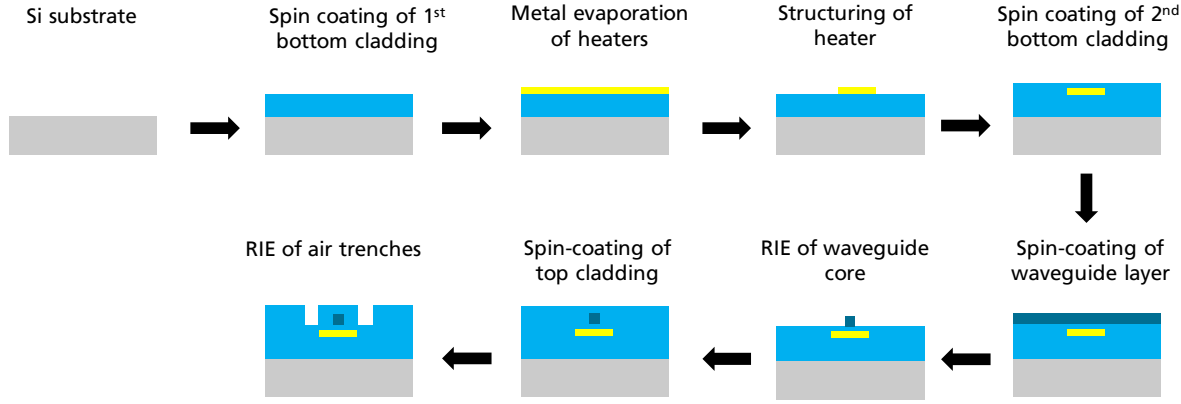


Figure 3.7. Fabrication process of the polymer waveguides including micro-heaters.

claddings with refractive index $\mu_{cladd} = 1.45$. The polymer material used is the ZPU-12 series from the company ChemOptics Inc. [29]. Table 3.1 summarizes the already mentioned geometrical and optical characteristics of the polymer waveguides, together with other key parameters such as the effective refractive index of the polymer waveguide μ_p , effective group index of the polymer waveguide $\mu_{g,p}$, the propagation losses α_p , the thermo-optical coefficient (TOC), and the coefficient of thermal expansion (CTE). Since the polymer material used shows a low dispersion in the C-band, it will be considered that the group index equals the effective refractive index, i.e. $\mu_{g,p} \approx \mu_p = 1.456$.

A schematic of the waveguide cross-section at the thermo-optically tunable phase sections and Bragg gratings is shown in Figure 3.6. The metal micro-heater is buried beneath the core with the aim of providing a uniform temperature distribution along the waveguide cross section, as well as protecting the metal electro-heater from damages and discharges from the environment. The vertical distance between the heater and waveguide core, indicated as HD in Figure 3.6, can be minimized in order to achieve the highest heating efficiency possible without introducing significant optical losses to the propagating mode. Simulation and experimental results showed that an HD of $3 \mu\text{m}$ did not increase the losses of the TE propagating wave, and this value was set for the fabrication of the polymer waveguides considered in this work. To isolate the heat generated by the heater electrode, air trenches on the sides of the waveguide direction are formed.

The study on the tuning efficiency of the polymer-based thermo-optically tunable Bragg gratings was reported in a publication related to this work [51], in which I contributed by designing and characterizing the Bragg gratings. The considered waveguide cross section was the same as shown in Figure 3.6, and the goal was to find adequate cross section geometries to ensure efficient thermo-optical tuning. More concretely, the effect of the air trench depth and bottom cladding thickness to provide a heat confinement and thermal buffer, was studied. Thermal simulations were carried out using the finite element method (FEM) method. Those simulations showed that increasing the thickness of the buffer cladding and of the air trenches the heat confinement along the optical mode, and hence an increase of the thermo-optical tuning efficiency, can be achieved. This can be understood by the fact that air and polymer have low thermal conductivities, and hence act as thermal buffers. These considerations have been taken into account in the fabricated devices presented throughout this work.

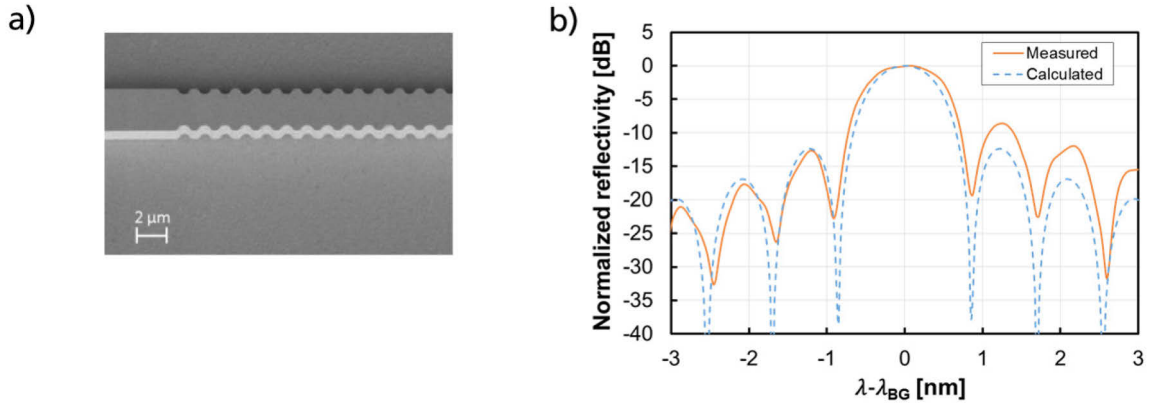


Figure 3.8. (a) Picture of a polymer-based Bragg grating waveguide, and (b) comparison of measured and calculated spectra for a polymer Bragg grating with a length of $L_{BG} = 1$ mm and a reflectivity $R_{BG} = 25\%$.

3.4.1 Fabrication

The fabrication process of the polymer waveguides is depicted in Figure 3.7. The ZPU-12 cladding material is spin-coated on a 4" Si substrate with a thickness of 525 μm, cured by UV illumination and baked at a temperature of 200 °C. Following, metal is evaporated on top of the bottom cladding in order to form the micro-heater stack, which is subsequently structured. A second layer of bottom cladding is spin coated and cured, serving as a buffer between the micro-heater and the core of the waveguide. Following, the core layer is coated, cured and etched using reactive ion etching with oxygen plasma to form the waveguide. Notice that the sidewall corrugations are also lithographically defined at the same step, hence no additional processes are necessary for the fabrication of grating structures. Finally, air trenches are etched on both sides of the thermo-optically tunable waveguide sections for enhanced heat confinement. It should be noted that the number of lithographic steps amounts to 3 (one for the heater electrode structuring, a second one for the waveguide, and a final one for the etching of the air trenches).

3.4.2 Tunable Bragg gratings

As previously mentioned, the Bragg gratings are implemented on the polymer waveguide by means of sidewall corrugations, as shown in Figure 3.8 (a). The Bragg wavelength is defined by the corrugation period Λ and the average effective refractive index in the grating $\tilde{\mu}_{BG}$ by means of eq. (3.6). In order to relax the fabrication accuracy required, Bragg gratings with order $m_{BG} = 3$ have been considered in this work. Due to the low refractive index of the polymer materials used in this work (see Table 3.1) it is valid to consider in a first approximation the effective and group index of the polymer Bragg gratings the same effective and group indices of the polymer waveguides showed in Table 3.1, i.e. $\tilde{\mu}_{BG} \approx \mu_p = 1.456$ and $\tilde{\mu}_{g,BG} \approx \mu_{g,p} = 1.456$. From equations (3.6)-(3.11), the design parameters of the polymer Bragg grating Λ , κ , and L_{BG} can be set in order to achieve the targeted Bragg wavelength, maximum reflectance, and bandwidth.

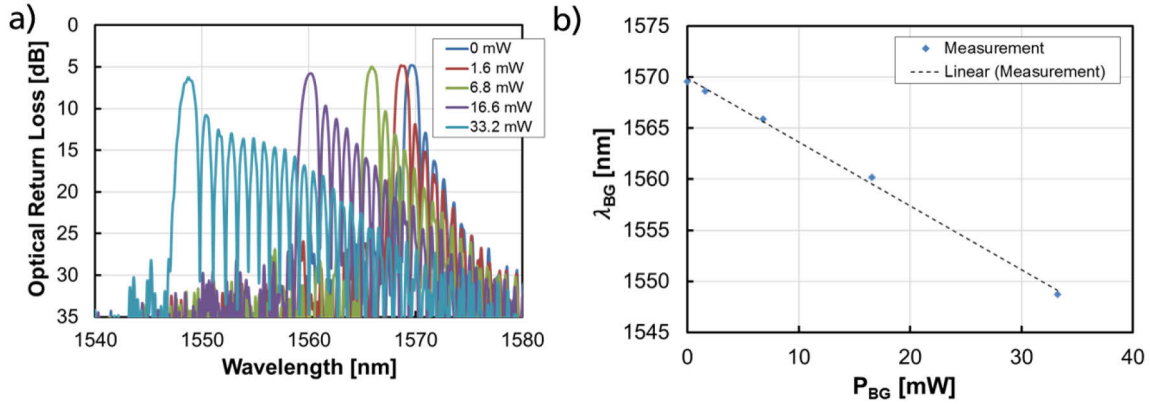


Figure 3.9. (a) Measured spectra of a 1mm long Bragg grating with a reflectivity of 25% for different electrical powers applied on the heater electrode. (b) Measured central Bragg wavelength (λ_{BG}) at different electrical powers on the micro-heater (P_{BG}).

Figure 3.8 (b) shows the measured normalized reflectivity of a third order polymer Bragg grating with a length of $L_{BG} = 1$ mm and a reflectivity of $R_{BG} = 25\%$ designed for wavelength of $\lambda_{BG} = 1570$ nm which, considering $\tilde{\mu}_{BG} = 1.456$, corresponds to a grating period of $\Lambda = 1.617$ μm . As a comparison, the calculated reflectivity spectrum using eq. (3.7) is shown. As it can be seen, the measured spectrum shows a slight asymmetry, which can be attributed to an apodization in the Bragg grating, which might be caused by a stress in the Bragg grating induced after the etching of the air trenches. Nevertheless, the reflection bandwidth $\Delta\lambda_{BG}$ fits fairly well with the calculated results.

By means of applying current on the Bragg grating micro-heater, and hence increasing the temperature on the Bragg grating waveguide by a certain value T'_{BG} , eq. (3.6) for the Bragg wavelength λ_{BG} can be modified in the following way to account for the influence of thermal effects:

$$\lambda_{BG} = \frac{2}{m_{BG}} (\tilde{\mu}_{BG} + TOC \cdot T'_{BG}) (\Lambda + \Lambda \cdot CTE \cdot T'_{BG}), \quad (3.25)$$

where TOC the thermo-optical coefficient of the ZPU-12 polymer material, and CTE its coefficient of thermal expansion (values for both are provided in Table 3.1). Due to the low thermal conductivity of polymers and the use of air trenches, the heat dissipated by the micro-heaters will be confined in a relatively small volume, and the rest of the polymer material will remain unheated. The larger volume of non-heated polymer material will not allow the heated polymer area to largely expand. Hence, in this work, it will be considered in a first approximation that the effect of the thermal expansion can be disregarded. Therefore, the expression that provides the Bragg wavelength as a function of the temperature will be provided by the following expression

$$\lambda_{BG} = \frac{2}{m_{BG}} (\tilde{\mu}_{BG} + TOC \cdot T'_{BG}) \cdot \Lambda. \quad (3.26)$$

Notice from this expression that, due to the negative TOC of the polymer material, an increase in the temperature will shift λ_{BG} towards shorter wavelengths. Considering eq. (3.26), which provided the dependence of the Bragg wavelength λ_{BG} and a certain temperature change T'_{BG} , derivation with respect to T'_{BG} provides wavelength variation with temperature:

3. Principles of III-V/Polymer Tunable DBR Lasers

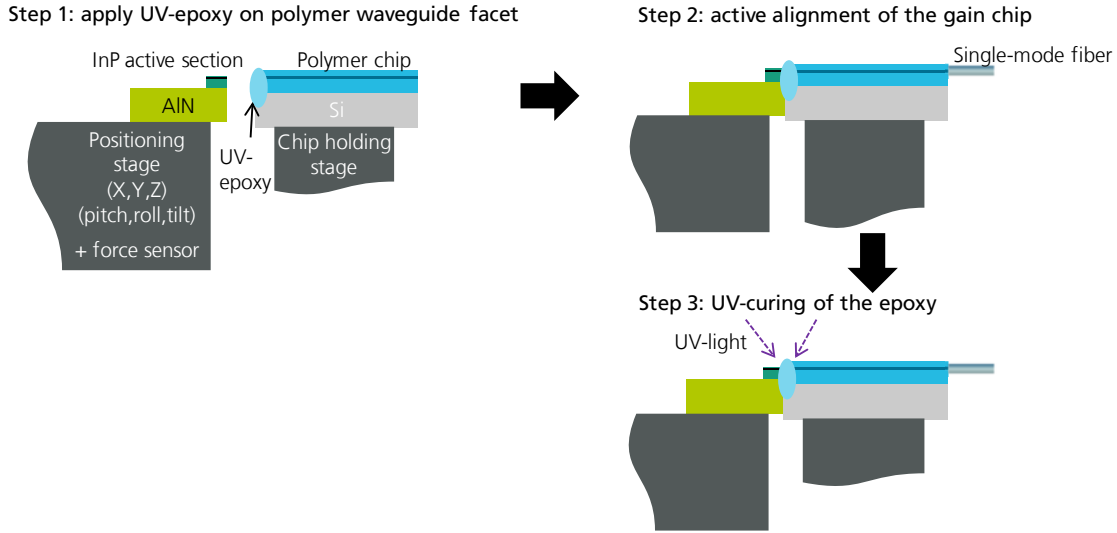


Figure 3.10. Active alignment process for III-V/polymer hybrid integration.

$$\frac{d\lambda_{BG}}{dT'_{BG}} = \frac{2}{m_{BG}} TOC \cdot \Lambda. \quad (3.27)$$

Figure 3.9 (a) shows the optical return loss of the same grating shown in Figure 3.8 (b) measured at different electrical powers applied on the Bragg grating micro-heater, from now on noted as P_{BG} . For a heater power of 33.2 mW, a tuning of the Bragg wavelength of around 21 nm is achieved. From eq. (3.27), and considering the thermo-optical coefficient from Table 3.1 and a grating period $\Lambda = 1.617 \mu\text{m}$, it is straightforward to calculate that this wavelength tuning corresponds to a temperature increase in the polymer waveguide of around 177°C. At room temperature (25°C), this implies that the local temperature in the polymer Bragg grating exceeds 202°C, which is slightly larger than the baking temperature of 200°C used in the fabrication process of the polymer waveguides (see the previous subsection). Therefore, sustained 21 nm tuning of the Bragg grating is expected to have negative consequences in the long-term reliability of the device.

In Figure 3.9 (a), it can also be observed that the symmetry of the reflection spectra decreases with increasing the electrical power on the micro-heater. This effect can be attributed to a non-uniform temperature distribution along the Bragg grating, or some residual thermal expansion induced in certain areas of the Bragg grating. Figure 3.9 (b) shows the correspondence between heater power and measured Bragg wavelength. From the minimum-square fit of the measurement points, a tuning efficiency of 0.62 nm/mW is achieved.

3.4.3 Phase shifters

Phase shifters are used to change the optical length of the resonator in order to tune the wavelength of the longitudinal modes. Being m the order of a certain longitudinal mode and T'_{PS} the variation in the temperature induced in the phase shift section, the wavelength of a longitudinal mode with order m_l as a function of a phase section with length L_{PS} can be obtained from eq. (3.18) to be

$$\lambda_m = \frac{2}{m} [\mu_a L_a + \mu_p L_{WG} + (\mu_p + TOC \cdot T'_{PS}) L_{PS} + (\tilde{\mu}_{BG} + TOC \cdot T'_{BG}) L_{BG,eff}] . \quad (3.28)$$

, where the effect of increasing the temperature in the Bragg grating T'_{BG} has also been included. Notice that the variation in the wavelength of the longitudinal mode with temperature in the phase section can be obtained partially differentiating eq. (3.28) with respect to T'_{PS} :

$$\frac{\partial \lambda_m}{\partial T'_{PS}} = \frac{2}{m} TOC \cdot L_{PS} . \quad (3.29)$$

3.5 III-V/polymer hybrid integration

In this section, the hybrid integration process between the InP-based active section and the polymer-based passive section is described, and the coupling losses calculated.

3.5.1 Description of the automatic alignment process

For the hybrid integration of the active section and the polymer waveguide, an active alignment method for butt-joint coupling was used. In Figure 3.10, the alignment sequence is described. In a first step, the active section, already bonded on the submount, is placed on a contact holder, which is fixed to a 6 axis alignment stage, and is electrically contacted to apply the injection current. The alignment stage allows controlling the horizontal, vertical and longitudinal axis, as well as the pitch, roll and tilt angles. Additionally, the contact holder includes a force-sensor, which allows detecting contact between the InP active section and polymer chip. The polymer chip is placed on a separate holding stage, where the vertical axis can be controlled in order to roughly adjust the device in the same horizontal plane as the active section. A drop of UV-curable optical glue, with a refractive index of 1.45, is placed on the facet of the polymer waveguide where the active section will be coupled. Since the active section features on its front facet an AR coating towards polymer, this glue avoids any air gaps and hence provides a good optical matching between the active and passive sections, as well as a fixation mechanism. In a second step, the active section is approached towards the polymer chip, where the glue serves as a wet interface. Additionally, a single-mode fiber placed on a 3-axis stage is approached to the output waveguide of the polymer chip, which allows detecting the output power. After the search of first-light, i.e. a rough optical alignment between active section, polymer chip and output fiber, the automatic alignment process for fine adjustment starts, which controls the 6-axis of the gain-chip stage and the 3-axis of the output fiber, and monitors the measured output power and the contact force between the active section and polymer chip. Once force has been detected and the output power optimized, the alignment process is finished. In the final step, the optical glue is cured with UV, fixing the gain chip to the polymer chip, and hence finalizing the hybrid integration process. Optionally, an additional UV-curable glue can be applied on the interface between active section and polymer in order to increase the robustness of the coupling, and the hybrid device can be cured with temperature in order to finalize the cross-linking process of the glues.

3.5.2 Coupling losses and alignment tolerances

For the implementation of III-V/polymer tunable lasers, the coupling interface between InP and polymer waveguide is of crucial importance. Low coupling efficiency at this coupling point will affect the round-trip gain conditions, and hence degrade the performance of the laser not only with regard to the achievable

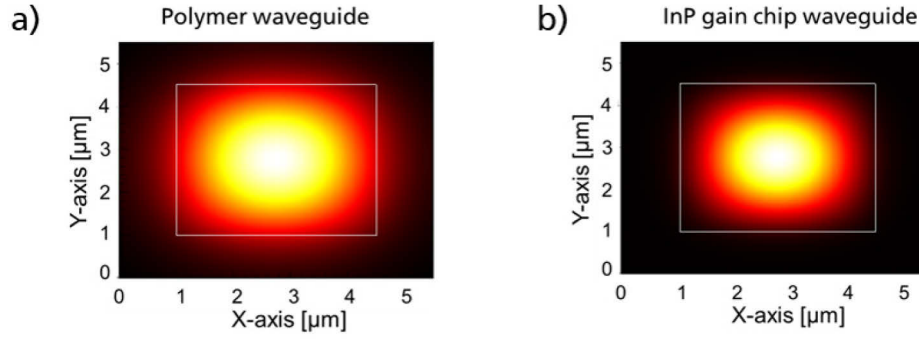


Figure 3.11. Simulated intensity distribution of the fundamental TE mode at 1550 nm of (a) InP multi-quantum-well active section and (b) polymer waveguide with a square cross section of $3.5 \times 3.5 \mu\text{m}^2$. The $1/e^2$ mode-field diameters can be extracted to be $4.7 \mu\text{m}$ for the horizontal and vertical axis in the case of the polymer waveguide, and $3.37 \mu\text{m}$ in the horizontal axis and $3.29 \mu\text{m}$ in the vertical axis for the case of the InP active section.

optical output power, but also with regard to other parameters such as linewidth, modulation bandwidth, and chirp. Hence, a high overlap of the field distributions of the InP and polymer waveguides is necessary. The overlap η is defined by the mode overlap integral between two normalized electric field distributions $\psi_a(x, y)$ and $\psi_p(x, y)$, which can be written as

$$\eta = \frac{|\iint \psi_a \psi_p dA|^2}{\iint |\psi_a|^2 dA \iint |\psi_p|^2 dA}. \quad (3.30)$$

The simulated intensity distribution of the fundamental TE-mode at 1550 nm in the polymer waveguide Figure 3.11 (a). The $1/e^2$ mode field diameter is $4.7 \mu\text{m}$ in the horizontal and vertical directions. To achieve a high mode overlap between the InP active section and the polymer waveguide, the waveguide of the active section features a lateral taper at the front facet. The simulated intensity distribution at the front facet of the active section is shown in Figure 3.11(b), where the $1/e^2$ mode field diameter can be extracted to be $3.37 \mu\text{m}$ in the horizontal direction and $3.29 \mu\text{m}$ in the vertical direction, resulting in an almost circular field distribution. The simulated coupling losses for different vertical or horizontal misalignment offsets between the InP and polymer waveguides are shown in Figure 3.12. The coupling losses in the case of perfect

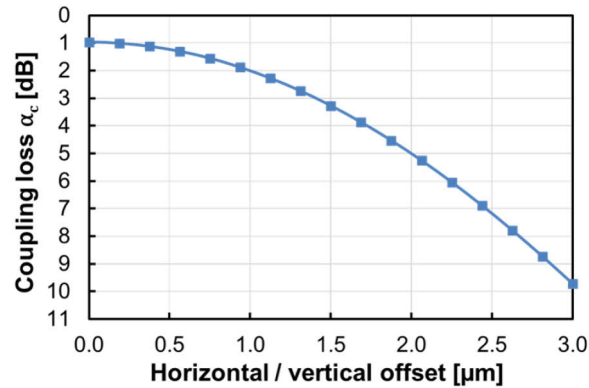


Figure 3.12 Simulated coupling losses between InP active section and polymer waveguide for different vertical or horizontal offsets at the coupling interface.

alignment amount to 1 dB. Regarding the effect of the offset in the coupling, it can be seen that the alignment tolerances for a 1-dB variation of the coupling losses fall within $\pm 1\mu\text{m}$. Notice that a sub-micrometer accuracy can be provided by commercially available photonic assembly systems [52], as well as by passive bonding equipment [53].

3.6 Conclusions of the chapter

In this chapter, a tunable DBR laser based on the III-V/polymer hybrid photonic integration has been presented. A model of this device was developed using the general theory of external cavity lasers covered in Chapter 2. The hybrid integration concept combines InGaAs MQW active sections providing optical gain in a wavelength range larger than 40 nm, and thermo-optically tunable Bragg gratings with a tunability of more than 20 nm. For the hybrid integration of the tunable laser, the active and the polymer passive elements are end-fire coupled using an active alignment method. Waveguide tapering at the front facet of the active section allows achieving theoretical coupling losses of 1-dB and alignment tolerances of $\pm 1\mu\text{m}$.

4. Design Strategies and Performance of III-V/Polymer Tunable DBR Lasers

After having introduced in the previous chapter the model of the III-V/polymer DBR lasers and the characteristics of the InP MQW active sections and thermo-optically tunable polymer waveguides, this chapter focuses on the design strategies and performance when targeting high-speed direct-modulation, narrow linewidth, and continuous tuning.

4.1 High-speed direct modulation

As it has been discussed in Subsections 2.5.2-2.5.4, the behavior of an external cavity laser under direct modulation is defined by its relaxation oscillation frequency f_r , damping rate γ , RIN and chirp. It has also been seen that keeping short passive sections (i.e. low parameters of A) is beneficial to achieve a large relaxation oscillation frequency, a large damping rate, a low RIN, and a low chirp (accounted for by the transient linewidth enhancement factor $\alpha_{transient}$). Additionally, inducing a certain detuning, which can be modelled by the parameter B given by eq. (2.39), the chirping (i.e. $\alpha_{transient}$) can be reduced. For a given value of A (i.e. for a given external cavity laser geometry) the increase of the parameter B can increase the relaxation oscillation frequency

With the aim to fulfil the strategy of keeping the length of the passive section as short as possible, the device considered to study the high-speed modulation performance comprised a passive section with a 3rd order Bragg grating with length $L_{BG}=700\text{ }\mu\text{m}$ a phase section with length $L_{PS}=200\text{ }\mu\text{m}$, and an interconnecting waveguide sections with total length $L_{WG}=300\text{ }\mu\text{m}$. The design wavelength of the Bragg grating was 1570 nm (corresponding to a period $\Lambda=1.617\text{ }\mu\text{m}$ considering $\tilde{\mu}_{BG} \approx \mu_p = 1.456$) and

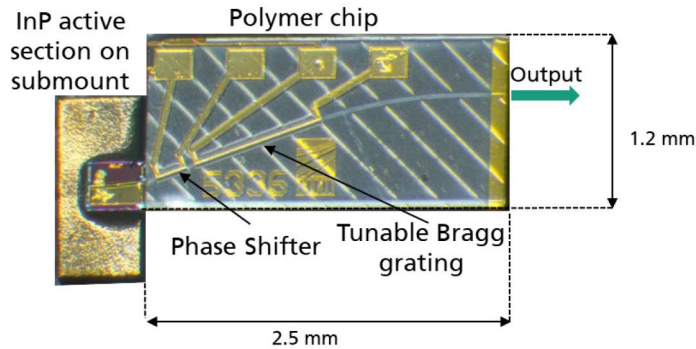


Figure 4.1. Picture of the III-V/polymer tunable DBR laser considered for the study of the high-speed modulation performance.

4. Design Strategies and Performance of III-V/Polymer Tunable DBR Lasers

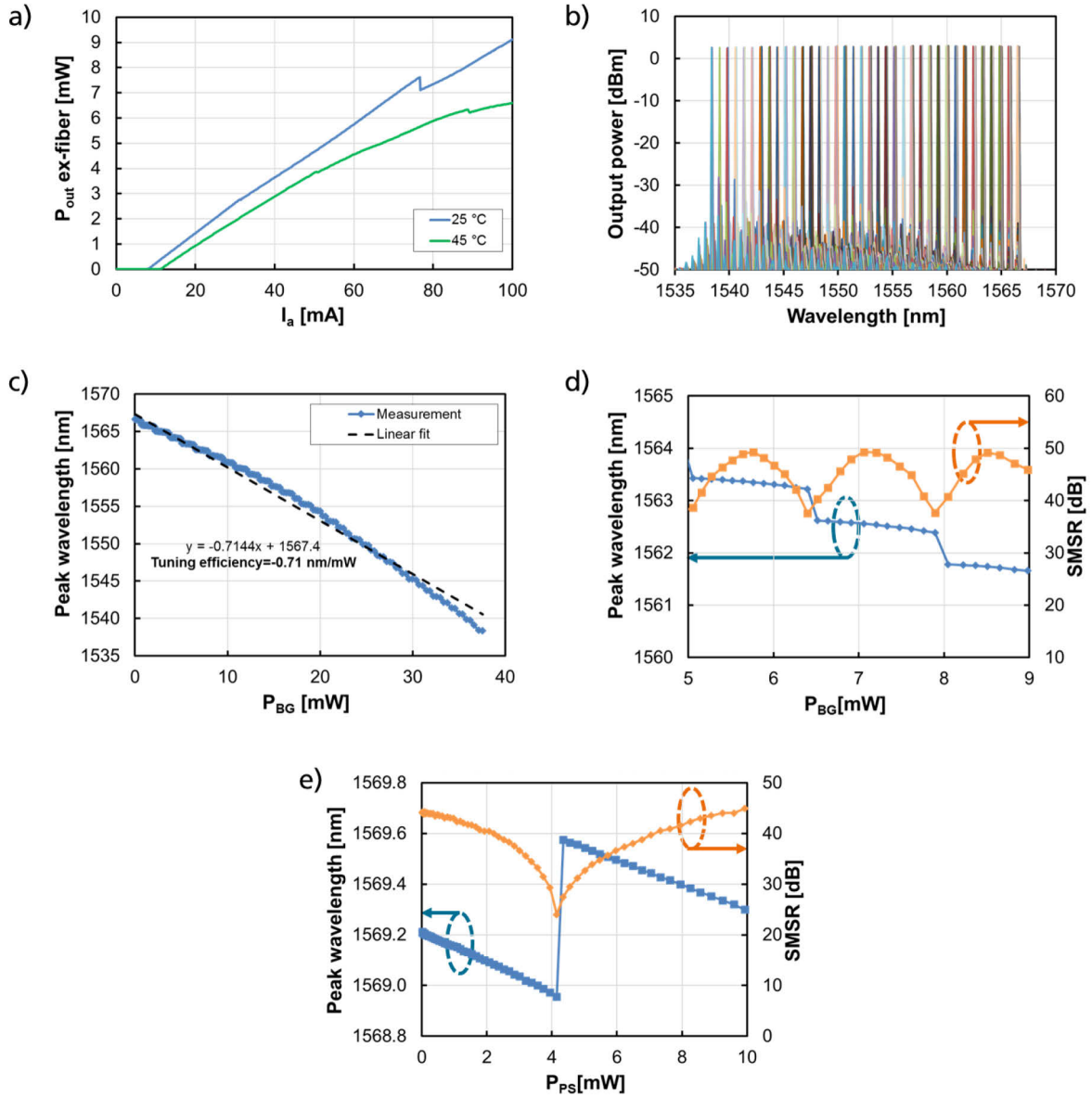


Figure 4.2. Output power and tuning characteristics of the DBR tunable laser considered for the study of the high-speed modulation performance. (a) Measured P-I curve. (b) Superimposed spectra measured scanning the Bragg grating. The current at the gain section was kept to $I_a = 50$ mA, no current was applied on the phase section. (c) Peak lasing wavelength at different heater powers on the Bragg grating (P_{BG}). (d) Peak wavelength and SMSR for a small tuning range of the Bragg grating. (e) Peak lasing wavelength at different heater powers on the phase shifter (P_{PS}). For (b)-(e), the device was operated at a temperature of 45°C.

reflectivity $R_{BG} = 20\%$. With those parameters, the effective length of the passive section $L_{p,eff}$ can be calculated from eq. (3.20) to be $L_{p,eff} = L_{WG} + L_{PS} + L_{eff,BG} = 850$ μm , where the approximation $L_{eff,BG} \approx L_{BG}/2$ for Bragg gratings with moderate reflectivities (see eq. (3.16)) has been considered. An active section as the one described in Section 3.3 with a length $L_a = 400$ μm was used. A picture of the device is shown in Figure 4.1.

4.1.1 Output power and tuning behavior

The power-intensity (P-I) curve measured at the output fiber at 25°C and 45°C is shown in Figure 4.2 (a). No current was applied on the heater sections. The threshold current was measured to be 8.2 mA and 11.2 mA at 25°C and 45°C, respectively. The output power achieved was larger than 9 mW (9.5 dBm) at 25°C and 6.5 mW (8.1 dBm) at 45°C when injecting a current $I_a=100$ mA in the active section. The kinks in the curve observed at around 50 mA at 25°C and 82 mA at 45°C are due to mode hops. These mode hops can be attributed to changes in the refractive index of the active section due to temperature effects. It should be noted that, in the case of applying direct modulation on the active section, those mode hops will not occur if the amplitude modulation frequency is larger than the frequency response of the thermo-optical effect, which typically lies between some hundreds of Hz and some hundreds of MHz [54].

In comparison to other directly-modulated tunable lasers, the delivered output power is similar to that of other polymer-based DBRs (around 9 mW were also demonstrated at 25°C in [55]), and larger than in VCSELs (1.4 mW demonstrated at 20°C in [18]).

In Figure 4.2 (b), the superimposed spectra measured at different electrical powers P_{BG} in the Bragg grating section and for a fixed injection current in the active section of $I_a=50$ mA is shown. The device was temperature-stabilized to 45°C, and the phase section was not driven. As it can be observed, lasing was achieved over more than 25 nm. Notice that, considering the Bragg grating design parameter mentioned above and the thermo-optical coefficient of $-1.1 \times 10^{-4}/\text{K}$, the temperature increase in the Bragg grating T'_{BG} required for the tuning of 25 nm can be calculated from eq. (3.26) to be 214°C. This is beyond the baking temperature of 200°C used in the fabrication process of the polymer waveguide (see Section 3.4.1), and can have a negative influence in the long-term reliability of the device. This aspect will be discussed in more level of detail in Chapter 5.

In Figure 4.2 (c), the lasing wavelengths achieved at the different electrical powers on the Bragg grating micro-heaters P_{BG} are shown, where it can be observed that the 25 nm tuning can be achieved with maximum electrical powers below 40 mW. By means of a linear fit, the tuning efficiency can be extracted to be -0.71 nm/mW.

Tuning only the Bragg grating, mode-hops occur when the wavelength detuning between the lasing mode and the Bragg grating is such that the gain threshold for a neighbor longitudinal mode is lower than that of the previously lasing mode. This phenomenon has been described in Chapter 2. The mode-hops can be well observed in Figure 4.2 (d) as the steps in the wavelength that occur for grating heater powers of around 6.3 mW and 7.9 mW. The wavelength jump in a mode hop equals the mode-spacing of the longitudinal modes. In between two mode-hops, the wavelength of the lasing longitudinal mode varies due to the phase changed induced. Considering eq. (3.28), this variation in the lasing wavelength is attributed to the different value of the effective length of the Bragg grating ($L_{BG,eff}$) under the new detuning conditions, and the variation of the refractive index in the Bragg grating $\tilde{\mu}_{BG}$ induced by temperature increase in the Bragg grating section T'_{BG} .

The induced detuning also affects the SMSR due to the variation in the gain roundtrip conditions of the lasing and neighbor modes. This can also be observed in Figure 4.2 (d). When the wavelength of the lasing mode is close to the Bragg wavelength, the lasing mode will experience the lowest mirror losses and will hence reach the lowest gain threshold condition, while the neighbor modes will experience higher mirror losses with a similar value, yielding to a symmetric and high suppression of the two neighbor modes. In

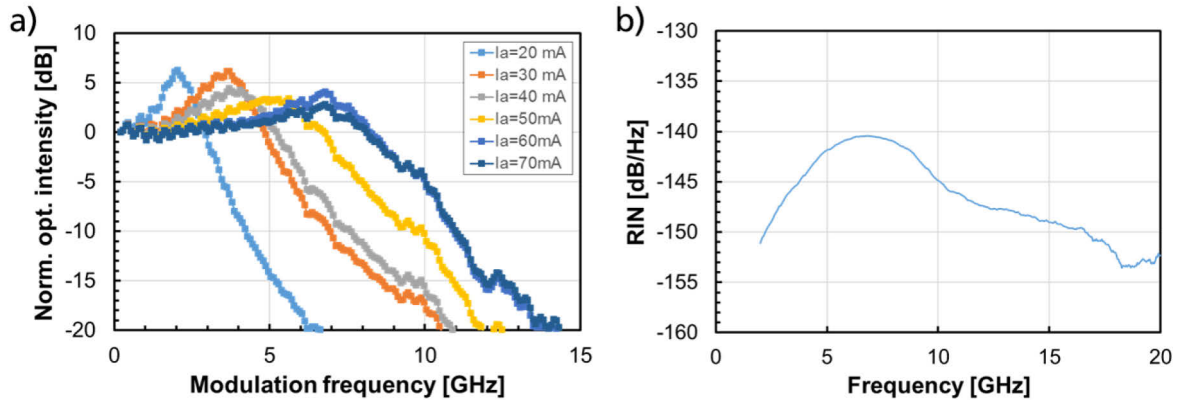


Figure 4.3. (a) Small signal direct-modulation response for different values of the injection current (I_a) of a DBR tunable laser with an effective length of the passive section of $L_{p,eff} = 850 \mu\text{m}$ and a Bragg reflectivity of 20%. (b) RIN spectrum measured at an injection current in the active section $I_a = 70 \text{ mA}$. The device temperature-stabilized at 45°C .

those conditions, an SMSR close to 50 dB can be achieved. When increasing the detuning, the values of the SMSR decrease since the mirror losses of one of the longitudinal modes will decrease, which will cause the gain threshold of that longitudinal mode to decrease.

In Figure 4.2 (e), the lasing wavelength and SMSR as a function of the applied electrical power on the phase shifter, noted as P_{PS} , is shown. Tuning only the phase section, the wavelength of the longitudinal mode and hence the detuning are varied. A mode hop occurs when the detuning induces more favorable gain conditions to a neighbor mode than the previously lasing mode, being the induced jump in the wavelength equal to the spacing between longitudinal modes. Near a mode hop, the SMSR degrades due to the induced detuning. It is worth pointing out that this behavior is periodic with the applied electrical heater power, each period corresponding to an induced roundtrip phase shift of $2\pi \text{ rad}$ (i.e. a phase shift of the phase section of $\pi \text{ rad}$).

4.1.2 Basic small-signal modulation performance

In Figure 4.3 (a), the small signal modulation response for different injection currents in the active section, I_a , are shown. The phase section and Bragg grating were not driven for these tests (i.e. $P_{PS} = P_{BG} = 0 \text{ mW}$). The relaxation oscillation frequency, and hence the modulation bandwidth, increases with the output power, as expected from eq. (2.40), and therefore increases with the injection current in the active section I_a . For an injection current of $I_a = 70 \text{ mA}$, the relaxation oscillation frequency f_r amounts to around 7 GHz, and the 3-dB modulation bandwidth f_{3dB} 8.6 GHz. The achieved results show the potential suitability of this device for 10 Gbaud amplitude modulation formats. Large signal modulations at this rate will be covered in Chapter 6. The achieved modulation bandwidth is slightly larger than that of directly modulated VCSELs reported in [18], which amounted to around 7 GHz, and in the III-V/Si tunable laser implementation reported in [20], which amounted to 7.22 GHz. A similar implementation of III-V/polymer tunable DBR tunable lasers reported in [27] showed a f_{3dB} of 8 GHz, very similar to the result reported in this work.

Comparison with theory: in order to compare the measured relaxation oscillation frequency and the expected values from the theory exposed in Subsection 2.5.2, let us calculate first as a reference the relaxation oscillation frequency f_{r0} of the reference solitary semiconductor laser comprising only the active

section. The reflectivity on the rear-end mirror will be considered to be $R_1 = r_1^2 = 0.95$, and the reflectivity R in the front end mirror will be considered to be the same as the effective reflectivity in the case of the external cavity laser configuration, which from eqs. (2.32) and (3.3) can be expressed as $R = r^2 = \max(|r(\omega)|^2) = \alpha_c^2 \exp(-2\alpha_p L_p) R_{BG}$. Assuming the coupling efficiency between the passive and active section to be $\alpha_c = 0.79$ (corresponding to the 1 dB coupling losses as obtained by simulations in Subsection 3.5.2), propagation losses in the polymer waveguide of 0.7 dB/cm (i.e. $\alpha_p \sim 16.1 \text{ m}^{-1}$), and a Bragg reflector featuring a reflectivity of $R_{BG} = 20\%$, the effective reflectivity can be obtained to be $R = 12.4\%$. With those values, the mirror losses can be calculated from eq. (3.17) to be $\langle \alpha_m \rangle = 2671.7 \text{ m}^{-1}$. To obtain the value for the total output power P_{tot} at the exit of the Bragg grating, it will be considered as a first approximation that the reflector at the rear-end of the active section is perfect, and that the coupling efficiency between the output polymer waveguide and the cleaved single-mode fiber (SMF) is 1 dB. With those considerations, and taking into account the output power measured at the output fiber of 5.5 mW that can be extracted from Figure 4.3 (a) at an injection current $I_a = 70 \text{ mA}$, a P_{tot} of 6.9 mW can be calculated for the case of $I_a = 70 \text{ mA}$. Using the calculated values for $\langle \alpha_m \rangle$ and P_{tot} , and considering the parameters of the active section summarized in Appendix E, the relaxation oscillation frequency f_{r0} of the solitary semiconductor laser can be calculated from eq. (2.40) to be $f_{r0} = 9 \text{ GHz}$. To obtain the relaxation oscillation frequency f_r of the DBR laser, the relation between f_{r0} and f_r , which is given as a function of the parameters A and B by eq. (2.41), can be used. For this calculation, B will be considered to be zero (i.e. no detuning). Additionally, it will be assumed that gain rates for the case of the solitary and external cavity lasers (G and G_0 , respectively) are equal, meaning that the external feedback does not modify significantly the photon lifetime (i.e., the optical length of the passive section of the cavity is short in comparison to the optical length of the active section). This is a good approximation for the case of the short polymer passive section with low effective refractive index featured by the device under consideration. With those assumptions, the parameter A was calculated using eq. (3.23) considering $\tilde{\mu}_{g,BG} = \mu_{g,p} = 1.456$, yielding to a relaxation oscillation frequency f_r calculated from eq. (2.41) to be around 6.7 GHz. This is in good agreement with the measured 7 GHz. The higher measured f_r in comparison to theory might be attributed to the effect of detuning, which is accounted for by the parameter B . As it was discussed in Subsection 2.5.2., adequate detuning can result in an enhancement of f_r .

Besides the modulation bandwidth, and as it was discussed in Subsection 2.5.3, the relative intensity noise has also an influence on the modulation performance. RIN measurements were performed using the method described in [56], which consists on detecting the laser output with a photodetector and measuring the frequency spectrum with a microwave spectrum analyzer. In Figure 4.3 (b), a RIN curve for the case of an injection current in the active section 70 mA is shown. As in the measurement of the modulation response, the device was temperature-stabilized at 45°C. As it can be observed, the relaxation oscillation frequency of the laser can be measured to be around 7 GHz, in good agreement with the result extracted from the small-signal modulation response in Figure 4.3 (a). The peak RIN value at the relaxation oscillation frequency amounts to around -141 dB/Hz.

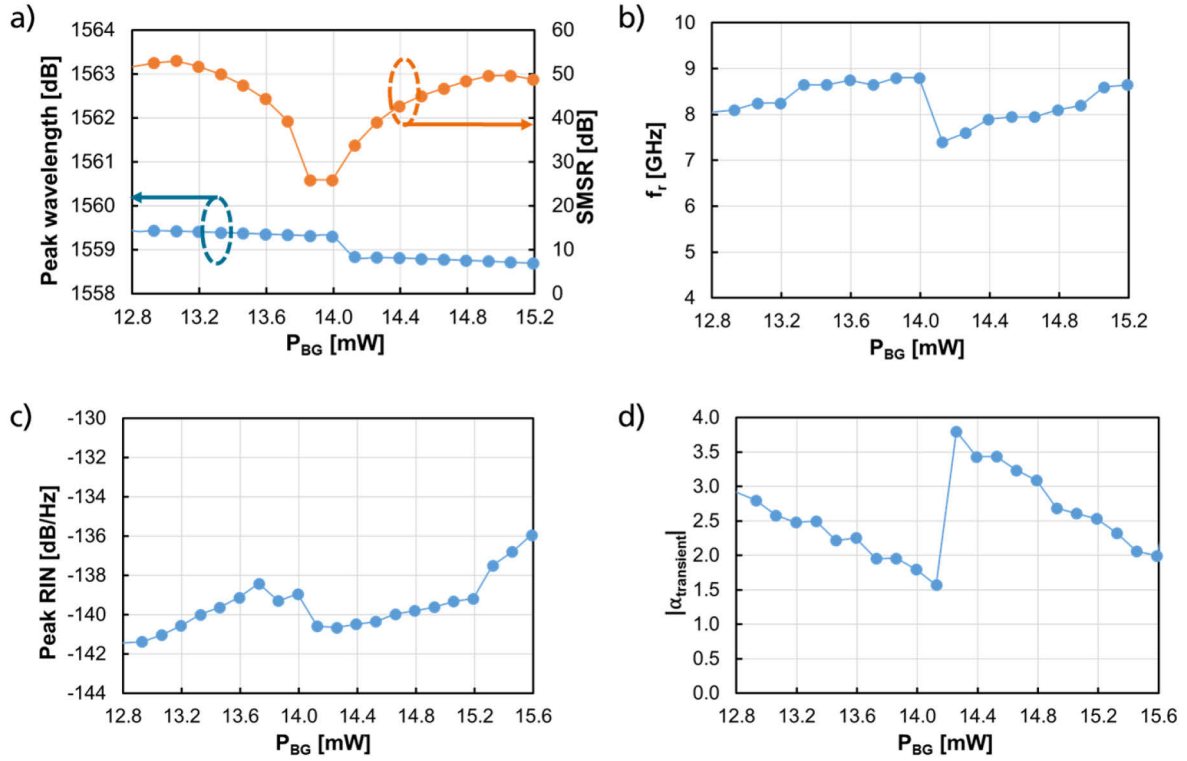


Figure 4.4. (a) Measured wavelength and side-mode suppression ratio (SMSR), (b) relaxation oscillation frequency (f_r), (c) peak relative intensity noise (RIN) at the relaxation oscillation frequency, and (d) transient chirp factor measured ($\alpha_{transient}$), while finely tuning the electrical power on the Bragg grating (P_{BG}). The injection current in the active section was fixed to 70 mA, and the electrical heater power on the phase section was kept constant. The device temperature was set to 45°C. (a)-(c) were measured during the same measurement run, whereas (d) was measured in a separate run.

4.1.3 Effect of detuning

As mentioned above, a possible reason for the deviation between the theoretical and experimental measurements of the relaxation oscillation frequency f_r , discussed in the previous subsection is the effect of the detuning, which is accounted for by parameter B . Investigations were performed in order to study the influence of the detuning on the modulation performance of the DBR tunable laser. In Figure 4.4 (a), the wavelength and the SMSR are shown for a fine tuning of the electrical powers in the Bragg grating micro heater (P_{BG}). The phase section remained constant, and the temperature of the device was stabilized at 45°C. A mode-hop occurs at around $P_{BG} = 14$ mW, as it can be observed by the discontinuity in the measured lasing wavelength.

Recalling, due to the negative TOC of the polymer material, an increase in the heater power P_{BG} (and hence in the temperature) shifts the polymer Bragg grating towards shorter wavelengths. Considering this, it is straightforward to deduce that, after a mode-hop, the detuning will be such that the new lasing mode will be at the shorter wavelength side of the Bragg grating (as it was depicted in Figure 3.4 (a)), which translates in a low SMSR value. While further tuning the Bragg grating, the detuning will be reduced until it reaches zero value (as it was depicted in Figure 3.4 (b)), showing a maximum SMSR value. Continuing to tune the Bragg grating from the point of zero detuning will induce the lasing mode to be on the longer

wavelength side of the Bragg grating (as it was depicted in Figure 3.4 (c)), hence inducing a decrease of the SMSR until the next mode-hop takes place. As it was discussed in Subsection 3.2.2, these effects of detuning can be seen as variations in the parameter B . After a mode hop, the parameter B shows a negative value since the longitudinal mode is at a higher frequency (i.e. shorter wavelength) than the Bragg grating. When reaching the zero detuning, the value of the parameter B will be zero. Continuing to tune the Bragg grating increase the parameter B will towards positive values since lasing mode is at a lower frequency (i.e. longer wavelength) than the Bragg grating, until the next mode-hop occurs.

In Figure 4.4 (b), the relaxation oscillation frequency f_r extracted from the RIN spectra is shown for different electrical powers at the Bragg section. As it can be observed, f_r varied between 7.3 GHz and 8.8 GHz. The relaxation oscillation shows a minimum value after a mode hop occurs, and increases when the laser is tuned towards a mode hop. This can be attributed to variations in the external feedback parameter B . After a mode hop, the detuning parameter B will be negative, hence acting negatively on f_r . Tuning the Bragg grating will cause the parameter B to reduce until it reaches zero for no detuning, and will continue to increase towards positive values when approaching a mode-hop. As it was discussed in Subsection 2.5.2, this increase of the parameter B results in an increase of the relaxation oscillation frequency f_r .

In Figure 4.4 (c), the RIN value at the relaxation oscillation frequency is shown. It can be seen that the RIN varied between -142 dB/Hz and -136 dB/Hz, and that there is an increasing trend when tuning the laser towards the next mode hop, and decreases after a mode-hop occurs. The increasing trend in RIN when tuning the Bragg grating towards a mode-hop can be attributed to an increase of the parameter B from negative to positive values while tuning only the Bragg grating. As it was discussed in Subsection 2.5.2, increasing B will result in the reduction of the damping rate γ . As given by eq. (2.45), the peak RIN is inversely proportional to the square of the damping rate, and hence will increase with an increase of the parameter B [36].

In Figure 4.4 (d), the measured transient linewidth enhancement factor $\alpha_{transient}$ is shown. This parameter was measured following the method described in [57] by means of modulating the active section at 10 GHz, and extracting the intensity and phase and amplitude modulation indices. Let us recall from Subsection 2.5.4 that, under these high-speed modulation conditions, the dominant linewidth enhancement factor is the transient contribution $\alpha_{transient}$, which can be expressed as a function of Henry's linewidth enhancement factor of the active section α and the external cavity parameters A and B as given by eq. (2.49). It should be noted that this measurement was performed separately to the wavelength, SMSR, f_r and RIN, which lead to small difference with respect to the values of P_{BG} at which the mode hops occurred. The obtained values $\alpha_{transient}$ varied between 3.5 after a mode hop to 1.5 before a mode hop. As for the case of f_r and the RIN, the reason of this variation can be attributed to variations in the parameter B from negative values (after a mode hop) to positive values (when approaching a mode hop), as it is expected from the discussions in Subsection 2.5.4.

As a conclusion of the measurements from Figure 4.4, notice that, as expected from the theory covered in Subsections 2.5.2 and 2.5.4, the detuning induces an increase in the relaxation oscillation frequency f_r , and a decrease in the transient linewidth enhancement factor $\alpha_{transient}$. This means that the modulation bandwidth and the chirping of the source can both be improved simultaneously by means of detuning. However, the increase in the detuning provides an increase in the RIN (as seen in Figure 4.4 and as expected from the theory in Subsection 2.5.3). Notice also that, as expected from the theory in Subsection 2.5.2, the

damping rate is also decreased for an induced tuning. This information is useful for setting the operation point of the tunable laser, since it will allow finding an adequate settings either for maximum modulation performance in terms of modulation bandwidth and chirp, or for minimum RIN and maximum damping rate. Minimizing the detuning will allow for a trade-off between those three parameters.

4.1.4 Considerations towards optimization of the modulation performance

In order to further improve the direct-modulation characteristics of the DBR laser considered in this section, some hints can be extracted considering the theory covered in Section 2.5. A first approach is to reduce the effective length of the passive section $L_{p,eff}$ in order to further reduce the parameter A . This would allow increasing the relaxation oscillation frequency, decreasing the damping rate, and hence decreasing the RIN. However, reducing the length of the passive section will allow in the best case for relaxation oscillation frequencies close to the relaxation oscillation frequency of the equivalent solitary semiconductor laser, which as calculated in Subsection 4.1.2, amounted to $f_{r0}=9$ GHz.

Another approach to increase the modulation performance would be to exploit the effect of the detuning, which allows changing the external feedback parameter B . Increasing B will simultaneously increase the relaxation oscillation frequency and reduce the transient linewidth enhancement factor. However, it should be noted that increasing B induces also an increase in the RIN. An increase of the B parameter might be achieved by means of reducing the length of the active and passive sections, what would increase the mode spacing and potentially enable a larger detuning before a mode-hop occurs.

4.2 Narrow linewidth

As it has been seen in the theoretical discussions on the linewidth provided in Subsection 2.5.5, the linewidth in an external cavity semiconductor laser is inversely proportional to the reduction factor F^2 , being $F = 1 + A + B$. Hence, increasing the length of the active section (i.e. increasing A) will result in a reduction of the linewidth. Additionally, the detuning can cause the parameter B to be positive (by means of setting the lasing mode at a longer wavelength side from the central wavelength of the Bragg reflector), and hence further reduce the linewidth of the device.

To study the linewidth of the DBR, a device comprising a longer passive section than the high-speed device considered in Section 4.1 was considered. The DBR laser featured $L_{WG}=300$ μm , $L_{PS}=600$ μm , and $L_{BG}=1250$ μm . With those parameters, the effective length of the passive section can be calculated to be $L_{p,eff} = L_{WG} + L_{PS} + L_{BG,eff} \approx 1525$ μm , where it has been considered that $L_{BG,eff} \approx L_{BG}/2$. The Bragg grating was designed at 1570 nm (i.e. $\Lambda=1.617$ μm considering $\tilde{\mu}_{BG} \approx \mu_p=1.456$) and showed a reflectivity R_{BG} of 20%. The length of the active section was $L_a=400$ μm .

4.2.1 Output power and tuning behavior

The P-I curve measured ex-fiber at 45°C is shown in Figure 4.5 (a). The phase shifter and Bragg grating heaters were not driven. The threshold current was measured to be around 10 mA, and the ex-fiber output power achieved was larger than 7.5 mW (8.45 dBm) injecting a current $I_a=100$ mA in the active section.

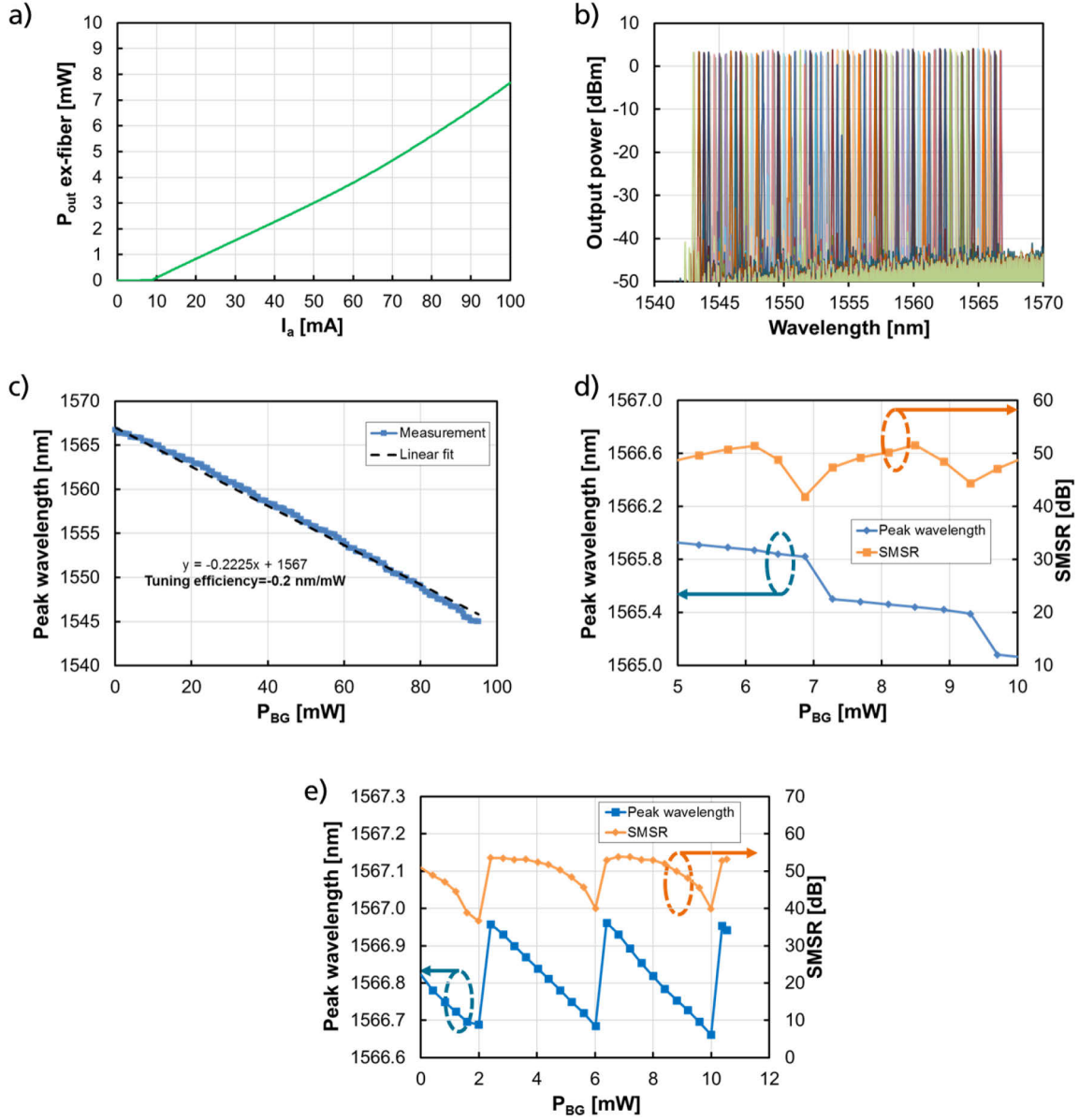


Figure 4.5. Output power and tuning characteristics of the DBR tunable laser with an effective length of the passive section of $L_{p,eff} = 1525$ μm , a Bragg grating reflectivity of 20%, and an active section with length 400 μm . (a) Measured P-I curve. (b) Superimposed spectra measured scanning the Bragg grating. The current at the gain section was kept to $I_a = 50$ mA, and no current was applied on the phase section. (c) Peak lasing wavelength at different heater powers on the Bragg grating (P_{BG}). (d) Peak wavelength and SMSR for a small tuning range of the Bragg grating. (e) Peak lasing wavelength at different heater powers on the phase shifter (P_{PS}). For all measurements the device was stabilized at a temperature of 45°C.

Figure 4.5 (b) shows the superimposed spectra measured at different driving currents in the grating section and for a fixed injection current in the active section of $I_a = 50$ mA and device temperature of 45°C. During this measurement, the phase section was not driven. As in the case of the high-speed device considered in Section 4.1, the tuning range was beyond 20 nm. In Figure 4.5 (c), the lasing wavelengths achieved at the different electrical powers on the Bragg grating micro-heater (P_{BG}) are shown. The required

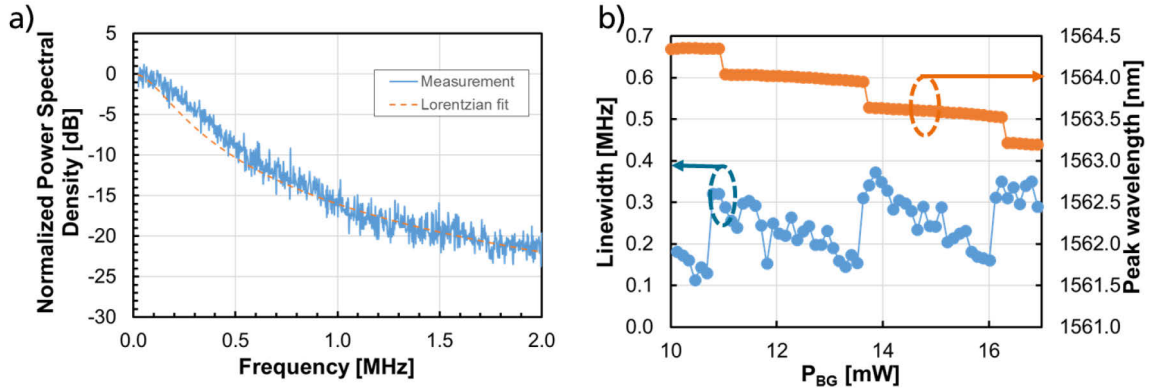


Figure 4.6. (a) Measured linewidth and Lorentzian fit at 1565 nm of the DBR tunable with an effective length of the passive section of $L_{p,eff} = 1525 \mu\text{m}$, a Bragg grating reflectivity of 20%, and an active section with length 400 μm . (b) Measured wavelength and 3-dB linewidth while tuning the Bragg grating along two mode-hops. The device was stabilized at a temperature of 45°C, and the injection current in the active section was set to 80 mA.

electrical power on the Bragg grating micro-heater to achieve 25 nm tuning amounts to around 90 mW, and the tuning efficiency can be extracted by means of a linear fit to be -0.22 nm/mW.

Figure 4.5 (d) shows the wavelength and SMSR for a small variation of P_{BG} . As it can be seen, SMSR values larger than 50 dB can be achieved between two mode hops.

In Figure 4.5 (e), the lasing wavelength and SMSR as a function of the applied electrical power on the phase shifter is shown. Several 2π roundtrip shifts can be achieved with due to the long phase section used in this device. As for the case of fine tuning of the Bragg grating (Figure 4.5 (d)), the tuning of the phase section allows achieving SMSR values larger than 50 dB when minimizing the detuning.

4.2.2 Linewidth and effect of detuning

The measured linewidth of a semiconductor laser is determined by two factors. Firstly, the intrinsic phase noise caused by spontaneous emission events and amplitude-phase coupling, which yield the linewidth equation (2.52). This noise contribution can be generally considered a white noise source [41], and yields to a power spectral density of the electrical field (also referred to as the spectral line shape) that obeys a Lorentzian function [36]. Secondly, low-frequency effects such as noise in the current sources, temperature variations and mechanical vibrations [40], show a power spectral density with a $1/f$ frequency dependence, and are hence called $1/f$ noise contributions [58]. These $1/f$ noise contributions yield to an electrical field with a line shape that obeys a Gaussian function [36]. When considering coherent optical communications systems at high baud rates, the Lorentzian contribution to the line shape of the electrical field, which is the one that will affect the high frequencies due to its white power spectral density, has a predominant influence [58].

For the measurements in this section, the spectral lines shapes were measured using a self-homodyne method [59], where the used Mach-Zehnder interferometer had a path difference length of 6.4 km. Figure 4.6 (a) shows the measured linewidth and Lorentzian fit at a wavelength of 1565 nm. The device temperature was stabilized to 45°C. The currents at the active and phase sections were set to $I_a = 80 \text{ mA}$, which considering the P-I curve shown in Figure 4.5 (a) corresponds to an output power ex-fiber of 5.7 mW. From the Lorentzian fit, a linewidth of 160 kHz can be extracted. The deviations between measured

and fitted data might be due to $1/f$ frequency contributions such as noise in the current sources, and/or temperature instabilities.

To evaluate the effect of the detuning, Figure 4.6 (b) shows the measured linewidth for a fine-tuning of the Bragg grating. As it can be observed, the linewidth has a decreasing trend when the laser is tuned towards a mode-hop, where linewidth values as low as 130 kHz were achieved. The reduction in the linewidth can be attributed to the fact that tuning of the Bragg grating modifies the detuning, and causes an increase in the parameter B from negative to positive values. This induces the parameter B to increase towards positive values when approaching a mode hop, which causes an increase in the parameter $F = 1 + A + B$, to which the linewidth reduces quadratically (see eq. (2.52)).

Comparison with theory: in order to compare the measured linewidth and the expected values from the theory exposed in Subsection 2.5.5, let us consider first a reference solitary semiconductor laser comprising only the active section. The reflectivity on the rear-end mirror will be considered to be $R_1 = r_1^2 = 0.95$, and the reflectivity R in the front end mirror will be defined to be the same as the effective reflectivity in the case of the external cavity laser configuration, which from eqs. (2.32) and (3.3) can be expressed as $R = r^2 = \max(|r(\omega)|^2) = \alpha_c^2 \exp(-2\alpha_p L_p) R_{BG}$. Assuming the coupling efficiency between the passive and active section to be $\alpha_c = 0.8$ (corresponding to the 1 dB coupling losses as obtained by simulations in Subsection 3.5.2), propagation losses in the polymer waveguide of 0.7 dB/cm (i.e. $\alpha_p \sim 16.1 \text{ m}^{-1}$), and a Bragg reflector featuring a reflectivity of $R_{BG} = 20\%$, the effective reflectivity can be obtained to be $R = 12.3\%$. With those values, the mirror losses can be calculated from eq. (3.17) to be $\langle \alpha_m \rangle = 2688 \text{ m}^{-1}$. Considering coupling losses of 1 dB (i.e. coupling efficiency 80%) between the output polymer waveguide and the output fiber, a P_{out} at the exit of the Bragg grating of 7.1 mW can be calculated for the case of $I_a = 80 \text{ mA}$ considering the ex-fiber output power of 5.7 mW (extracted from Figure 4.3 (a)). For the active section, the following typical parameters at 1550 nm for InGaAsP MQW (summarized in Appendix E) will be considered: effective group index $\mu_{g,a} = 3.8$, transversal spontaneous emission enhancement factor $K_{xy} = 1$, spontaneous emission factor $n_{sp} = 1.5$, losses in the active section $\alpha_a = 1750 \text{ m}^{-1}$, and linewidth enhancement factor $\alpha = 2.5$. The linewidth of the reference solitary semiconductor laser can be calculated from eq. (2.51) to be $\Delta\nu_0 = 1.6 \text{ MHz}$. To obtain the linewidth $\Delta\nu$ of the DBR laser, the relation between $\Delta\nu_0$ and $\Delta\nu$, which according to eq. (2.52) is given as a function of the parameters A and B by $\Delta\nu = \Delta\nu_0 / (1 + A + B)^2$, can be used. For this calculation, B will be considered to be zero for simplicity (i.e. zero detuning). From this expression, and considering the approximation of A for no detuning given by eq. (3.23), the value of $\Delta\nu$ can be obtained to be 268 kHz, which is good agreement with the measured linewidths in Figure 4.6 (b).

The achieved minimum linewidths of 130 kHz are comparable to the III-V/Si₃N₄ tunable laser implementation on the TriPleX ultra-low-loss waveguide platform reported in [60], which showed a linewidth of 64 kHz. III-V/Si C-band tunable laser implementations have shown linewidths of around 5 kHz [21], relying on the high effective lengths of the passive (i.e. large external cavity parameter A) achievable with high-quality-factor ring resonators in the high-contrast silicon waveguides. In monolithic implementations, InP-based C-band tunable lasers with linewidths of around 200 kHz have been

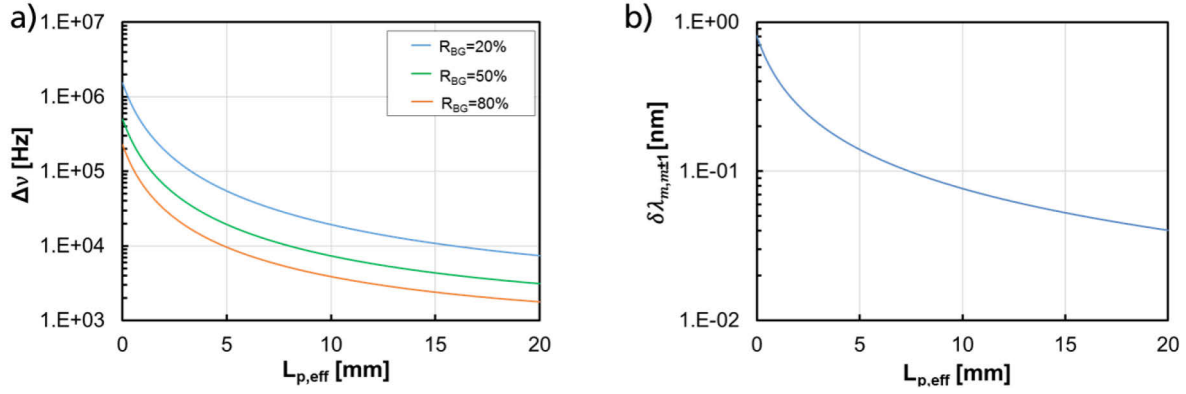


Figure 4.7. (a) Calculated linewidth for different effective lengths of the passive section and different reflectivities on the Bragg grating considering a passive section with length $400\ \mu\text{m}$. The emitted output power at the exit of the Bragg grating was considered to be of $7.1\ \text{mW}$. (b) Mode spacing for the different effective lengths of the passive section.

demonstrated in coherent transmitter PICs comprising arrays of I/Q modulators [15]. With those devices, 44 GBaud 16-QAM modulation was demonstrated, which hints to the potential usability of the DBR laser presented in this section in coherent high-speed communications given the narrower linewidths achievable.

4.2.3 Considerations towards further reduction of the linewidth

Increasing further the optical length of the passive section (i.e. A) and increasing the detuning (i.e. B) would allow for a further linewidth reduction. For the theoretical investigations on further strategies to reduce the linewidth, it will be considered for simplicity that the lasing mode is perfectly tuned with the Bragg grating (i.e. $B=0$). Additionally, as in the theoretical calculations performed in the previous section, an output power at the exit of the Bragg grating of $7.1\ \text{mW}$ will be considered.

Figure 4.7 (a) shows the linewidth calculated using eq (2.52) for different effective lengths of the passive section $L_{p,eff}$ and different reflectivities of the Bragg grating R_{BG} . For the calculation of the parameter A , eq. (3.23) was used, where it is worth recalling that the group index of the Bragg grating ($\tilde{\mu}_{g,BG}$) can be approximated to the group index of the polymer waveguide ($\mu_{g,p}$). As it can be observed, considering the reflectivity of 20 % used in the device discussed in this section, a linewidth narrower than 10 kHz might be achieved increasing the effective length of the passive section to around 1.6 cm. Increasing the reflectivity of the Bragg grating to more than 50%, a reflectivity of 10 kHz might be achieved with effective lengths of the passive section of 8 mm. The reduction of the linewidth when increasing the reflectivity is due to the decrease in the mirror losses. Following this strategy would allow achieving linewidths in the range of the 15 kHz demonstrated in the III-V/Si tunable laser reported in [21].

Nevertheless, it should be noted that increasing the length of the passive section comes with a reduction of the mode spacing, which implies that a reduction of the bandwidth of the Bragg grating would be necessary. In Figure 4.7 (b), the mode spacing calculated from eq. (3.19) is shown. For a polymer external cavity of 2 cm, the mode spacing reaches a value of around 40 pm. This value makes the filtering requirements of the polymer-based Bragg grating very stringent to ensure single-mode operation. Therefore, before going to such long passive sections, increasing the parameter B might be a more practicable alternative. Besides increasing B by means of increasing the allowed detuning, the use of

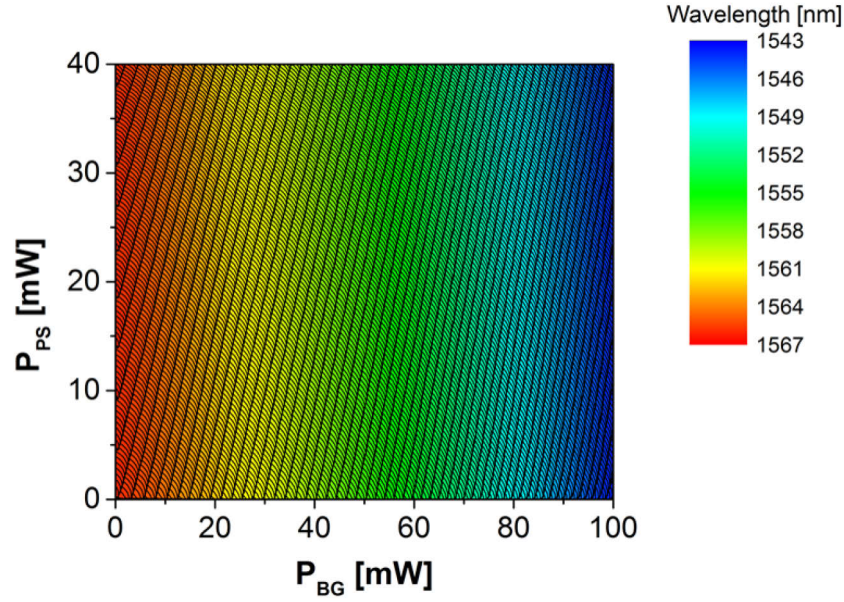


Figure 4.8. Wavelength map of a DBR laser as a function of the electrical power on the Bragg grating and phase electrodes. The measured device featured an active section with a length of L_a 400 μm , a phase shifter with a length of L_{PS} =600 μm , a Bragg grating with a length L_{BG} =1250 μm , and interconnecting passive waveguides with a total length of L_{WG} =300 μm . The device was temperature-stabilized at 45°C.

controlled feedback from a third reflector outside of the main laser cavity has been shown in [61] to be an attractive method. The use of a third reflector can allow both varying A and B to achieve an increase in F^2 . The strength of this variation might be controlled by means of varying the intensity of the optical feedback, as well as the phase. This allowed in [61] achieving linewidths in III-V/Si tunable lasers of around 50 kHz.

4.3 Enhanced continuous tuning

As it has been seen in the previous sections, tuning separately the Bragg grating and the phase shifter induces mode-hops due to the induced detuning. Since, as expected from eq. (3.18), tuning the Bragg grating and the phase section induces a tuning of the longitudinal modes, it is expected that, by means of and adequate control of both the phase shifter and Bragg grating, the detuning can be controlled in such a way that mode-hops do not occur. In order to see this graphically, let us consider the two-dimensional wavelength map as a function of heater power in the phase section (P_{PS}) and the Bragg grating (P_{BG}) shown in Figure 4.8. The measured device showed the same design parameters as the narrow linewidth device considered in the previous section (L_a = 400 μm , L_{WG} = 300 μm , L_{PS} =600 μm , and L_{BG} =1250 μm). The combinations of P_{PS} and P_{BG} at which mode hops occur are to be seen in the graph as the thick black lines, and follow a diagonal trajectory. Those diagonal lines can be therefore understood as mode-hop boundaries, and two of such consecutive diagonal lines delimit mode-hop free areas. Therefore, varying P_{PS} and P_{BG} in a way that a trajectory is followed between two mode-hop boundaries, continuous tuning will be achieved. If besides avoiding the mode-hops, the SMSR is intended to be kept constant, the detuning needs to be maintained, and therefore the trajectories have to be parallel to the mode-hop boundaries.

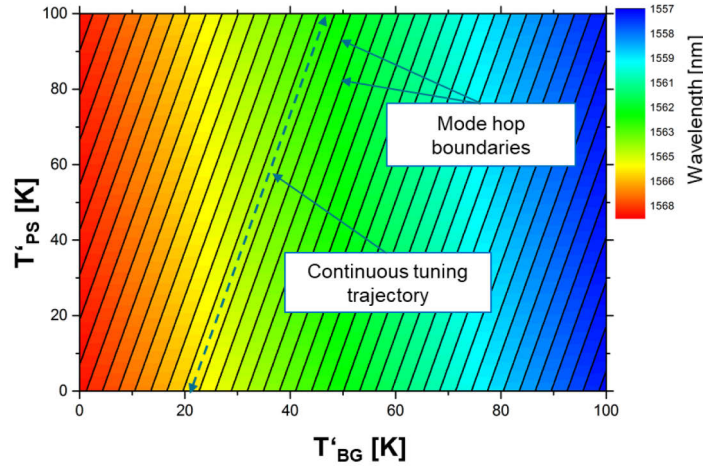


Figure 4.9. Calculated wavelength of a III-V/polymer DBR laser as a function of the temperature increase in the phase (T'_{ps}) and Bragg grating sections (T'_{BG}).

In this section, the analytical procedure to define those continuous tuning trajectories is presented, and the design strategy to achieve the largest possible continuous tuning is discussed. Finally, experimental results are presented.

4.3.1 Theory of continuous tuning in thermo-optically tunable DBR lasers

Due to the linear relation between electrical power on the micro-heaters and the achieved temperature increase [62], a wavelength map as a function of the temperature is equivalent to the wavelength maps as a function of the heater powers. As an example, Figure 4.9 shows a calculated wavelength map of a III-V/polymer DBR as a function of the temperature variation induced in the Bragg and phase sections, T'_{BG} and T'_{ps} respectively, where the maximum temperature increase has been limited to 100°C in order to ease the graphic interpretation of the mode-hop boundaries and continuous tuning trajectories. As it can be observed, linear diagonal mode-hop boundaries can also be defined, and variations in the temperature of the Bragg grating and phase section following trajectories between those mode-hop boundaries will allow for continuous tuning.

Let us start setting as a boundary condition a certain maximum temperature in the phase and Bragg grating sections $T'_{max}=175^{\circ}\text{C}$. If the device is temperature-stabilized at 25°C , a maximum temperature of 200°C will be reached in the waveguide, which is the baking temperature used in the curing and cross-linking processes of the polymer layers during fabrication (see Subsection 3.4.1). The linear continuous tuning trajectories as a function of temperature can be defined by a certain slope, from now on noted as $s_{T,cont}$, which relates the variations in the temperature in the phase section $\Delta T'_{ps}$ and the Bragg grating section $\Delta T'_{BG}$ that are required in order to ensure keeping an constant detuning value. Therefore, $s_{T,cont}$ can be mathematically defined as

$$s_{T,cont} = \frac{\Delta T'_{ps}}{\Delta T'_{BG}}. \quad (4.1)$$

Notice that, in order to ensure the largest continuous tuning range possible for a given maximum increase in the temperature of T'_{max} , it should be targeted that $s_{T,cont}$ has a value as close as possible to one, since this will imply that both the reflector and the longitudinal modes are tuned with the same efficiency. Values of $s_{T,cont}$ larger than one will imply that the tuning efficiency of the longitudinal modes is lower than that of the Bragg grating, and therefore the maximum continuous tuning range will be limited by the maximum wavelength tuning achievable with the longitudinal modes. If $s_{T,cont}$ has a value lower than one, it will imply that the tuning efficiency of the Bragg grating is lower than that of the longitudinal modes, and hence the maximum continuous tuning will be limited by the maximum tuning achievable with the Bragg grating with a temperature increase of T'_{max} .

For the analytic calculation of the continuous tuning slope $s_{T,cont}$, let us obtain from eq. (3.26) the wavelength variation induced on the Bragg wavelength, noted as $\Delta\lambda_{BG}$, which is induced by means of a certain temperature change $\Delta T'_{BG}$:

$$\Delta\lambda_{BG} = \frac{2}{m_{BG}} TOC \cdot \Lambda \cdot \Delta T'_{BG}. \quad (4.2)$$

The wavelength variation in the longitudinal modes, from now on noted as $\Delta\lambda_m$, can be obtained in a straightforward way from eq. (3.28), yielding

$$\Delta\lambda_m = \frac{2}{m} [TOC \cdot L_{PS} \cdot \Delta T'_{PS} + TOC \cdot L_{BG,eff} \cdot \Delta T'_{BG}]. \quad (4.3)$$

For continuous tuning, it is convenient that the detuning value is kept constant in order to avoid setting the laser at operation points that are close to a mode hop. This is the same to say that, for continuous tuning, it is convenient to set as a boundary condition that the wavelength variation in the Bragg grating equals the wavelength variation in the longitudinal mode, i.e. $\Delta\lambda_{BG} = \Delta\lambda_m$. This condition results in continuous tuning trajectories parallel to the mode-hop boundary. Using this boundary condition, and equalizing the expressions (4.2) and (4.3), an expression for $\Delta T'_{PS}$ as a function of $\Delta T'_{BG}$ to ensure continuous tuning can be obtained:

$$\Delta T'_{PS} = \frac{m}{TOC} \left[\frac{1}{m_{BG}} (TOC \cdot \Lambda \cdot \Delta T'_{BG}) - \frac{1}{m} TOC \cdot L_{BG,eff} \cdot \Delta T'_{BG} \right]. \quad (4.4)$$

Plugging eq. (4.4) into eq. (4.1) allows obtaining the following expression for s_T :

$$s_{T,cont} = \frac{1}{L_{PS}} \left(\frac{m}{m_{BG}} \Lambda - L_{BG,eff} \right). \quad (4.5)$$

To further study the design rules that can allow tailoring $s_{T,cont}$, it is convenient to write $s_{T,cont}$ as a function of intrinsic geometrical and material parameters of the laser cavity. In order to do so, let us consider the following expressions for m and Λ , which can be obtained from eq. (3.18) and (3.6), respectively:

$$m = \frac{2(\mu_a L_a + \mu_p L_{WG} + \mu_p L_{PS} + \tilde{\mu}_{BG} L_{BG,eff})}{\lambda} \quad (4.6)$$

4. Design Strategies and Performance of III-V/Polymer Tunable DBR Lasers

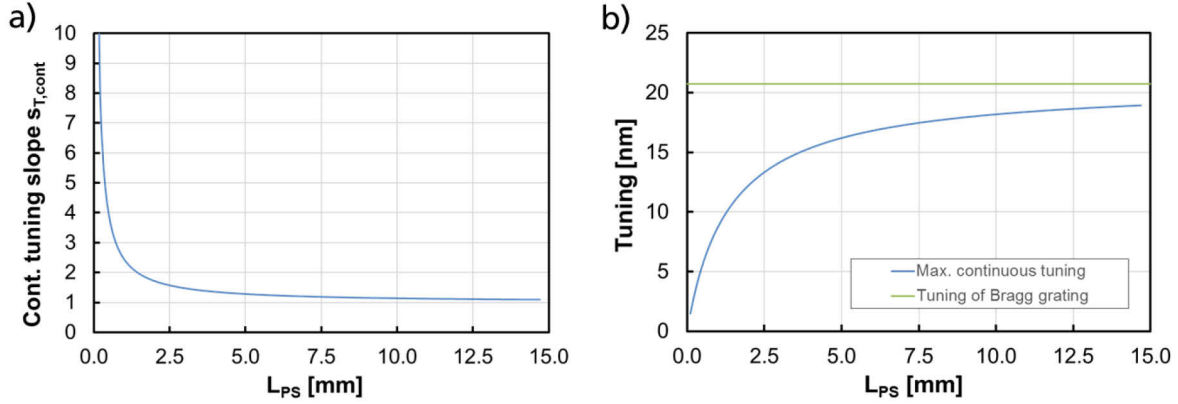


Figure 4.10. (a) Calculated continuous tuning slope and (b) maximum continuous tuning range for a III-V/polymer DBR tunable laser operating at a starting wavelength of 1570 nm. For the calculation $L_a=400 \mu\text{m}$ and $L_{WG}=300 \mu\text{m}$. As boundary condition, the maximum tolerated temperature increase in the polymer material was set to 175°C .

$$\Lambda = \frac{m_{BG} \lambda_{BG}}{2\tilde{\mu}_{BG}}. \quad (4.7)$$

Using eqs. (4.6) and (4.7) in eq. (4.5), and assuming $\lambda = \lambda_{BG}$ (i.e. zero detuning between Bragg grating and longitudinal mode), the continuous tuning slope yields:

$$s_{T,cont} = \frac{\mu_a}{\tilde{\mu}_{BG}} \frac{L_a}{L_{PS}} + \frac{\mu_p}{\tilde{\mu}_{BG}} \frac{L_{WG}}{L_{PS}} + \frac{\mu_p}{\tilde{\mu}_{BG}}. \quad (4.8)$$

Two important conclusions can be extracted from eq. (4.8). Firstly, the slope is independent of the length of the Bragg grating. Hence, if the tunable DBR is intended to be optimized for continuous tuning, the length of the Bragg grating can be chosen freely in order to ensure adequate filtering of the longitudinal modes and hence single-mode operation. Secondly, given a certain phase shift and wave guiding sections with refractive index μ_p , a passive propagation section with refractive index μ_p , and a reflector with a refractive index $\tilde{\mu}_{BG}$, the physical lengths L_{PS} , L_{WG} , and L_a , can be optimized from eq. (4.8) in order to yield an $s_{T,cont}$ as close as possible to 1, and hence to provide the largest continuous tuning possible.

For the specific case of the III-V/polymer tunable DBR, due to the low refractive index of polymers and the low refractive index contrast of the waveguides, the effective refractive index in the Bragg grating can be approximated by the effective refractive index in the polymer waveguide, i.e. $\tilde{\mu}_{BG} \approx \mu_p = 1.456$. Applying this approximation in eq. (4.8), the following expression for the continuous tuning slope results:

$$s_{T,cont} \approx \frac{\mu_a}{\tilde{\mu}_{BG}} \frac{L_a}{L_{PS}} + \frac{L_{WG}}{L_{PS}} + 1. \quad (4.9)$$

From this equation, it can be seen that, in the case of low refractive index contrasts of the passive section such as is the case of the polymer waveguides used in this work, $s_{T,cont}$ will always be larger than one, and will trend asymptotically to one when increasing L_{PS} and decreasing the length of the active section L_a . This implies that, for a certain temperature change in the Bragg grating $\Delta T'_{BG}$, and considering the definition of the continuous tuning slope $s_{T,cont}$, the temperature change in the phase section needed to ensure continuous tuning will be provided by $\Delta T'_{PS} = s_{T,cont} \Delta T'_{BG}$, and the required $\Delta T'_{PS}$ will always be larger

than $\Delta T'_{BG}$. This is equivalent to say that the tuning efficiency of the longitudinal modes will always be lower than that of the Bragg grating. Considering eq. (4.3) for $\Delta\lambda_m$, the maximum continuous tuning $\Delta\lambda_{cont}$ achievable with a certain continuous tuning slope $s_{T,cont}$ can be provided by the following expression:

$$\Delta\lambda_{cont} = \frac{2}{m} \left[TOC \cdot L_{PS} T'_{max} + TOC \cdot L_{BG,eff} \frac{T'_{max}}{s_T} \right]. \quad (4.10)$$

From eqs. (4.8) and (4.10), the continuous tuning slope and the maximum achievable continuous tuning range considering a maximum temperature increase T'_{max} can be analytically calculated. In Figure 4.10 (a), the calculated continuous tuning slope $s_{T,cont}$ for different values of the phase section length L_{PS} considering a tunable laser with design parameters $L_a=400 \mu\text{m}$, $\mu_a=3.8$, $L_{WG}=300 \mu\text{m}$, $\mu_{BG} \approx \mu_p = 1.456$. Confirming the previous discussions, the continuous tuning slope decreases with increasing the length of the phase section, and asymptotically tends to 1. As it has been mathematically discussed previously, for a given maximum tolerated temperature increase in the polymer material T'_{max} , the maximum continuous tuning is achieved when the continuous tuning slope $s_{T,cont}$ has a value as close as possible to 1. In Figure 4.10 (b), the maximum continuous tuning considering a maximum tolerated temperature increase in the polymer of $T'_{max}=175 \text{ }^\circ\text{C}$ is shown as a function of the length of the phase section. As expected from the previous discussions, the maximum continuous tuning increases with the length of the phase section, and tends asymptotically to the tuning achievable by the Bragg grating at the maximum tolerated temperature increase. Hence, a continuous tuning range $\Delta\lambda_{cont}$ over more than 17 nm is expected by means of using phase sections with a length of around 6.5 mm and beyond. Nevertheless, it should be noted that increasing length of the phase section implies that the wavelength spacing between the longitudinal modes and the separation between mode-hop boundaries will be reduced, hence making more stringent the bandwidth characteristics of the Bragg grating bandwidth in order to ensure single mode operation.

On a practical note, it is worth mentioning that, for the driving of the tunable laser, a slope that relates the applied electrical powers in the phase section and the Bragg grating section is of more convenience. The electrical power in a micro heater is directly proportional to the temperature increase achieved times the length L of the electrode, i.e. $P \propto \Delta T \cdot L$. Hence, an electrical power slope, noted as $s_{P,cont}$, can be expressed as a function of the temperature slope provided by eq. (4.9) as

$$\begin{aligned} s_{P,cont} &= s_{T,cont} \left(\frac{L_{PS}}{L_{BG}} \right) \approx \left(\frac{L_{PS}}{L_{BG}} \right) \left(\frac{\mu_a}{\tilde{\mu}_{BG}} \frac{L_a}{L_{PS}} + \frac{\mu_p}{\tilde{\mu}_{BG}} \frac{L_{WG}}{L_{PS}} + 1 \right) \\ &= \frac{\mu_a}{\tilde{\mu}_{BG}} \frac{L_a}{L_{BG}} + \frac{\mu_p}{\tilde{\mu}_{BG}} \frac{L_{WG}}{L_{BG}} + \frac{L_{PS}}{L_{BG}}. \end{aligned} \quad (4.11)$$

4.3.2 Experimental results

Tuning experiments were been performed III-V/polymer DBR laser with a $L_a=400 \mu\text{m}$, $L_{PS}=4 \text{ mm}$, $L_{WG}=300 \mu\text{m}$, and $L_{BG}=1.5 \text{ mm}$, and a Bragg grating designed at $\lambda_{BG}=1568 \text{ nm}$ ($\Lambda=1.617 \mu\text{m}$ considering $\tilde{\mu}_{BG} \approx \mu_p=1.456$). Considering the calculated maximum continuous tuning ranges shown in Figure 4.10 (b), a continuous tuning range of around 16 nm is expected. From eq. (4.11), and considering $\mu_a=3.6$ and $\tilde{\mu}_{BG} \approx \mu_p=1.456$, the slope can be calculated to be $s_{P,cont}=3.6$. However, a heater power slope $s_{P,cont}$ for continuous tuning was empirically extracted from measured 2-D wavelength maps, and set to 3. The reasons of the deviation between calculated and extracted results could be attributed to fabrication

4. Design Strategies and Performance of III-V/Polymer Tunable DBR Lasers

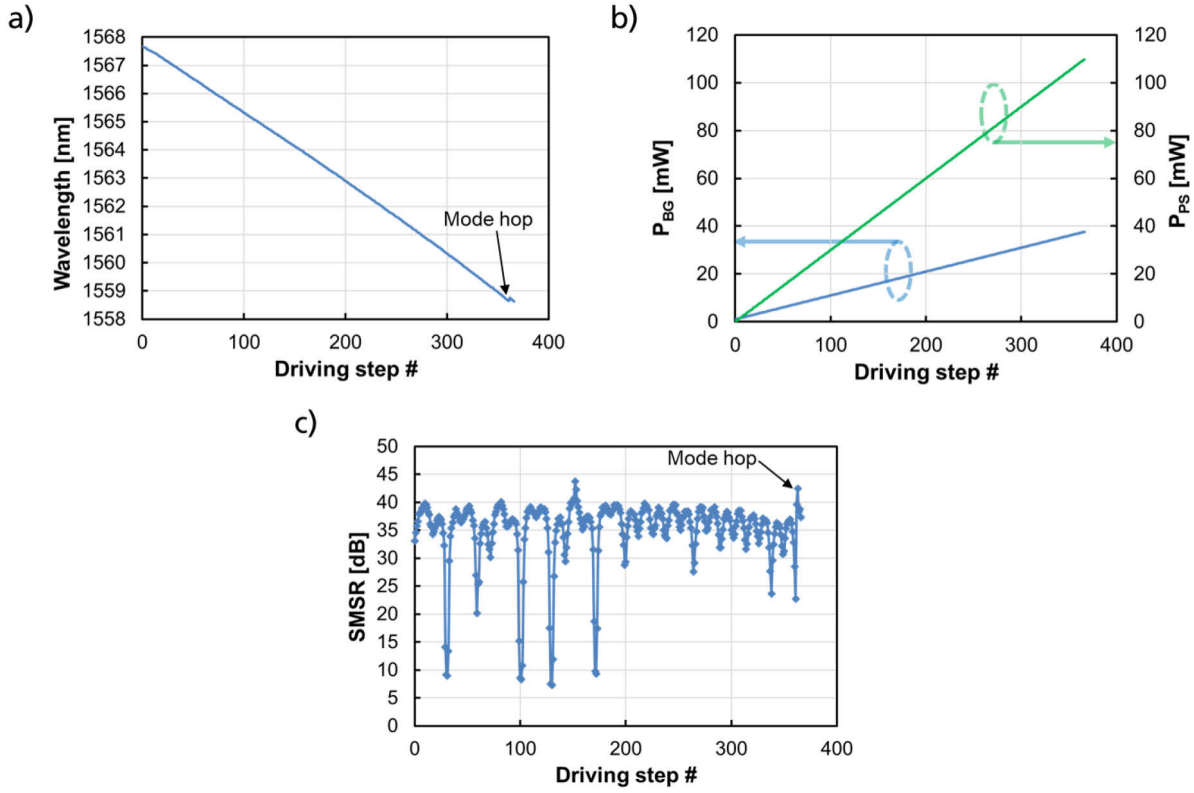


Figure 4.11. (a) Measured continuous wavelength tuning on a DBR laser with a 4mm-long phase section. (b) Electrical power applied at the Bragg grating and phase section for each driving step. (c) Side-mode suppression ratio (SMSR) at each driving step. The wavelength and SMSR values were extracted using an optical spectrum analyzer with a set resolution of 0.05 nm.

deviations and/or non-homogeneous temperature distributions along the micro-heaters, which could imply that the effective refractive indices and lengths of the different sections involved in eq. (4.11) would differ from the design values. An optical spectrum Analyzer (OSA) with a maximum resolution of 0.05 nm was used for the determination of the lasing wavelength. In Figure 4.11 (a), the wavelength measured at different steps along the tuning trajectory is plotted, while Figure 4.11 (b) shows the set electrical powers on the Bragg grating and phase section at each step using a slope $s_{P,cont}=3$. After a continuous tuning of 9 nm, a mode hop occurred.

To evaluate the reason of the mode-hop, it is worth looking at the measured SMSR at each wavelength step, shown in Figure 4.11 (c). As it can be seen, the SMSR varies along the mode-hop-free tuning in an oscillatory way. This is unexpected from ideal 2-D wavelength maps, since as it has been previously shown, the mode-hop boundaries follow a linear behavior, and any trajectory parallel to them should maintain the same detuning and hence the same SMSR. A possible explanation to this effect could be optical feedback from the fiber-to chip interface, which creates a phase and hence wavelength-dependent variation of the position of the longitudinal modes and the mode-hop-free boundaries. The expected mode-hop-free tuning value of 16 nm is therefore yet to be proven.

As a final remark, notice that the design strategy in order to achieve a large continuous tuning range by means of increasing the length of the phase section L_{PS} is compatible with the design strategy for narrow linewidth discussed in Section 4.2, since long effective lengths of the passive sections will be achieved.

However, the long phase sections are incompatible with the design strategy for high-speed modulation discussed in Section 4.1.

4.4 Conclusions of the chapter

In this chapter, different design strategies of the polymer-based passive section have been discussed in order to optimize the high-speed direct modulation characteristics, the linewidth, or the continuous tunability.

Since the relaxation oscillation frequency decreases and the transient linewidth enhancement factor increases when including an external cavity into a semiconductor laser, keeping short polymer passive sections (i.e. low values of A) is the adequate strategy to enable high-speed direct modulation. With a device comprising an effective polymer passive section of 850 μm and a Bragg grating with a reflectivity of 20%, output powers ex-fiber of more than 6.5 mW (8.1 dBm), a tuning range in excess of 20 nm and SMSR values close to 50 dB have been achieved. Relaxation oscillation frequencies of more than 8 GHz and transient linewidth enhancement factors close to 1.5 have been achieved when inducing in the laser a certain detuning to increase the value of the parameter B . These values, together with measured peak RIN values lower than -136 dB/Hz, show the potential of the presented tunable laser implementation for 10 Gb/s direct modulation. A further increase of the relaxation oscillation frequency and decrease of the transient linewidth enhancement factor might be achieved increasing the parameter B by e.g. reducing the length of the active and passive sections, which would increase the mode spacing between longitudinal modes and potentially enable a larger detuning before a mode-hop occurs.

The linewidth of the laser is reduced when increasing the length of the passive section (i.e. parameter A) and increasing the detuning (i.e. B) by a factor $F^2 = (1 + A + B)^2$. For a DBR laser including a polymer section with an effective length of 1525 μm and a Bragg grating with a reflectivity of 20%, linewidths as low as 130 kHz have been achieved. The device showed an output powers ex-fiber of more than 7 mW (8.45 dBm), a tuning range of more than 20 nm, and SMSR values up to 50 dB. Increasing the length of the active section and increasing reflectivity of the Bragg grating, theoretical calculations shown that linewidths lower than 10 kHz might be achievable.

Continuous tuning can be achieved by means of tuning simultaneously the Bragg grating and the longitudinal modes of the phase shifter. Since, in the proposed device, the tuning efficiency of the phase shifter is lower than that of the Bragg grating, the achievable mode-hop-free tuning range can be extended by means of increasing the length of the phase shifter. With a phase shifter length of 4 mm, a mode-hop-free tuning of around 9 nm has been achieved, after which a mode-hop occurred. Theoretical results shown that, with that very same phase shifter length and for a maximum temperature increase in the polymer waveguide of 175°C, a mode-hop-free tuning range of 16 nm is potentially achievable with optimized driving of the phase and Bragg grating sections.

5. Wavelength Setting, Stabilization, and Device Reliability

Besides the key performance characteristics discussed in the previous chapter, the setting of the tunable laser at a desired wavelength and its stabilization, as well as the reliability of the device over time, are key practical aspects to be addressed to study the usability of tunable lasers in real application scenarios. These aspects are of special importance in thermo-optically tunable structures, firstly due to the dependence of the lasing wavelength on the temperature, and secondly due to the required high local temperatures to achieve a large tuning range. The latter aspect has also a direct influence on the long-term reliability of the device, since high temperatures may induce irreversible damage in the tunable sections.

This chapter covers the wavelength setting and stabilization of a III-V/polymer DBR laser. The methodology was developed within the master thesis written by Magnus Happach [63], which I supervised. The results were published in [64]. My contributions to this work were the design and hybrid integration of the DBR laser device, and the development of the wavelength stabilization methodology. The stabilization method relies on the use of the voltage drop in the active section as a monitoring signal to detect the detuning between the Bragg grating and the longitudinal modes. This signal can be used not only as a monitor of the lasing wavelength and the operation conditions of the device, but also as a monitoring of mode-hops, which can allow for a quick experimental extraction of the continuous tuning slope $s_{p,cont}$ (provided by eq. (4.11)) during initialization of the device. As it will be discussed, this continuous tuning slope can be of much practical convenience for setting the laser from an initial operation point towards the desired wavelength. Additionally, to throw some final light with regards to the practical usability of the device, some initial studies with regards to long-term reliability are presented.

5.1 Effect of temperature variations on the lasing wavelength

In order to study the influence of the environmental temperature on the III-V/polymer DBR laser, let us first develop mathematically the dependence of the Bragg grating wavelength and the wavelength of the longitudinal modes of a certain variation in the operation temperature of the device T'_{env} . From eqs. (3.6) and (3.18), the following expressions can be obtained:

$$\lambda_{BG} = \frac{2}{m_{BG}} (\tilde{\mu}_{BG} + T'_{env} \cdot TOC_p) \Lambda \quad (5.1)$$

$$\begin{aligned} \lambda_m = \frac{2}{m} [& (\mu_a + T'_{env} \cdot TOC_a) L_a + (\mu_p + T'_{env} \cdot TOC_p) L_{WG} + (\mu_p + T'_{env} \cdot TOC_p) L_{PS} + \\ & + (\tilde{\mu}_{BG} + T'_{env} \cdot TOC_p) L_{BG,eff}], \end{aligned} \quad (5.2)$$

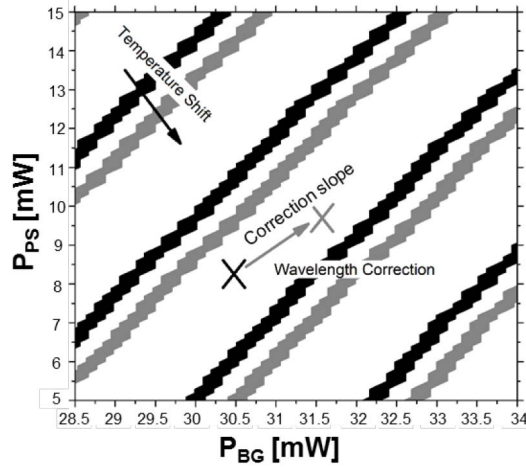


Figure 5.1. Wavelength maps at two different temperatures of the III-V/polymer tunable DBR as a function of the electrical powers at the tunable phase section (P_{PS}) and Bragg grating (P_{BG}). To correct a temperature induced wavelength shift by means of re-adjusting the heater powers at the phase and Bragg section, a certain correction slope must be applied. The figure has been extracted from [64].

being TOC_a and TOC_p the thermo-optical coefficients of InP and polymer, respectively. It should be noted that, in those equations and in the discussions henceforth, the effect of the thermal expansion coefficient (CTE) has not been included. This can be argued parting for the layer arrangement of the polymer-based device (see Section 3.4), which comprises a thick Si substrate on top of which the different polymer lasers are coated and structured to form the waveguide cross section. Although the CTE of the polymer material is fairly high ($200\text{--}300 \times 10^{-6} \text{ K}^{-1}$ [29]), the CTE of silicon is two orders of magnitude lower ($2.5 \times 10^{-6} \text{ K}^{-1}$ [65]). For this reason, it seems reasonable to consider in a first approximation that the low CTE of the Si will dominate, and will limit the expansion and contraction of the polymer material.

The temperature variation on the device induces a wavelength shift of the lasing mode and of the Bragg grating. In the more general case, this induces a detuning. In order to portray graphically the effect that this change has in the operation point of the device, let us consider the 2-D wavelength map as a function of the electrical powers in the Bragg grating (P_{BG}) and in the phase heaters shown in Figure 5.1. The black and grey lines indicate the mode-hop boundaries for two temperatures T_1 , and $T_2 = T_1 + T'_{env}$, respectively, where $T_1 = 25^\circ\text{C}$ and $T_2 = 45^\circ\text{C}$ (i.e. T'_{env} is an increase in the temperature). As it can be seen, the variation in the temperature of the device changes not only the lasing wavelength and the detuning, as expected considering eqs. (5.1) and (5.2), but also the position of the mode-hop boundaries. In order to force the laser to stay at its initial wavelength, a correction in the operation point of the Bragg and phase sections needs to be applied. Similarly as it was done for the continuous tuning in Section 4.3, the required variations in the electrical power in the Bragg grating and phase section required to correct the wavelength, noted from now on, respectively, as ΔP_{PS} and ΔP_{BG} , can be expressed by means of certain a correction slope, which can be defined as $s_{p,corr} = \Delta P_{PS} / \Delta P_{BG}$. It is worth noting here that that the aging of the device can also result in variations of the wavelength map. Hence, having a correction mechanism that can overcome variations in the temperature will also provide a way of overcoming drifts due to aging.

5.2 Wavelength correction under temperature variations

In order to develop a mathematical expression for the correction slope, let us calculate the variations in the Bragg and longitudinal mode wavelengths as a function of the change in the environmental temperature T'_{env} . From eqs. (5.1) and (5.2), those variations can be easily extracted to be:

$$\Delta\lambda_{BG} = \frac{2}{m_{BG}} (T'_{env} \cdot TOC) \Lambda \quad (5.3)$$

$$\begin{aligned} \Delta\lambda_m = \frac{2}{m} [(T'_{env} \cdot TOC_a) L_a + (T'_{env} \cdot TOC_p) L_{WG} + (T'_{env} \cdot TOC_p) L_{PS} + \\ + (T'_{env} \cdot TOC_p) L_{BG,eff}] . \end{aligned} \quad (5.4)$$

If the initial operating wavelength of the device is to be maintained, the Bragg and phase sections in the laser cavity can be accordingly driven so that the induced local temperature changes T'_{PS} and T'_{BG} compensate the effect of T'_{env} . Including in eqs. (5.3) and (5.4) these local temperature variations, the following equations result:

$$\Delta\lambda_{BG} = \frac{2}{m_{BG}} (T'_{env} + T'_{BG}) \cdot TOC_p \cdot \Lambda \quad (5.5)$$

$$\begin{aligned} \Delta\lambda_m = \frac{2}{m_l} [(T'_{env} \cdot TOC_a) L_a + (T'_{env} \cdot TOC_p) L_{WG} + (T'_{env} + T'_{PS}) \cdot TOC_p \cdot L_{PS} + \\ + (T'_{env} + T'_{BG}) \cdot TOC_p \cdot L_{BG,eff}] . \end{aligned} \quad (5.6)$$

From eq. (5.5), it is straightforward to see that, in order to keep the Bragg wavelength at its initial conditions (i.e. $\Delta\lambda_{BG} = 0$), the induced T'_{BG} should have the same magnitude and opposed sign as T'_{env} , i.e.

$$T'_{BG} = -T'_{env} . \quad (5.7)$$

This T'_{BG} can be included in the wavelength shift equation of the longitudinal mode given by eq. (5.6), from which an expression of the required T'_{PS} needed to keep the original longitudinal mode position (i.e. $\Delta\lambda_m = 0$) can be obtained

$$T'_{PS} = T'_{env} \frac{L_a TOC_a + L_{WG} TOC_p + L_{PS} TOC_p}{L_{PS} TOC_p} . \quad (5.8)$$

From eqs. (5.7) and (5.8), a correction slope for the driving temperatures in the phase and Bragg grating, namely $s_{T,corr}$, which will allow re-setting the Bragg grating and the longitudinal mode to its initial lasing conditions, can be defined as

$$s_{T,corr} = \frac{T'_{PS}}{T'_{BG}} = \frac{L_a TOC_a + L_{WG} TOC_p + L_{PS} TOC_p}{L_{PS} TOC_p} . \quad (5.9)$$

To adapt the temperature slope provided by eq. (5.9) to a slope that relates the applied electrical powers, let us take into account that the electrical power in a micro heater is directly proportional to the induced

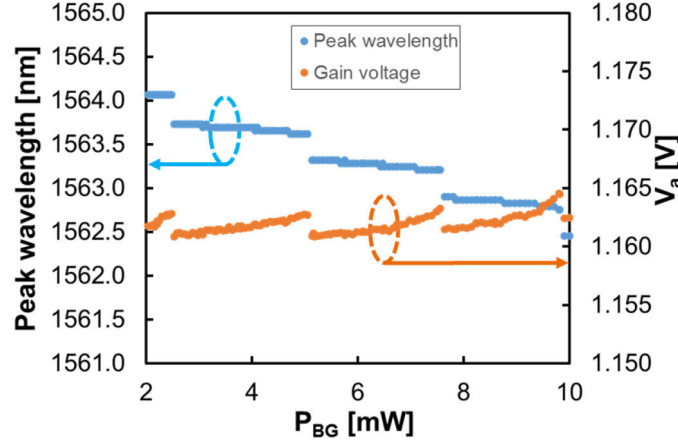


Figure 5.2. Measured lasing wavelength and voltage drop measured at the active section (V_a) for a scan of the electrical power applied on the Bragg grating micro-heater (P_{BG}). The temperature of the device was set to 45°C. The figure has been extracted from [64].

temperature increase times the length L of the electrode, i.e. $P \propto \Delta T \cdot L$ [62]. Hence, an electrical power slope $s_{P,corr}$ can be expressed as a function of the temperature slope as

$$s_{P,corr} = s_{T,corr} \left(\frac{L_{PS}}{L_{BG}} \right) = \frac{L_{PS}}{L_{BG}} \left(\frac{L_a TOC_a + L_{WG} TOC_p + L_{PS} TOC_p}{L_{PS} TOC_p} \right). \quad (5.10)$$

5.3 The voltage drop in the active section as a monitoring signal

Having seen that a correction slope to overcome changes in the operation point due to environmental conditions can be mathematically obtained, the next step is to obtain some read-out signals that can be monitored in order to track when variations in the operation point occur. One possible read-out signal that can be used is the voltage drop at the active section. Biasing the tunable laser above threshold, there exists a direct correlation between voltage drop at the active section and the detuning [45]. This is due to the fact that, by means of modifying the detuning conditions, the threshold conditions of the lasing mode vary due to the wavelength dependence of the cavity losses, which are attributed to the wavelength dependence of both the Bragg grating reflectivity and the losses in the active section. Due to the pinning of the threshold gain g_{th} and the carrier density in the active section n_{th} , and provided that the injected current in the active section I_a is kept constant, the detuning will result in a variation of n_{th} , and hence in a variation in the voltage of the active section V_a . If the losses at the new lasing mode are different from the losses that the previous lasing mode experienced before the mode-hop, a discontinuity in the voltage drop will be observed. This effect is shown in Figure 5.2, where the measured wavelength and voltage at the active section while tuning only the Bragg grating (i.e. modifying the detuning conditions) are plotted. As it can be seen, the mode-hops are correlated with discontinuities in the voltage, which proves that the voltage in the active section can provide information on the detuning, and on the occurrence of mode-hops.

The possibility of detecting the occurrence of mode-hops by means of monitoring the active section can be used for the experimental extraction of the continuous tuning slope, $s_{P,cont}$, which has been introduced in Section 4.3 and can be calculated using eq. (4.11). The continuous tuning slope can be useful not only

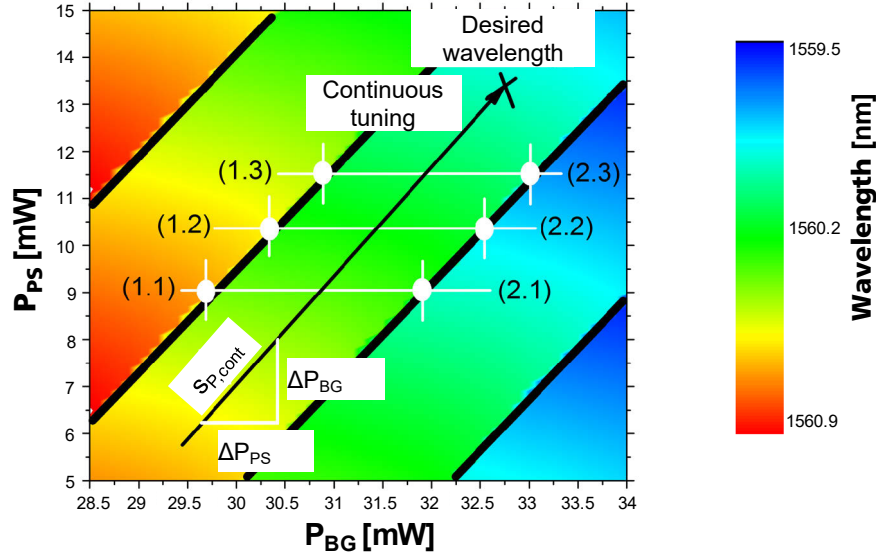


Figure 5.3. Measured wavelength mapping of a III-V/polymer DBR tunable with mode hop boundaries marked in black. The horizontal white lines mark sweeps of the Bragg power P_{BG} performed at different phase currents P_{PS} in order to detect different mode-hop operation points by means of monitoring the voltage drop at the active section. Interpolating the points along one mode-hop boundary at which mode-hops occur, the mode-hop free tuning slope can be extracted experimentally without the need of performing multi-dimensional wavelength maps. The figure has been extracted from [64].

for operating the laser in a wavelength-sweep modus, but also to set the laser at the desired wavelength starting from an initial operation point. In order to see how s_P could be extracted from V_a , let us consider the measured wavelength map shown in Figure 5.3. The mode-hop boundaries are marked as solid black lines. Tuning the Bragg grating for three different electrical power values applied on the phase shifter P_{PS} allows running into the mode-hops marked as 1.1–1.3 and 2.1–2.3. The occurrence of those mode hops can be detected measuring V_a . Knowing the values of P_{BG} and P_{PS} at which those mode hops occur, and by means of linear interpolation either of the set 1.1–1.3 or 2.1–2.3, $s_{P,cont}$ can be obtained. This method for obtaining $s_{P,cont}$ uses only direct electrical measurements at the gain section, and can be potentially executed during initialization of the laser in real systems and repeated after a certain operation time for recalibration, hence addressing possible changes in the device due to aging.

5.4 Method for wavelength setting and stabilization

In this section, a procedure for setting and stabilizing the operation wavelength is proposed based on the correction slope $s_{P,corr}$ given by eq. (5.10), and the use of the voltage drop in the active section for monitoring of detuning conditions and for the extraction of the continuous tuning slope $s_{P,cont}$.

Step 1: setting of a preliminary operation point

When targeting a certain wavelength, a preliminary lookup table (LUT), which can be extracted with minimal characterization effort performing a 1D scan of the electrical power on the Bragg grating for a certain electrical power on the phase section, can be used to find a preliminary operation point (i.e. a combination of P_{BG} and P_{PS}) close enough to the target wavelength. The extraction of this preliminary LUT can be done with a low time-effort when compared to the accurate multi-dimensional maps, and can be

5. Wavelength Setting, Stabilization, and Device Reliability

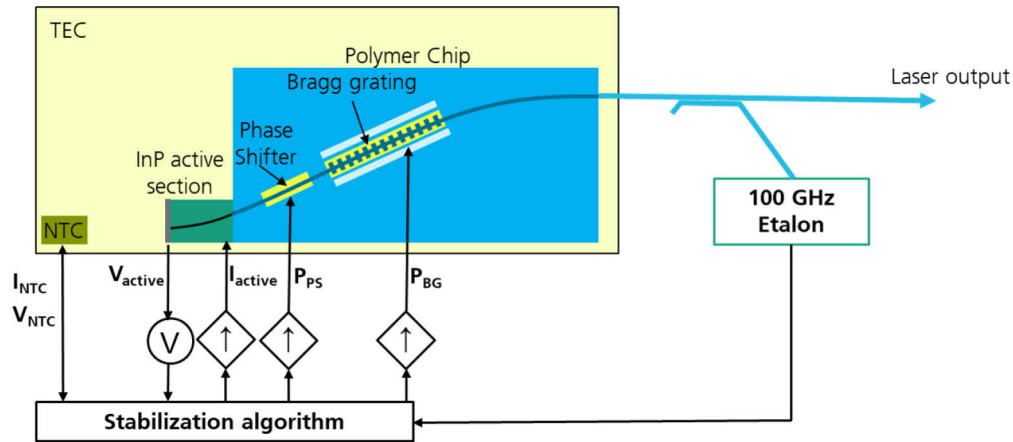


Figure 5.4. Schematic of the wavelength stabilization circuit. The software-based control unit reads out the active section voltage drop, and adjusts the electrical power on the phase shifter and Bragg grating sections. A commercially available 100-GHz etalon was used in order to monitor variations in the wavelength.

performed before installing the tunable laser in the relevant application environment, serving as a calibration data.

Step 2: extraction of the continuous tuning slope $s_{P,cont}$

Following the methodology described in Section 5.3, it is possible to extract experimentally the continuous tuning slope $s_{P,cont}$ by means of using the voltage drop at the active section, and without the need of any further wavelength-measuring equipment. This routine could be repeated after a certain operation time of the laser, as a means of a self-calibration.

Step 3: adjustment of detuning

As it has been discussed in Section 2.5 and experimentally observed in Subsections 4.1 and 4.2, the detuning can have positive influence in different dynamic characteristics of the device. However, it should be taken into account that inducing a detuning sets the operation point of the laser close to the occurrence of a mode-hop, which makes the laser more susceptible to suffer mode-hops due to changes in the temperature, drifts in the current sources, or aging of the device. For the experiments performed here, an operation point of minimum detuning was targeted. This detuning can be determined by means of using the voltage drop in the active section as a monitoring signal, as discussed in 5.3. The execution has been proven to take only a few seconds, and can be performed during initialization of the laser and be repeated after a certain operation time of the laser, serving as self-calibration.

Step 4: setting of the desired wavelength by means of continuous tuning

Starting from the initial operation point with the desired detuning, the laser can be tuned continuously to the targeted wavelength using the tuning slope $s_{P,cont}$ extracted in step 2. A wavelength monitor (implemented by means of e.g. a Fabry-Pérot resonator) can be used as a monitoring signal to determine when the desired operation wavelength has been reached.

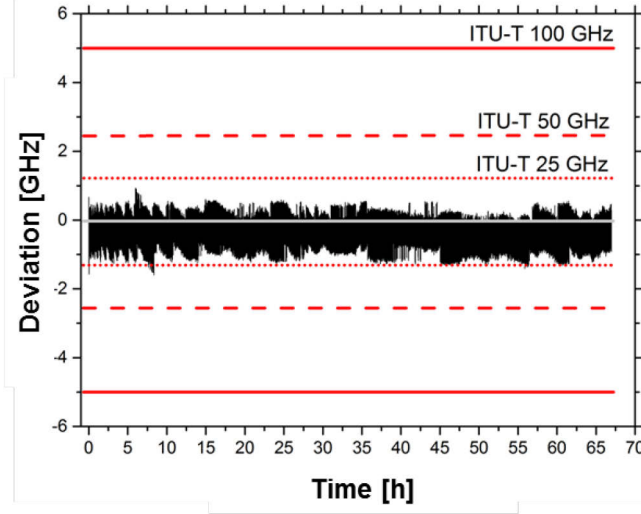


Figure 5.5. Frequency deviation of a stabilized III-V/polymer DBR laser operated at 45 °C. The red lines mark a deviation of $\pm 5\%$ of the channel spacing for the ITU-T frequency grid standards with 100, 50 and 25 GHz channel spacing. The figure has been extracted from [64].

Step 5: wavelength stabilization

In order to stabilize the laser wavelength against drifts caused by environmental changes, the correction slope $s_{P,corr}$, given by eq. (5.10), can be used. If a monitoring signal (such as the voltage drop at the active section, and/or a photodiode from a wavelength monitor) indicates a wavelength drift, the laser is tuned using the driving slope $s_{P,corr}$ until the desired wavelength is reached. Notice that, as discussed in Section 5.2, tuning with the slope $s_{P,corr}$ will allow maintaining the detuning conditions initially set in step 3.

5.5 Experiments on wavelength stabilization

The described procedure for wavelength stabilization was tested using a stabilization feedback loop as described in Figure 5.4. The used DBR tunable laser featured the same geometry parameters as the narrow linewidth device considered in Section 4.2 ($L_a = 400 \mu\text{m}$, $L_{WG} = 300 \mu\text{m}$, $L_{PS} = 600 \mu\text{m}$, and $L_{BG} = 1250 \mu\text{m}$). The DBR tunable laser device was placed on a thermoelectric cooler (TEC), and a miniaturized negative temperature coefficient (NTC) thermistor was used to monitor the operation temperature. The output of the tunable laser was connected to a 100-GHz etalon as a wavelength monitor, whose output was fed to a software-based control unit in order to detect variations in the wavelength. The control unit regulated the current/voltage sources which set the injection current in the active section (I_a), and the electrical powers in the phase section (P_{PS}) and the Bragg grating (P_{BG}). The voltage at the active section (V_a) was also monitored in order to detect variations in the detuning. A wavelength meter was used after the laser output in order to evaluate the performance of the stabilization loop. As a metric for the evaluation of the stabilization performance, a maximum tolerable lasing frequency deviation from the ITU-T DWDM frequency grid standard [66] of $\pm 5\%$ has been considered.

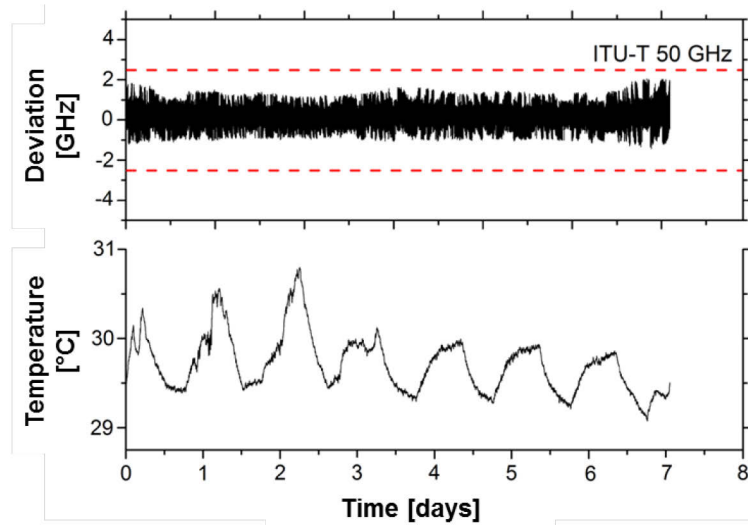


Figure 5.6. Frequency deviation of an uncooled III-V/polymer DBR laser in laboratory conditions, and $\pm 5\%$ channel deviation of the ITU-T frequency grid standard with 50 GHz channel spacing. The figure has been extracted from [64].

5.5.1 Stabilization at a constant device temperature

Initial stabilization tests were performed operating the tunable laser at a fixed temperature of 45°C . Figure 5.5 shows the frequency deviation for a time interval of more than 65 hours, after which the test was stopped. A temperature wavelength deviation below ± 1.25 GHz was achieved over the measured time. Considering a tolerable wavelength deviation of $\pm 5\%$ of the channel spacing (the error margins for 25, 50 and 100 GHz ITU-T frequency grids are included in Figure 5.5), it can be concluded that the tunable laser could be operated in grids with a channels spacing as low as 25 GHz.

5.5.2 Uncooled stabilization in a laboratory environment

In order to evaluate the performance of the stabilization method of the tunable laser in an uncooled regime, tests were performed in a laboratory environment deactivating the TEC, and monitoring the temperature using the NTC thermistor placed close to the device. Figure 5.6 shows the wavelength deviation over more than 7 days, after which the experiment was stopped. It can be seen that, during this time span, a wavelength deviation under 2 GHz for temperature variations of around 1.5°C could be achieved. These results show that the tunable laser could remain stable in the ITU-T 50 GHz without the need of temperature stabilization.

5.5.3 Stabilization under forced temperature variations

To study the performance of the stabilization method under large temperature variations, the temperature of the TEC was changed from 15° to 60°C at a rate of 0.1°C/s . Besides the monitoring signals from the 100-GHz etalon and the active section (V_a), the signal of the NTC served also to monitor the temperature changes, and the information was used by the control unit to correct the wavelength and stabilize the laser using the correction slope $S_{P,corr}$. It should be noted that, without the stabilization of the tunable laser, temperature variations of $T'_{env}=45^{\circ}\text{C}$ would imply a wavelength shift of around 4.5 nm, as it can be extracted from eq. (5.3). Figure 5.7 shows the stabilization at four 50-GHz ITU-T channels during more than 10 hours with 40 temperature sweeps, where it can be observed that all four channels could be

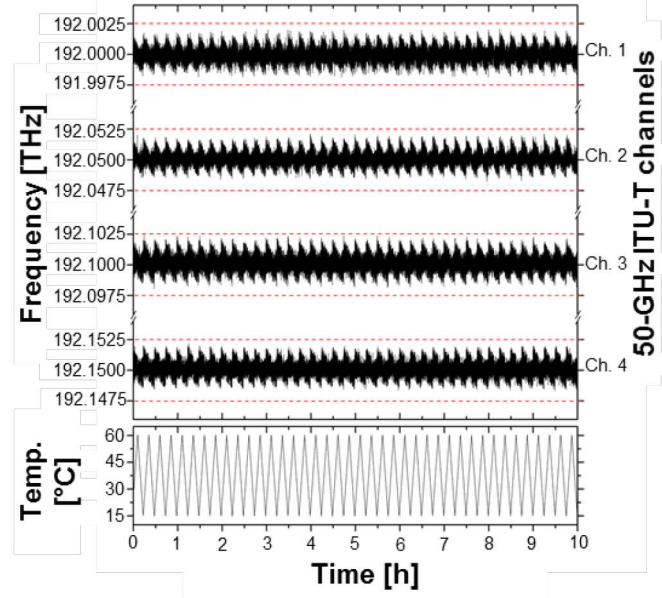


Figure 5.7. Stabilization of the III-V/polymer DBR laser at four channels of the ITU-T Grid with 50 GHz spacing under forced temperature changes between 15 °C and 60 °C. The red-dashed lines showed the maximum tolerated frequency deviation of $\pm 5\%$ of the channel spacing in 50 GHz ITU-T grid. The figure has been extracted from [64].

stabilized within 5 GHz ($\pm 5\%$ of the 50 GHz channel spacing). The achieved results show the possibility of stabilizing the III-V/polymer DBR laser under harsh temperature variations, hinting towards the applicability of the III-V/polymer tunable laser and the proposed stabilization method in real application scenarios.

5.6 Initial studies on long-term reliability

After addressing the wavelength setting and wavelength stabilization over time, a last point still remains open in order to study whether the proposed implementation can be of relevance in real application environments: the long term reliability of the device. As it can be derived from eq. (3.28) considering a third order grating designed at the wavelength of 1570 nm ($\Lambda = 1.617 \mu\text{m}$ with $\tilde{\mu}_{BG} = 1.456$) and the characteristics of the polymer waveguide summarized in Table 3.1, a 20 nm tuning range requires a temperate change in the Bragg grating of around 169°C. This indicates that the local temperature of the Bragg grating is around 194 °C when driving the device at room temperature (25°C). Although the degradation temperature of the ZPU-12 polymer material used in this work is 300°C [29], the baking temperatures of the polymer material during fabrication reach 200°C (see Subsection 3.4.1), and temperatures around this value and above might induce irreversible changes in both optical and structural properties of the material. Additionally, to be readily deployed in the corresponding application environments, the laser needs to be packaged in a certain housing, meaning that various glues for optical, mechanical fixation, as well as metal wire bonds between the contact pads in the device and the housing pins, have to be included. All these parts must prove to be stable in a collective manner during the long-term operation.

5. Wavelength Setting, Stabilization, and Device Reliability

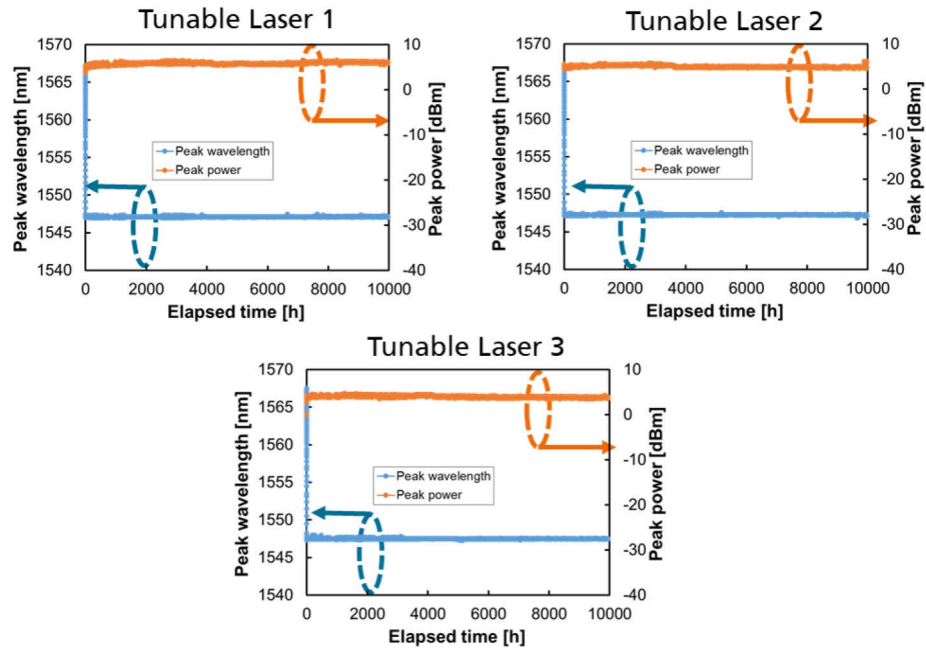


Figure 5.8. Measured wavelength and peak output power of three DBR tunable laser modules operating at 20-nm tuned wavelength at a stabilized temperature of 25°C.

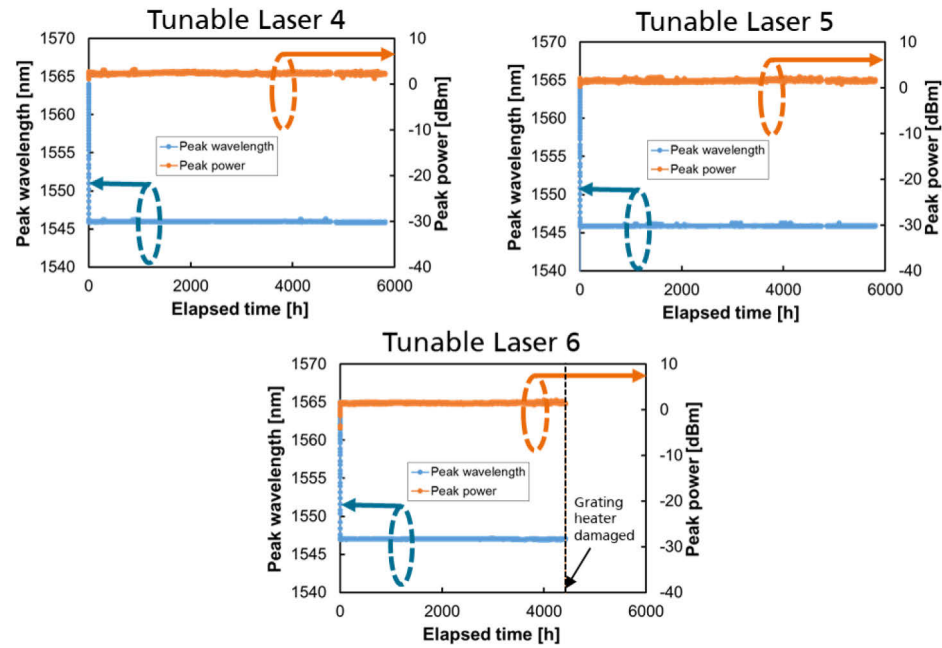


Figure 5.9. Measured wavelength and peak output power of three tunable laser modules operating at 18-nm tuned wavelength at a stabilized temperature of 45°C.

In order to extract some preliminary conclusions on the long-term reliability tests of the proposed III-V/polymer tunable lasers, a batch of three tunable laser devices with nearly identical parameters were packaged in 14-pin butterfly modules. The temperature of the tunable laser was stabilized to 25°C by means of a TEC, the lasing wavelength was tuned 20 nm with respect to the initial lasing wavelength, implying a

maximum temperature in the polymer of 194 °C, and the SMSR was adjusted to > 40 dB. The laser outputs were fed into optical power meters in order to record the output power. Additionally, part of the output was coupled to an optical spectrum analyzer (OSA) for the monitoring of the lasing wavelength. A basic wavelength stabilization method was implemented, which used as feedback the values measured at the optical power meter and OSA in order to maintain the output power and the lasing wavelength by means of re-adjusting the injected currents in the active and thermo-optically tunable sections. In these initial investigations, the modules were not hermetically sealed.

The tests ran for over 10,000 hours, which exceeds one year, and all three modules exhibited almost identical behavior, as it is shown in Figure 5.8. Both the output power and the central wavelength appear constant over the entire test span without any indication of abrupt breakdown or slow-declining of device performance.

A second batch of three laser modules was prepared and the tests were performed in a similar way, but this time at an operation temperature of 45°C. In order to keep a similar maximum temperature on the polymer waveguide below 200°C, the induced tuning was 18 nm, which from eq. (3.28), the temperature change in the Bragg grating can be calculated to be 152°C. Considering the operation temperature of 45°C, the maximum temperature in the polymer reaches 197°C. In Figure 5.9, the lasing wavelength and output power of the three tunable laser modules is shown. Although two devices showed no degradation after more than 5800 h, after which the testing was stopped, one device showed a breakdown of the Bragg grating heater after 4420 h. These results seem to show that the reliability of such devices might be compromised if the temperature in the polymer approaches 200°C, although to confirm this, further statistical measurements would be necessary.

Rigorous accelerated life tests should be conducted in a next stage according to the Telcordia Generic Requirement in order to estimate the general life span of the product in a statistic manner [67]. Nevertheless, the preliminary reliability tests in this work show a promising reliability of the III-V/polymer tunable laser is promising when the maximum temperature on the polymer waveguide is lower than 200°C, i.e. 20 nm maximum tuning at 25°C, or 18 nm tuning at 45°C.

5.7 Conclusions of the chapter

In this chapter, a methodology for wavelength setting and stabilization has been proposed. This concept relies on a preliminary LUT based on a simple one-dimensional scan and the use of the voltage drop at the active section as a monitoring signal, and does not require accurate and time-consuming multi-dimensional wavelength maps. The voltage drop provides information on the detuning between the Bragg grating and longitudinal mode, and can be used to set the tunable laser to a desired operation point in between two mode hops. Furthermore, the voltage in the active section can be used for detecting mode-hops, and hence for extracting empirically the continuous tuning slope of the tunable laser during initialization or re-configuration intervals of the device without the need of any external equipment. This provides the possibility to continuously tune the laser from a rough starting wavelength, which can be set using a preliminary LUT, and continuously tuning towards the desired wavelength. Using these methods, and with the help of additional wavelength monitoring implemented using a 100-GHz etalon, it was possible to stabilize the III-V/polymer DBR tunable laser within ± 2.5 GHz under forced temperature variations from 15 °C to 60 °C with 0.1 °C per second over 40 periods, lasting 10 hours. The achieved results show the potential of the device proposed in this work for uncooled operation in DWDM communication systems.

5. Wavelength Setting, Stabilization, and Device Reliability

Additionally, preliminary studies on the device reliability have been performed. The achieved results show a promising operation of the III-V/polymer tunable laser device when the maximum temperature on the polymer waveguide is lower than 200°C, i.e. for 20 nm maximum tuning at 25°C, or 18 nm tuning at 45°C.

6. Study of Performance in Different Application Scenarios

Having seen the performance achievable with III-V/polymer DBR tunable lasers and some practical considerations with regards the wavelength setting, stability and long-term reliability, this chapter aims to investigate the usability of the DBR tunable laser in different application scenarios, as well as their integration as key building blocks in application-oriented PICs. Firstly, the tunable laser is used as a directly modulated optical source to evaluate its use as a wavelength-flexible transmitter in WDM-PONs, either for fiber-to-the-home (FTTH), or in the optical links between network nodes and base stations in 5G networks. Secondly, tunable I/Q transmitter PICs for coherent data-center and metro/core optical networks are presented, comprising the tunable laser as seeder for modulators. Thirdly, a PIC comprising two tunable lasers is used for the photonic generation of THz signals by means of mixing the two generated wavelengths in a photodiode. This PIC has been tested for the photonic generation of THz carriers in high-speed wireless links, potentially usable in next-generation wireless networks, as well as for the generation of continuous frequency sweeps at THz frequencies in spectroscopy systems.

6.1 Passive optical networks for FTTH and 5G

PONs are envisioned to be key in the infrastructure of FTTH for the interconnection between end-users and central offices [3, 4], as well as in 5G networks for the interconnection between radio units and the nodes towards the optical network [6, 7]. Tunable directly modulated lasers are envisioned to be key elements in the optical transceivers used in those networks since they allow simplifying the network operation, reducing installation costs, and keeping the maintenance efforts under control [4].

In order to study the suitability of the proposed device as a tunable transmitter in a WDM-PON, large signal direct modulation was tested on the DBR tunable laser for high-speed modulation presented in

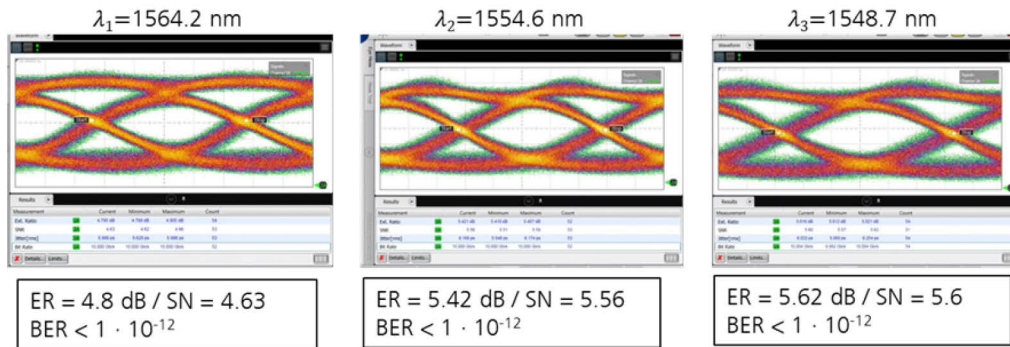


Figure 6.1. 10 Gb/s eye diagrams at three different wavelengths, obtained after propagation along 11.3 km of SMF.

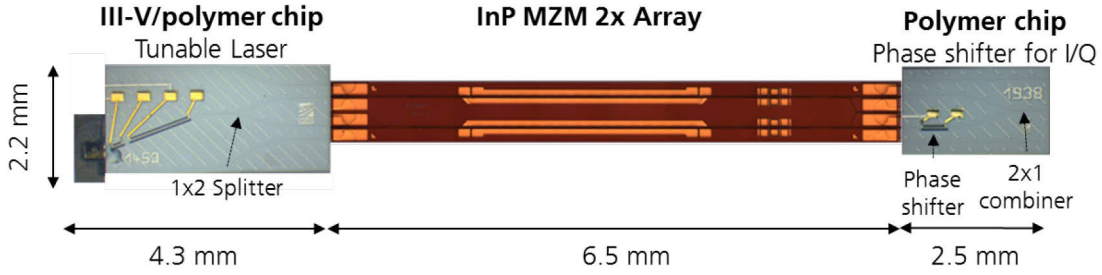


Figure 6.2. Picture of a polymer-based tunable I/Q transmitter hybrid PIC comprising the DBR tunable laser as seeder to the Mach-Zehnder modulators (MZM). The figure has been extracted from [68].

Section 4.1, which showed a 3-dB modulation bandwidth of around 8.7 GHz. The DBR laser was directly modulated using pseudo-random non-return-to-zero (NRZ) data ($2^{31}-1$), and the signal was transmitted over a single-mode fibre (SMF) link. The signal from the photodiode was connected to an oscilloscope.

Transmission experiments at 10 Gb/s were carried out using also pseudo-random NRZ data ($2^{31}-1$). For those experiments, the length of the SFM link was 11.3 km. The eye diagrams, also measured at three wavelengths with 8 nm separation, are shown in Figure 6.1. The dynamic extinction ratio was larger than 4.8 dB at the three wavelengths and the bit error rates were lower than 10^{-12} .

For SMF fiber link lengths beyond 11.3 km using a bit rate of 10 Gb/s, the chirp induced by the direct modulation degrades the BER, and error-free data transmission cannot be ensured. As discussed in Subsection 4.1.4, chirp reduction could be achieved in future design iterations by means of further exploiting the effect of the detuning.

6.2 Coherent data-center and metro/core networks

To fulfill the ever-increasing bandwidth demands on the Internet, combining advanced coherent modulation formats and DWDM is being widely explored as a potential solution in metro/core optical networks as well as inter/intra data centers. In this context, tunable lasers are envisioned to be key building blocks of coherent optoelectronic transceivers to provide the re-configuration possibility depending on the network status and the bandwidth demands. In this section, different hybrid PICs for DWDM coherent transmitters comprising the III-V/polymer DBR laser, are reviewed.

6.2.1 Tunable I/Q transmitter

The concept and performance of a tunable in-phase (I) / quadrature (Q) hybrid PIC, which comprised the III-V/polymer DBR laser as wavelength-adjustable source, was reported in [68]. My contribution to this work was the design, hybrid integration and characterization of the DBR laser, the development of the hybrid integration process with the modulators, and the development of the methodology to operate the DBR lasers for the transmission experiments. A picture of the PIC is shown in Figure 6.2. The DBR lasers featured analog design characteristics as the device showing linewidths below 300 kHz presented in Section 4.2, which featured a passive section with an effective length $L_{p,eff}$ of around 1.5 mm and a reflectivity on the Bragg grating $R_{BG} = 20\%$, and an active section with a length of $L_a = 400 \mu\text{m}$. A Y-branch was included

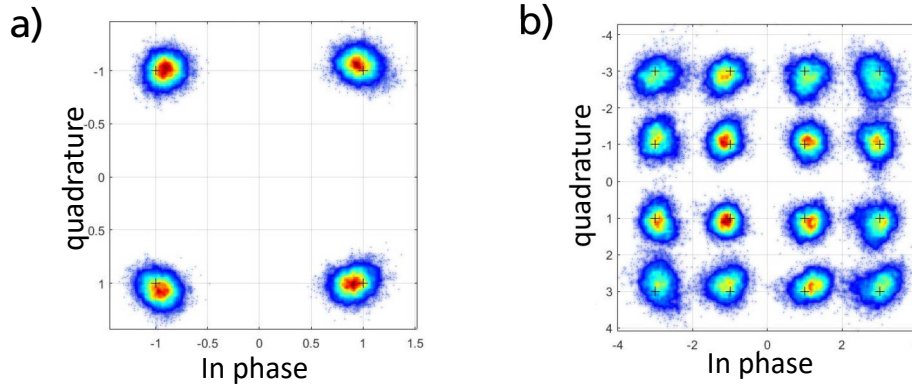


Figure 6.3. Eye diagrams for (a) QPSK and (b) 16-QAM at 20 GBaud obtained after 100 km transmission over SMF. The III-V/polymer DBR tunable laser was set to 1553.2 nm. The figures have been extracted from [68].

at the exit of the Bragg grating to butt couple the output optical signal to an InP-chip with two modulators. The modulators showed a $V_\pi=2$ V and a bandwidth of 42 GHz. To avoid reflections at the coupling interface, the InP MZM chip was anti-reflection (AR) coated towards polymer. The coupling losses between the polymer waveguides and the InP MZM chip were optimized by means of spot-size converters, and coupling losses as low as 0.8 dB showing 1-dB alignment tolerances of $\pm 0.8\mu\text{m}$ were measured [68]. A second polymer chip coupled at the output of the InP-modulator comprised a Y-junction with a 90° phase shifter on the lower arm in order to set the orthogonality between the I and Q modulation components. Notice that, with this hybrid integration approach, the InP modulators, which are the most critical elements due to their high-end specs, can be fabricated separately with specific processes to meet the stringent bandwidth requirements, which allows targeting high yields. Besides the InP active sections, all the other optical functionalities are implemented on polymer, reducing the real state of InP in the PIC and hence providing a potentially low-cost solution.

The tunable I/Q transmitter was packaged in a module together with InP-based 3-bit-selector-power-digital-to-analog-converters (3b-SPDACs) from III-V Labs, and was tested both in a laboratory environment. The device was tested using QPSK and 16-QAM modulation formats at 25 GBaud, using $2^{11}-1$ long pseudo-random binary sequences (PRBS). The output of the tunable I/Q transmitter PIC was launched to a 100-km-long SMF link and detected with a coherent receiver using a commercially-available external-cavity tunable laser with a linewidth of 100 kHz as a local oscillator (LO). Figure 6.3 (a) and (b) show the constellation diagrams at the output of the tunable I/Q transmitter at maximum OSNR for 16-QAM and QPSK signals at 25 GBaud, respectively. For the QPSK modulation format, error free operation after 100 km was achieved, while for the 16-QAM modulation format, error-free operation was achieved considering the hard-decision (HD) FEC limit with 7% overhead at a BER of 3.8×10^{-3} .

By means of further optimizing the cavity following according to the theoretical calculations shown in Subsection 4.2.3, linewidths below 10 kHz can be expected from theory. This would provide the possibility of improving the performance achieved with the tunable I/Q transceiver in order to improve the BER performance and support modulation formats beyond 16-QAM.

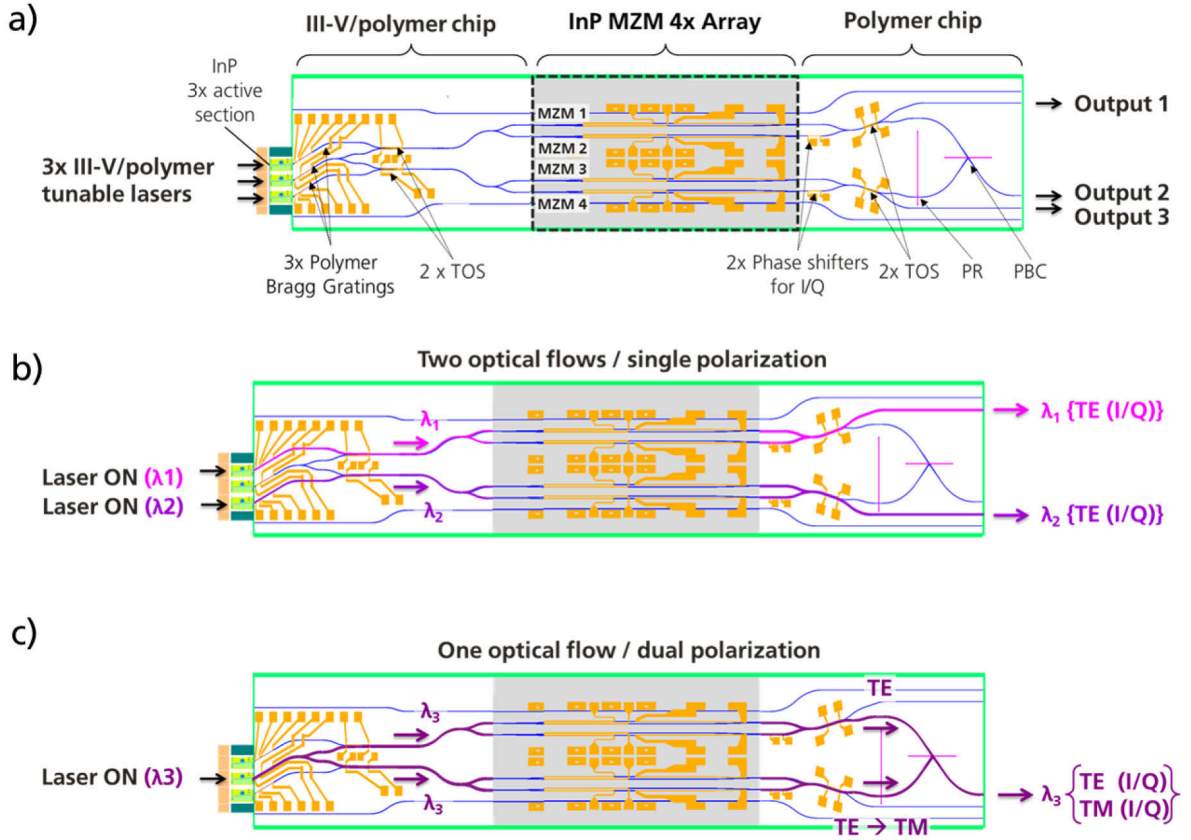


Figure 6.4. (a) Schematic of a polymer-based re-configurable multi-flow I/Q transmitter hybrid PICs. (b) Configuration for the generation of two single-polarization optical flows at two different wavelengths, and (c) configuration for the generation of one single-polarization optical-flow. The figures have been extracted from [69].

6.2.2 Re-configurable multi-wavelength I/Q transmitter

In [69], the concept of the tunable I/Q transmitter covered in the previous subsection was extended to propose a re-configurable tunable I/Q transmitter, capable of either generating and routing several single-polarization I/Q optical flows at different wavelengths, or one optical flow with polarization diversity. In Figure 6.4 (a), the schematic of the hybrid PIC is shown. From left to right, this PIC comprises three main blocks. The first block on the rear-end is a III-V/polymer chip for light generation and routing, comprising three DBR tunable lasers and two thermo-optical switches (TOS). The second block is an InP-based chip with 4 MZMs. Finally, a polymer chip at the front-end comprises phase shifters to set I/Q operation between the two upper and two lower MZMs, TOSs for light routing, and polarization handling elements such as PR and a polarization beam combiner (PBC).

The configuration of the PIC for the generation of two single-polarization (SP) optical flows is shown in Figure 6.4 (b). The upmost and lowest tunable lasers are operated at wavelengths λ_1 and λ_2 , respectively. Each of the two signals is independently guided by means of TOSs and a Y-branch to an I/Q modulator in order to generate two different optical flows. Finally, at the front-end polymer chip, the TOSs are set to guide the data signals at wavelengths λ_1 and λ_2 to the upper and lower output waveguides, respectively.

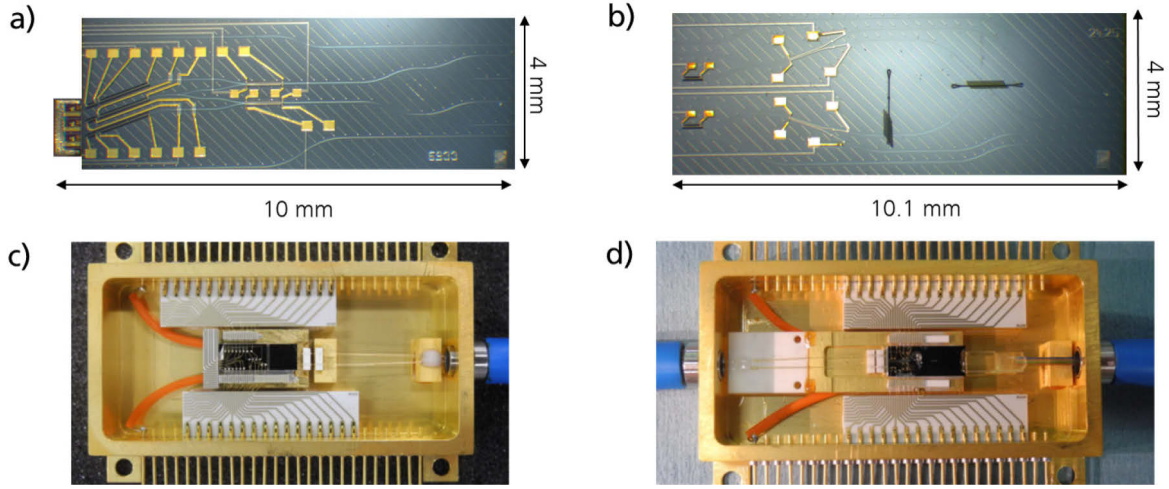


Figure 6.5. Polymer-based chips for (a) generation of multiple optical flows and (b) light routing and polarization diversity. (c) and (d) are the pictures of the packaged devices. These polymer-chips bring the re-configurability functionality to a multi-data-signal I/Q transmitter. Figures c) and d) are extracted from [70].

Figure 6.4 (c) shows the configuration for the generation of a dual-polarization (DP) optical flow. Tunable laser emitting in-plane TE polarization at wavelength λ_3 is operated, and the signal is split and guided to two I/Q modulators. At the front-end polymer chip, by means of setting the TOSs to guide both signals to the central output waveguide, the polarization of one data signal is rotated 90° from TE to TM, whereas the second signal remains unchanged at TE. Both signals are combined by means of a PBC.

The rear-end III-V/polymer chip and the front-end polymer-chip were tested in [70] in order to study the re-configurable multi-flow transmission concept. My contribution to this work was the design, hybrid integration and characterization of the rear-end and front-end chips, and the development of a methodology to operate the DBR lasers for the transmission experiments. The design parameters of the DBR tunable lasers are analog to the tunable laser presented in Section 4.2, which showed linewidths below 300 kHz. For these tests, the polymer-based chips were not hybridly integrated with the InP MZM-array in order to keep packaging efforts as low as possible for this first demonstrator. Instead, commercially available I/Q

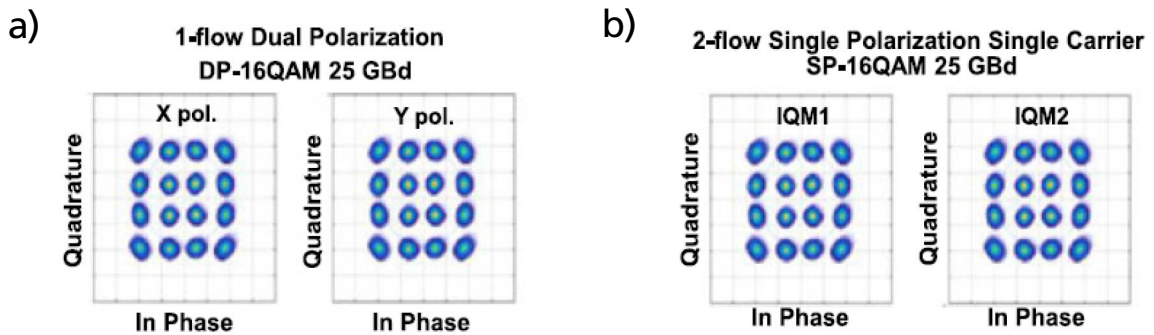


Figure 6.6. B2B constellation diagrams for with 16-QAM at 25 GBaud for different configurations of the multi-wavelength reconfigurable I/Q transmitter: (a) one dual-polarization optical flow at $\lambda_1 = 1551.65$ nm, and (b) two single-polarization optical flows at $\lambda_1 = 1551.65$ nm and $\lambda_2 = 1542.75$ nm. The figures are extracted from [70].

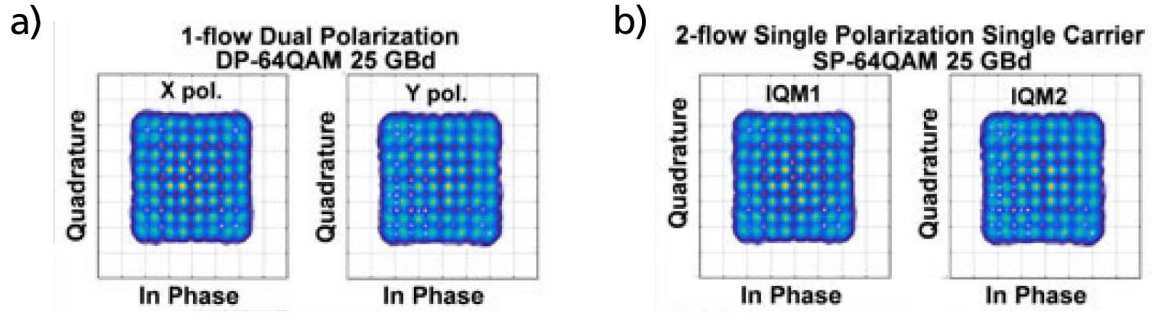


Figure 6.7. B2B constellation diagrams for with 64-QAM at 25 GBaud for different configurations of the multi-wavelength reconfigurable I/Q transmitter: (a) one dual-polarization optical flow at $\lambda_1 = 1551.65$ nm, and (b) two single-polarization optical flows at $\lambda_1 = 1551.65$ nm and $\lambda_2 = 1542.75$ nm. The figures are extracted from [70].

MZMs were used. Figure 6.5 (a) and (b) show the picture of the two polymer-based chips, whereas Figure 6.5 (c) and (d) show the picture of the packaged devices.

Different operation scenarios targeting the demonstration of the re-configuration of the transmitter were investigated. Figure 6.6 shows the constellation diagrams at 0 dBm received power measured in back-to-back (B2B) configuration for a scenario with one-flow DP and dual-flow SP. All the scenarios were operated at a symbol rate of 25 GBaud, aggregating total capacities of 200 Gb/s. For 1-flow dual-polarization, the operation wavelength λ_1 was set at 1551.65 nm, while for the case of two independent flows, the first flow was centered at λ_1 and the second one at $\lambda_2 = 1542.75$ nm. For both scenarios, and after transmission over 100 km of SMF, Q-factors above the FEC limit with 7% overhead ($\text{BER} = 3.8 \times 10^{-3}$) for received optical powers higher than -8 dBm were obtained [70].

Two further scenarios were tested in order to aggregate total capacities of 300 Gb/s. Figure 6.7 (a) shows the 64-QAM constellation diagram for one DP flow ($\lambda_1 = 1551.65$ nm), whereas Figure 6.7 (b) and for a two-flow SP configuration at wavelengths $\lambda_1 = 1551.65$ nm and $\lambda_2 = 1542.75$ nm. The different scenarios showed after a 100 km SMF link a Q-factor performance above the FEC limit with 24% overhead for received optical powers higher than -4 dBm.

As it has been mentioned above, the III-V/polymer DBR lasers featured the same design parameters as the tunable laser presented in in Section 4.2, which showed linewidths narrower than 300 kHz. As discussed in Subsection 4.2.3, linewidths below 10 kHz are theoretically achievable by means of increasing the length of the passive section and the reflectivity of the Bragg grating. This would allow improving the performance concerning BER, and potentially allow increasing the Baud rate.

6.3 THz communications for next-generation wireless systems

The next generation wireless systems, commonly known as the future 5G network, are envisioned to provide data connections above 10 Gb/s [5]. The Terahertz spectrum range (300 GHz – 3 THz) has been identified as a candidate band for the allocation of these high-speed wireless channels. The challenge of generating wireless carriers at those frequencies can be tackled by the developments in photonics for optical communications that have been carried during the last decades. More concretely, laser diodes can be used for generating optical signals, which can be mixed in a high-speed photodiode to generate a high-frequency signal. The use of tunable lasers instead of fixed-wavelength laser diodes can enable flexibility in the generation of the carrier frequencies, providing the possibility of allocating the data channel at the most

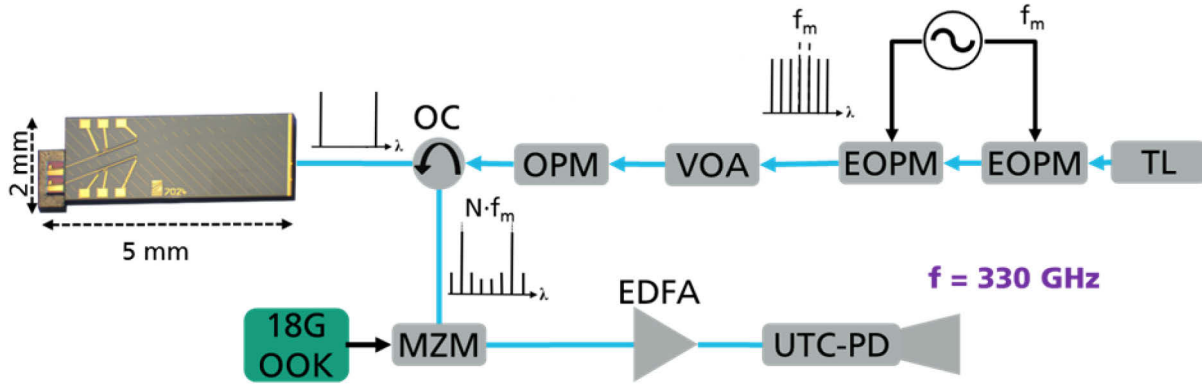


Figure 6.8. Experimental setup for the THz transmitter using a PIC comprising two III-V tunable lasers as a photonic source. TL: tunable laser, EOPM: electro-optic phase modulator, MZM: Mach-Zehnder modulator, EDFA: erbium-doped fiber amplifier, UTC-PD: uni-traveling carrier photodiode, VOA: variable optical attenuator, OPM: optical power monitor.

adequate frequency depending on the status of the wireless channel and the link requirements. In this context, the III-V/polymer DBR laser was tested for the generation of a Terahertz wireless link, and the results were reported in [71]. My contribution to this work was the design, hybrid integration and characterization of the DBR lasers, and the development of a methodology to operate the DBR lasers for the transmission experiments.

A 330 GHz carrier wave was generated using a PIC comprising two polymer-based DBR lasers, from now on referred to as dual-DBR PIC. For the generation of a high-frequency signal with high spectral purity, the two DBR lasers were phase-locked by means of optical injection locking from a master optical frequency comb generator (OFCG). For the interested reader, detailed information of the physics behind the optical injection locking can be found in [72–74]. In this section, the key results reported in [71] with regards to the photonic generation of a wireless link using dual-DBR PIC, are reviewed.

The configuration of the photonic THz transmitter is shown in Figure 6.8. The dual-DBR PIC comprised two DBR lasers with active sections with a length $L_a = 400 \mu\text{m}$, and passive sections with an effective length $L_{p,eff}$ of 1.5 mm and Bragg gratings with a reflectivity $R_{BG} = 20\%$. Notice that those are the same design characteristics as the device presented in Section 4.2, which showed linewidths below 300 kHz. The dimensions of the dual-DBR PIC were 2 mm x 5 mm. The wavelengths of the Bragg gratings were designed to be 1550 nm and 1570 nm at room temperature with the aim of allowing the generation of THz frequencies over a broad range. For the experiments presented here, the first tunable laser was set to an operation wavelength of 1549.3 nm, while the second laser was set at 1552 nm with the aim of a frequency difference of 330 GHz to generate the carrier. Both lasers were combined on-chip by means of a Y-branch. The OFCG used for optical injection locking was based on a commercially-available tunable seed laser (TL) set at 1551.05 nm with an output power of 0 dBm, followed by two cascaded electro-optic phase modulators (EOPM), modulated with a sinusoidal signal of $f_m = 27.5 \text{ GHz}$. The OFCG output was fed to the dual-DBR PIC through a variable optical attenuator (VOA) to adjust the amount of optical injection power, followed by an in-line optical power monitor (OPM), and an optical circulator (OC) to inject the frequency-comb into the dual III-V/polymer DBR PIC. The output signal from the DBR PIC was directed to a MZM via an optical circulator. Amplitude shift keying (ASK) was used as modulation format, and the

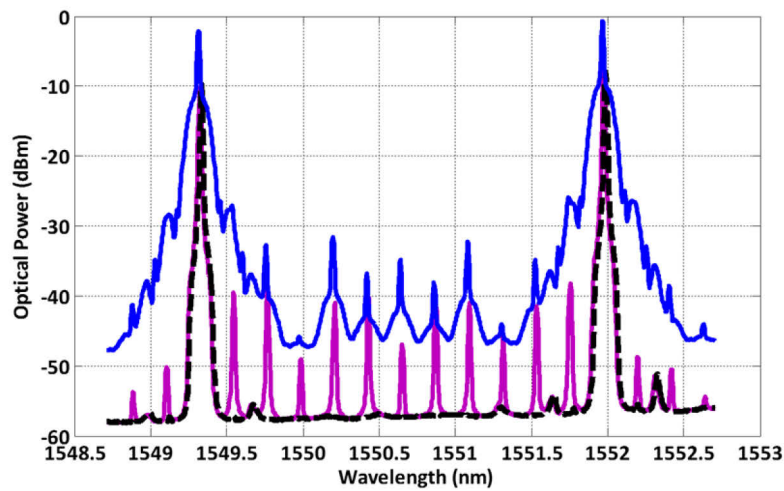


Figure 6.9. Optical spectrum of the dual-DBR PIC with 330 GHz spacing between wavelengths under different conditions: (dashed black) without injection locking, (pink) with optical injection from the external OFCG, and (blue) after the MZM modulated with a pseudo-random bit data stream at 18 Gbit/s. This figure has been extracted from [71].

data stream was a pseudo random bit sequence with a length of $2^{15} - 1$ at a bit rate of 18 Gbit/s. An erbium-doped fiber amplifier (EDFA) provided amplification of the optical signal, and a uni-travelling-carrier photodiode (UTC-PD) converted the optical signal into a 330 GHz modulated carrier wave by means of photomixing. The generated RF signal was radiated from a horn antenna. The receiver, separated 45 mm from the transmitter to ease the alignment, comprised a sub-harmonic mixer (SHM). The BER characteristics were measured in real-time using a bit error rate tester, and the eye diagrams were acquired with an oscilloscope.

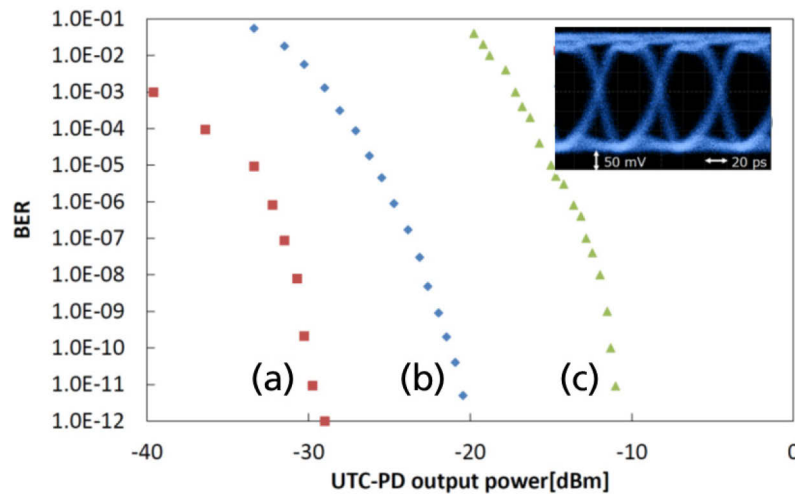


Figure 6.10. Bit error rate (BER) characteristics at 18 Gbit/s generating the 330 GHz carrier from: (a) an actively phase stabilized reference source [89], (b) the dual-DBR PIC with -8 dBm optical injection power from the OFCG, and (c) dual-DBR PIC without injection locking using direct detection at receiver. The inset shows the eye diagram under conditions of (b). This figure has been extracted from [71].

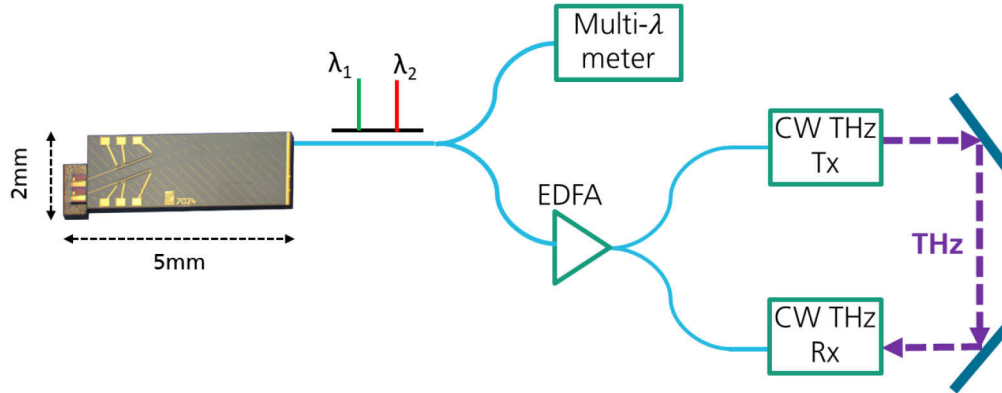


Figure 6.11. Schematic of the CW THz spectroscopy system pumped at 1.5 μm used for testing of the dual-DBR PIC as a tunable photonic source for the photonic THz generation.

Figure 6.9 shows the optical spectra of the DBR tunable laser PIC without injection locking (dashed-black line), injection locked with an optical injection power from the OCFCG of -8 dBm (pink line), and after modulating with the MZM (blue line). It can be observed that, under injection-locking condition, the Bragg gratings from the polymer-based tunable laser suppressed the comb lines with a suppression ratio larger than 30 dB. Concerning the modulated signal, it can be seen that every wavelength in the spectrum was modulated.

For the transmission experiments, the wireless link was firstly operated without injection locking on the dual-DBR PIC. With the lasers in a free-running condition, a direct detection scheme was implemented using a Schottky-barrier diode detector as a receiver for the THz signal. Using this scheme, and as it is shown In Figure 6.10 (c), a BER of 10^{-11} for a transmitted output power of -10 dBm from the UTC-PD was achieved.

In a second step, optical injection locking on the two polymer-based DBR lasers was used in order to implement a coherent transmission scheme. The local-oscillator signal at the receiver mixer was supplied from the same synthesizer used for the OFC generator (OFCG). This was done to reduce the impact of the phase noise of the synthesizer on the system, which allowed evaluating only the performance of the tunable laser PIC. As shown in Figure 6.10 (b), a BER of 10^{-11} for a transmitted output power of -20 dBm from the UTC-PD. Compared to the free-running lasers and direct detection, this provided a 10 dB sensitivity improvement.

In order to benchmark the performance of the PIC THz generator, coherent transmission experiments were performed using an actively phase-stabilized reference source described in [75]. In Figure 6.10 (a), the achieved BER curve as a function of the generated THz power by the UTC-PD is shown. As it can be observed, a 9 dB improvement with respect to the case of using the injection-locked polymer-PIC was achieved. This was attributed to the residual comb peaks present after injection locking of the PIC. In Figure 6.9 it could be seen that, after modulating the signal generated by the injection-locked polymer-based THz photonic transmitter PIC, all the residual peaks from the comb were modulated, and the different modulated peaks overlapped. This issue could be potentially avoided in a next iteration by means of implementing integrated optical filters on the PIC.

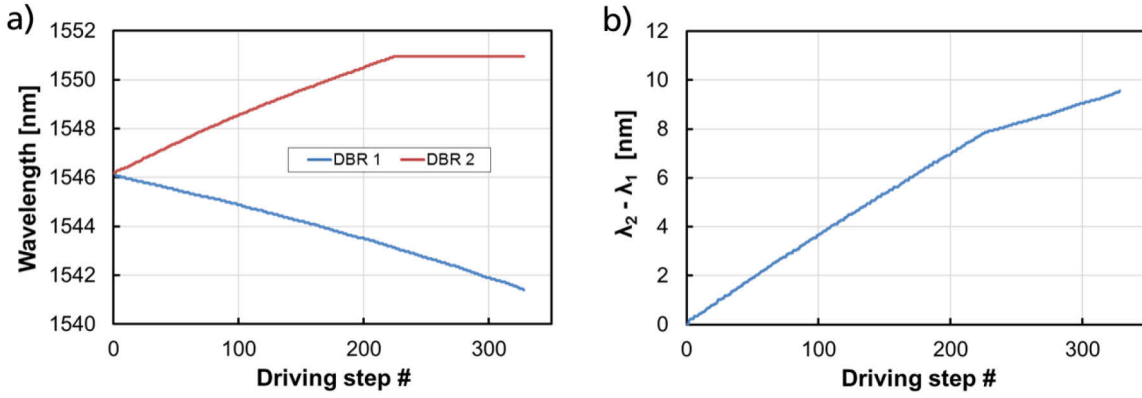


Figure 6.12. (a) Simultaneous wavelength sweep of the dual DBR source, and (b) the measured frequency difference between the two DBR lasers at different sweep steps.

6.4 THz spectroscopy systems

The use of THz frequencies for spectroscopy has also attracted a great deal of attention in applications such as biology and medical sciences, non-destructive testing, security, quality control of food and agricultural products, and global environmental monitoring [11]. In this section, the dual-DBR PIC presented in the previous section is tested as a continuously-tunable and low-cost alternative for the realization of the optical source in continuous-wave (CW) THz spectroscopy system. These results were published in [76], and my contribution to this work was the design, hybrid integration and characterization of the dual-DBR PIC, as well as the development of the methodology to tune the DBRs continuously.

In Figure 6.11, a basic schematic of the CW THz spectroscopy setup developed by the Terahertz Sensors and Systems group at Fraunhofer HHI is shown. A detailed description of the operation principle of this measurement method can be found in [77]. The THz transmitter (Tx) and receivers (Rx) have been developed by the Terahertz Sensors and Systems group at Fraunhofer HHI, and both operate at a wavelength of 1.5 μm . The THz Tx is based on photodiodes integrated with a bow-tie antenna, while the THz receiver consists of a photoconductive antenna. Detailed description of these elements can be found in [77].

For the initial experiments described here, the DBR lasers of the dual-DBR PIC featured again the same design characteristics as the device in Section 4.2, which showed a phase section with a length of $L_{PS}=600$ μm . Using equations (4.8) and (4.10), the expected maximum continuous tuning range for a maximum temperature increase in the phase and Bragg sections of T'_{max} 175°C can be calculated to be around 6 nm. One of the DBR lasers, from now on referred to as DBR 1, showed a starting wavelength of 1546 nm, while the second DBR, namely DBR 2, showed a starting wavelength at around 1565 nm.

For initialization of the system, the DBR 2 was tuned towards shorter wavelengths in order to be set at the same lasing wavelength as for DBR 1. After that, the DBR 1 was continuously tuned towards shorter wavelengths (i.e. the electrical powers on the micro-heaters were increased) while, simultaneously, the laser DBR 2 was continuously tuned towards longer wavelengths (i.e. the electrical powers on the micro-heaters were reduced). Figure 6.12 (a) shows the wavelength of each DBR achieved at driving sweep steps measured simultaneously by means of an OSA with a maximum resolution of 0.1 nm. As it can be observed, the DBR 2 reached its tuning limit after a continuous tuning of 5 nm was achieved since the phase heater

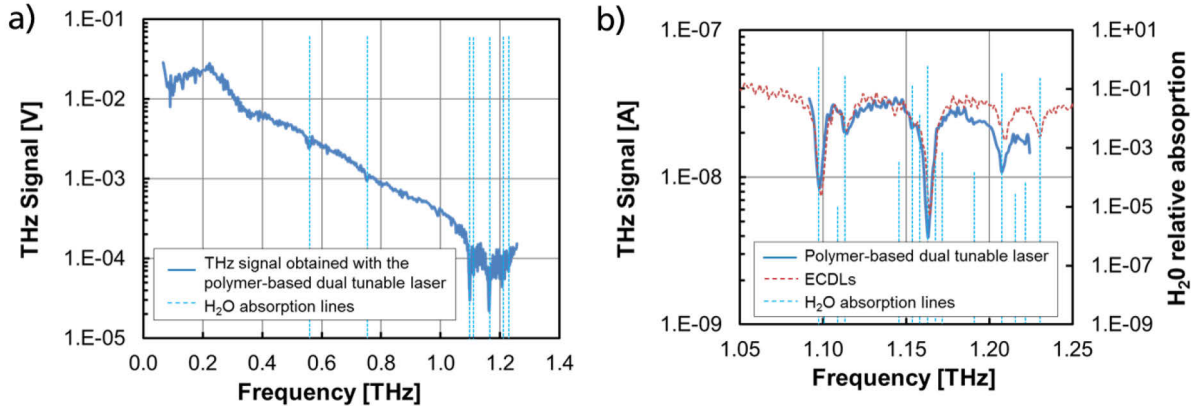


Figure 6.13. (a) Broadband CW THz scan achieved by means of photomixing using the a III-V/polymer dual-DBR PIC as wavelength-swept source, and (b) comparison between the dual-DBR PIC and commercially available ECDLs in a highly resolved THz scan for detecting water content in air.

electrical power was down to $P_{PS} = 0$ mW. It should be pointed out that the wavelength granularity observed in the tuning curve was due to the limited resolution of the OSA, and was not due to limitations in the stepping resolution of the polymer-based DBR themselves. Each DBR laser was tuned continuously over a wavelength range of more than 4.5 nm. The lower continuous tuning ranges in comparison to the expected theoretical value of 6 nm might be attributed to the setting of a non-optimal continuous tuning slope $s_{P,cont}$.

In Figure 6.12 (b), the wavelength difference between two DBRs, $\lambda_2 - \lambda_1$, is shown. A maximum wavelength difference of around 9.6 nm, which in the C-band wavelengths translates into a frequency difference of around 1.2 THz, was achieved. Notice that, after 222 driving steps, the slope of the curve decreased. This was due to the fact that DBR 2 was kept at a constant wavelength due to the phase shifter electrical power being already reduced down to 0 mW.

Figure 6.13 (a) shows the measured THz signal at the THz receiver along the sweep of the DBR PIC. As it can be seen, a frequency sweep of beyond 1.2 THz was achieved, and the detection of different H₂O absorption lines due to the air humidity was possible. It is worth noting that, by means of optimizing the laser cavity as shown in Section 4.3, continuous tuning ranges of beyond 9 nm can be potentially achieved, which would imply the possibility of generating THz scans over more than 2 THz.

In order to evaluate the resolution of the wavelength, the dual-DBR PIC was continuously tuned with very high resolution in a range between 1.090 THz and 1.223 THz. In Figure 6.13 (b), the comparison of the measured THz signal using the III-V/polymer dual DBR PIC and commercially available external cavity laser diodes (ECDLs) is presented. The vertical dashed lines indicate different H₂O absorption lines. As it can be observed, the measured amplitude using the dual DBR laser PIC overlaps well with the measurement results obtained with a commercially available ECDL, and several H₂O absorption lines can be well resolved.

6.5 Conclusions of the chapter

In this chapter, different performance tests of the III-V/polymer DBR laser have been carried out in different application fields, ranging from telecom to spectroscopy scenarios. Additionally, different III-V/polymer PICs, comprising the tunable DBR laser as a key building block, have been demonstrated.

6. Study of Performance in Different Application Scenarios

The III-V/polymer DBR has been proven to be an attractive candidate as a directly modulated tunable source in WDM-PON for FTTH and in the front-haul of 5G wireless networks. Large signal modulation tests at 10 Gb/s have shown open and clear eye diagrams. Error free transmission at 10 Gb/s over a single-mode fibre link of 11.3 km has been demonstrated.

Additionally, the use of the DBR laser in different coherent transmitters for data-center and metro/core networks has been studied. Different PICs comprising the tunable lasers as seeder to modulators in re-configurable I/Q transmitter PICs have been presented. Modulation formats up-to 64-QAM at 25 GBaud have been demonstrated in transmitter PICs capable of generating two data streams, implying an aggregated traffic of 300 Gb/s.

Furthermore, the applicability of a PIC comprising two tunable lasers (dual-DBR PIC) for the photonic generation of high-capacity wireless links for future 5G networks has been also demonstrated. The optical injection locking of DBR lasers enabled the generation of a wireless-link at 330 GHz with a bit-rate of 18 Gb/s.

The dual DBR PIC has also been used for the photonic generation of THz signals in a CW Terahertz spectroscopy system. A frequency-sweep of 1.2 THz has been achieved by means of simultaneous continuous tuning of the lasers. Various H₂O absorption lines could be identified, and resolutions similar to that with commercially available ECDLs were achieved.

7. Conclusions and Outlook

7.1 Conclusions

In this work, the implementation of C-band tunable lasers based on hybrid photonic integration approach combining InGaAsP multi-quantum-well active sections and polymer-based thermo-optically tunable structures has been investigated. The cavity structure considered is a three-section distributed Bragg reflector (DBR) laser, and tunabilities of 20 nm have demonstrated, limited by the maximum temperatures tolerated in the polymer material. The design strategies of the DBR laser in order to optimize either its high-speed modulation characteristics, linewidth, or maximum achievable continuous tuning, have been discussed.

A first design implementation targeting high-speed modulation showed a modulation bandwidth of 8.6 GHz, peak RIN values lower than -136 dB/Hz and output powers of more than 9.5 dBm. The achieved bandwidth is very similar to the one achieved with other polymer-based DBR structures reported in [26, 27] (8 GHz), and with tunable VCSELs reported in [18] (7 GHz). From the theory, it is expected that enhancing the detuning effect can further increase of the modulation bandwidth and reduce the laser chirping.

A second device targeting narrow linewidths showed linewidth values as low as 130 kHz, and output powers of 8.45 dBm. From theoretical calculations, it has been seen that, by means of increasing the effective length of the polymer section and the reflectivity of the Bragg grating, the linewidth can be potentially reduced to values down to 10 kHz. This linewidth value would be very similar to that achieved in the III-V/Si tunable laser reported in [21] (15 kHz), which make use of reflectors based on high Q-factor micro ring resonators in order to yield large effective optical lengths of the passive section.

A third design targeting maximum achievable swept-tuning has shown the possibility of 9 nm tuning without the occurrence of mode-hops, hinting to the potential use of this device as a swept wavelength source in e.g. spectroscopy applications. Theoretical developments have shown that this tuning range can be further extended by means of further increasing the length of the phase section.

Other more practical aspects such as are the wavelength stabilization and the device reliability, have been covered. It has been demonstrated that the DBR tunable laser implementation allows for fairly simple wavelength stabilization in DWDM channels, and accuracies of ± 2.5 GHz under forced temperature variations from 15 °C to 60 °C have been achieved. Additionally, preliminary reliability tests have shown the potential long-term reliability of tuning ranges of 20 nm.

Finally, the applicability of the proposed implementation has been tested in different application scenarios. Firstly, the possibility of transmitting at 10 Gb/s over fiber links of 11 km showed its potential usability in wavelength-division-multiplexed passive optical networks for FTTH and 5G networks. Secondly, hybrid photonic integrated circuits comprising the DBR lasers co-integrated with I/Q Mach-Zehnder modulators show the possibility of achieving high-order modulation formats such as 64-QAM at 25 GBaud, and hence the potential of the DBR lasers as key optical building blocks in optoelectronic

7. Conclusions and Outlook

transceivers for WDM metro/core and data-center networks. Thirdly, the possibility of using the DBR lasers for the photonic generation of THz frequencies for ultra-high-frequency wireless links showing up to 18 Gb/s data rates has been demonstrated, showing its potential use in the high-speed wireless links envisioned in future 5G networks. Finally, the photonic generation of THz frequency-sweeps for spectroscopy systems has been also investigated, showing the possibility of achieving frequency-scans along more than 1 THz.

All in all, the overall results achieved show that, with a fairly simple cavity implementation such as is a three-section DBR laser, the hybrid III-V/polymer implementation offers a versatile performance since, following the adequate design strategies, a broad range of application fields can be potentially covered.

7.2 Outlook

It is worth mentioning that the demonstrated tunable laser implementations are not only to be seen as stand-alone elements, but as building blocks of HHI's polymer-based photonic integration platform PolyBoard [78, 79]. This has been already hinted throughout this work, on which different PICs comprising the tunable DBRs have been presented. Further PICs for a broad range of applications can potentially be developed comprising other novel functionalities on HHI's PolyBoard technology such as graphene-based electro-absorption modulators [80, 81] and newly-developed optical isolators [82].

Additionally, beyond the DBR tunable laser structure discussed in this work, more complex cavity structures can be implemented in order to extend the tuning range beyond 20 nm. Those cavities can be based on e.g. polymer-based tunable sampled-grating as comb reflectors to implement the Vernier tuning effect, or by means of using ultra-widely tunable wavelength-selective filters such as grating assisted directional couplers [83]. Initial III-V/polymer implementations based on these structures have been reported in [84], work to which I have contributed. Tuning ranges beyond 90 nm have been demonstrated, showing the potential of the hybrid III-V/polymer integration for ultra-broadband tunable laser sources. Notice that those new implementations can also be modelled using the theory of external cavity semiconductor lasers presented in Chapter 2 of this work, which would allow optimizing their performance for the targeted application.

Furthermore, due to the transparency of polymer materials down to the visible range, tunable lasers in the visible might be developed parting from the theory and experimental results in the C-band presented on this work. This would open the polymer-based hybrid photonic integration technology to a completely new range of applications, since the availability of PICs in the visible wavelengths comprising light sources is a cornerstone in life sciences and emerging quantum technologies.

A. List of Patents and Publications

The following patents and scientific publications related to this work have been published.

A.1. Patents

M. Happach, D. de Felipe, M. Schell, and N. Keil, “Laser arrangement, method for controlling a laser and measuring method,” Applied for by Fraunhofer-Gesellschaft zur Förderung der angewandten Forschung e.V. on 10-02-2017, App. no. WO 2017/144462 A1, Priority date 12-02-2016.

A.2. Articles in journals

Groumas, Z. Zhang, V. Katopodis, Ch. Kouloumentas, D. de Felipe, R. Dinu, E. Miller, J. Mallari, G. Cangini, N. Keil, H. Avramopoulos, and N. Grote, “Complex monolithic and InP hybrid integration on high bandwidth electro-optic polymer platform,” *Optics Letters*, vol. 37, issue 16, pp. 3465-3467, August 2012.

A. Liu, Z. Zhang, D. de Felipe, N. Keil, and N. Grote, “Power-Efficient Thermo-Optic Tunable Filters Based on Polymeric Waveguide Bragg Gratings,” *IEEE Photonics Technology Letters*, vol. 26, issue 3, February 2014.

D. de Felipe, Z. Zhang, W. Brinker, M. Kleinert, A. Maese Novo, C. Zawadzki, M. Moehrle, and N. Keil, “Polymer-Based External Cavity Lasers: Tuning Efficiency, Reliability, and Polarization Diversity,” *IEEE Photonics Technology Letters*, vol. 26, issue 14, pp. 1391 – 1394, July 2014.

T. Mueller, A. Maese-Novo, Z. Zhang, A. Polatynski, D. de Felipe, M. Kleinert, W. Brinker, C. Zawadzki, and N. Keil, “Switchable dual-polarization external cavity tunable laser,” *Opt. Lett.* 40, 447-450, February 2015.

Z. Zhang, D. de Felipe, W. Brinker, M. Kleinert, A. Maese-Novo, M. Moehrle, C. Zawadzki, and N. Keil, “C/L-Band Colorless ONU Based on Polymer Bidirectional Optical Subassembly,” *J. Lightwave Technol.*, vol. 33, no. 6, March 2015.

Z. Zhang, D. de Felipe, V. Katopodis, P. Groumas, C. Kouloumentas, H. Avramopoulos, J.-Y. Dupuy 3, A. Konczykowska, A. Dede, A. Beretta, A. Vannucci, G. Cangini 5, R. Dinu 5, D. Schmidt, M. Moehrle, P. Runge, J.-H. Choi, H.-G. Bach, N. Grote, N. Keil, and Martin Schell, “Hybrid Photonic Integration on a Polymer Platform,” *Photonics*, 2(3), 1005-1026, September 2015.

V. Katopodis, D. de Felipe, C. Tsokos, P. Groumas, M. Spyropoulou, A. Beretta, A. Dede, M. Quagliotti, A. Pagano, A. Vannucci, N. Keil, H. Avramopoulos, and Ch. Kouloumentas, "Multi-Flow Transmitter Based on Polarization and Optical Carrier Management on Optical Polymers," in *IEEE Photonics Technology Letters*, vol. 28, no. 11, pp. 1169-1172, June 1, 2016. doi: 10.1109/LPT.2016.2533663.

D. de Felipe, M. Kleinert, Zawadzki, Crispin, A. Polatynski, G. Irmscher, W. Brinker, M. Moehrle, H.-G. Bach, N. Keil, and M. Schell, "Recent Developments in Polymer-Based Photonic Components for Disruptive Capacity Upgrade in Data Centers," *J. Lightwave Technol.*, vol. 35, no. 4, pp. 683–689, 2017.

Magnus Happach, David de Felipe, Victor Nicolai Friedhoff, Moritz Kleinert, Crispin Zawadzki, W. Rehbein, Walter Brinker, Martin Möhrle, Norbert Keil, Werner Hofmann, and Martin Schell, "Temperature-Tolerant Wavelength-Setting and -Stabilization in a Polymer-Based Tunable DBR Laser," *J. Lightwave Technol.* 35, 1797-1802 (2017).

V. Katopodis, H. Mardoyan, C. Tsokos, D. Felipe, A. Konczykowska, P. Groumas, M. Spyropoulou, L. Gounaridis, P. Jenneve, F. Boitier, F. Jorge, T. K. Johansen, M. Tienforti, J.-Y. Dupuy, A. Vannucci, N. Keil, H. Avramopoulos, and C. Kouloumentas, "Multiflow Transmitter With Full Format and Rate Flexibility for Next Generation Networks," *J. Lightwave Technol.*, vol. 36, no. 17, pp. 3785–3793, 2018.

G. Carpintero, S. Hisatake, D. de Felipe, R. Guzman, T. Nagatsuma, and N. Keil, "Wireless Data Transmission at Terahertz Carrier Waves Generated from a Hybrid InP-Polymer Dual Tunable DBR Laser Photonic Integrated Circuit," *Scientific Reports*, vol. 8, no. 1, p. 3018, 2018.

A. Liu, D. de Felipe, C. Zawadzki, N. Keil, and N. Grote, "Birefringence and Reflectivity of All-Polymer Tunable Bragg Grating Filters With Microheaters," *IEEE Photon. Technol. Lett.*, vol. 30, no. 14, pp. 1325–1328, 2018

A.3. Conference contributions

D. de Felipe, Z. Zhang, F. Soares, W. Rehbein, W. Brinker, H. N. Klein, C. Zawadzki, M. Moehrle, N. Keil, and N. Grote, „Widely-Tunable Polymer Waveguide Grating Laser," ECIO 2012 Conf. Digest, April 2012.

D. de Felipe, C. Zawadzki, Z. Zhang, W. Brinker, H. N. Klein, F. Soares, M. Moehrle, N. Keil, and N. Grote, „Polymer Hybrid Integrated Devices for WDM-PON," 17th Opto-Electronics and Communications Conference (OECC 2012) Technical Digest, paper 4D3-2, July 2012.

H. Klein, C. Wagner, W. Brinker, F. Soares, D. de Felipe, Z. Zhang, C. Zawadzki, N. Keil, and M. Moehrle, "Hybrid InP-polymer 30 nm tunable DBR laser for 10 Gbit/s direct modulation in the C-Band," in Proc. IPRM Conf., Santa Barbara, CA, USA, pp. 20–21, August 2012.

N. Grote, Z. Zhang, H. Klein, D. De Felipe, W. Rehbein, W. Brinker, C. Zawadzki, N. Keil, P. Groumas, C. Kouloumentas, R. Dinu, and E. Miller, "Thermo-optically Tunable Polymer-based Waveguide Bragg-Grating Lasers for the C-Band Domain," in Latin America Optics and Photonics Conference, OSA Technical Digest (online) (Optical Society of America, 2012), paper LS4A.2, November 2012.

D. de Felipe, C. Zawadzki, Z. Zhang, W. Brinker, H. N. Klein, M. Moehrle, N. Keil, N. Grote, and M. Schell, "40 nm Tuneable Source for Colourless ONUs based on Dual Hybridly Integrated Polymer Waveguide Grating Lasers," 39th European Conference and Exhibition on Optical Communication (ECOC 2013), September 2013.

Z. Zhang, D. de Felipe, W. Brinker, M. Kleinert, A. Maese Novo, C. Zawadzki, M. Moehrle, and N. Keil, „Bi-directional, Crosstalk-Suppressed, 40-nm Wavelength Tuneable Colourless ONU on PolymerPlatform,” 40th European Conference and Exhibition on Optical Communication (ECOC 2014), paper Mo. 4.4.4, September 2014.

M. Kleinert, Z. Zhang, D. de Felipe, C. Zawadzki ; A. Maese Novo ; W. Brinker ; M. Möhrle, and N. Keil, “Recent progress in InP/polymer-based devices for telecom and data center applications,” Proc. SPIE 9365, Integrated Optics: Devices, Materials, and Technologies XIX, 93650R, February 2015.

Z. Zhang, A. M. Novo, A. Polatynski, T. Mueller, G. Irmscher, D. de Felipe, M. Kleinert, W. Brinker, C. Zawadzki, and N. Keil, "Colorless, Dual-Polarization 90° Hybrid with Integrated VOAs and Local Oscillator on Polymer Platform," in Optical Fiber Communication Conference, OSA Technical Digest (online) (Optical Society of America, 2015), paper Th1F.3, March 2015.

Z. Zhang, V. Katopodis, P. Groumas, A. Konczykowska, J. -Y. Dupuy, A. Beretta, A. Dede, E. Miller, J. H. Choi, P. Harati, F. Jorge, V. Nodjiadjim, R. Dinu, G. Cangini, A. Vannucci, D. de Felipe, A. Maese-Novo, N. Keil, H. -G. Bach, Martin Schell, H. Avramopoulos, and Ch. Kouloumentas, “Passive and electro-optic polymer photonics and InP electronics integration,” Proc. SPIE 9516, Integrated Optics: Physics and Simulations II, 951603, May 2015.

D. de Felipe ; M. Happach ; S. Nellen ; W. Brinker ; M. Kleinert ; C. Zawadzki ; M. Möhrle ; N. Keil ; T. Göbel ; K. Petermann ; M. Schell,” Hybrid polymer/InP dual DBR laser for 1.5 μm continuous-wave terahertz systems.” Proc. SPIE 9747, Terahertz, RF, Millimeter, and Submillimeter-Wave Technology and Applications IX, 974719 (February 25, 2016); doi:10.1117/12.2212989.

G. Carpintero, S. Hisatake, D. de Felipe, R. Guzman, T. Nagatsuma, N. Keil, and T. Göbel, "Photonics-based millimeter and terahertz wave generation using a hybrid integrated dual DBR polymer laser," 2016 IEEE MTT-S International Microwave Symposium (IMS), San Francisco, CA, 2016, pp. 1-3. doi: 10.1109/MWSYM.2016.7540330

V. Katopodis, M. Spyropoulou, C. Tsokos, P. Groumas, D. de Felipe, N. Keil, A. Beretta, A. Vannucci, T. K. Johansen, M. Quagliotti, A. Pagano, J.-Y. Dupuy, A. Konczykowska, C. Delezoide, H. Mardoyan, Ch. Kouloumentas, and H. Avramopoulos, "Polarization-, carrier-, and format-selectable optical flow generation based on a multi-flow transmitter using passive polymers," 2016 18th International Conference on Transparent Optical Networks (ICTON), Trento, 2016, pp. 1-4. doi: 10.1109/ICTON.2016.7550583

D. de Felipe, M. Happach, M. Kleinert, C. Zawadzki, W. Brinker, W. Rehbein, M. Moehrle, N. Keil, W. Hofmann, and M. Schell, “Polymer-based Integrated Tuneable laser with On-Chip Wavelength Locker,” ECOC 2016 Oral presentation, paper W.2.E.2, September 2016.

V. Katopodis, C. Tsokos, D. de Felipe, M. Spyropoulou, A. Konczykowska, A. Aimone, P. Groumas, J.-Y. Dupuy, F. Jorge, H. Mardoyan, R. Rios-Müller, J. Renaudier, P. Jennevé, F. Boitier, A. Pagano, M. Quagliotti, D. Roccato, T. K. Johansen, M. Tienforti, A. Vannucci, H.-G. Bach, N. Keil, H. Avramopoulos, Ch. Kouloumentas, Muriel Riet, "Optical terabit transmitter and receiver based on passive polymer and InP technology for high-speed optical connectivity between datacenters," Proc. SPIE 10561, Next-Generation Optical Communication: Components, Sub-Systems, and Systems VII, 1056107 (29 January 2018)

D. de Felipe, M. Kresse, H. Conradi, M. Kleinert, M. Nuck, C. Zawadzki, A. Scheu, W. Brinker, W. Rehbein, A. Sigmund, M. Moehrle, N. Keil, and M. Schell, “Ultra-Wide Band Tunable Lasers on the PolyBoard Polymer-Waveguide Based Photonic Integration Platform,” in 2017 European Conference on Optical Communications 2017, 2017, pp. 1–3.

B. List of Abbreviations

5G	5 th generation of wireless networks
AR	Anti-reflection
ASE	Amplified spontaneous emission
ASK	Amplitude shift keying
BER	Bit error rate
BH	Buried heterostructure
CTE	Coefficient of thermal expansion
CW	Continuous wave
DBR	Distributed Bragg reflector
DP	Dual-polarization
DWDM	Dense wavelength division multiplexing
ECDL	External cavity diode laser
EDFA	Erbium-doped fiber amplifier
EOPM	Electro-optic phase modulator
FEC	Forward error correction
FEM	Finite element method
FSR	Free spectral range
FTTH	Fiber-to-the-home
FWHM	Full width half maximum
GADC	Grating assisted directional coupler
GRIN	Graded-index lenses
HD	Heater distance
HR	High-reflective
ITU-T	Telecommunication Standardization Sector of the International Telecommunication Union
LO	Local oscillator
LUT	Lookup table
MEMS	Microelectromechanical systems
MOVPE	Metalorganic vapour-phase epitaxy
MQWM	Multi-quantum-well
MZM	Mach-Zehnder modulator

NRZ	Non-return to zero
NTC	Negative temperature coefficient
OC	Optical circulator
OFCG	Optical frequency comb generator
OPM	Optical phase modulator
OSA	Optical spectrum analyzer
OSNR	Optical signal-to-noise ratio
PBC	Polarization beam combiner
PBS	Polarization beam splitter
P-I	Power-intensity
PIC	Photonic integrated circuit
PL	Photoluminescence
PON	Passive optical network
PR	Polarization rotator
PRBS	Pseudorandom binary sequence
Q	Quadrature
QAM	Quadrature amplitude modulation
QPSK	Quadrature phase shift keying
RIN	Relative intensity noise
Rx	Receiver
SG	Sampled grating
SHM	Subharmonic mixer
SiP	Silicon photonics
SMF	Single-mode fiber
SMSR	Side-mode suppression ratio
SP	Single polarization
TE	Transverse electric
TEC	Thermoelectric cooler
TFE	Thin-film element
TL	Tunable laser
TM	Transverse magnetic
TOC	Thermo-optical coefficient
TOS	Thermo-optical switch
Tx	Transmitter
UTC-PD	Uni-Traveling-Carrier Photodiodes

UV	Ultra violet
VOA	Variable optical attenuator
WDM	Wavelength division multiplexing

C. List of Symbols

α	Linewidth enhancement factor.
α_a	Power attenuation constant in the active section.
$\alpha_{adiabatic}$	Adiabatic chirp factor.
α_{BG}	Power attenuation in the Bragg grating.
α_c	Power coupling efficiency between the active and passive sections.
α_m	Mirror losses in a solitary semiconductor laser.
$\langle \alpha_m \rangle$	Distributed mirror losses of the external cavity tunable laser.
α_p	Power attenuation constant in the passive section.
$\alpha_{transient}$	Transient chirp factor.
α_{tot}	Total losses in the laser.
β_a	Propagation constant of the active section.
$\tilde{\beta}_{BG}$	Average propagation constant along the Bragg grating.
β_p	Propagation constant of the passive section.
Γ	Transversal confinement factor in the active section.
γ	Damping rate of the external cavity tunable laser.
γ_0	Damping rate of the reference solitary semiconductor laser.
$\Delta\beta$	Deviation of the propagation constant of the considered optical wave with respect to the Bragg condition.
$\Delta\lambda_{BG}$	Induced change in the Bragg wavelength.
$\Delta\lambda_m$	Induced change in the wavelength of the longitudinal mode.
$\Delta\lambda_{cont}$	Continuous tuning range.
$\Delta\nu$	Linewidth of the external cavity tunable laser.
$\Delta\nu_0$	Linewidth of the reference solitary semiconductor laser.
$\Delta\omega_m$	Angular frequency change in the longitudinal mode with order m .
$\Delta\omega_{r,max}$	Tuning of the central angular frequency of the frequency-selective reflector in the passive section.
$\Delta T'_{PS}$	Induced temperature change in the phase shifter.
$\Delta T'_{BG}$	Induced temperature change in the Bragg grating.
$\delta\nu$	Frequency chirp of the external cavity tunable laser.

$\delta\nu_0$	Frequency chirp of the reference solitary semiconductor laser.
$\delta\omega_{\omega,m}$	Angular frequency detuning of the mode with order m with respect to the central frequency of the frequency-selective reflector in the passive section.
$\delta\omega_{m,m\pm 1}$	Angular frequency spacing between the m -th order longitudinal mode and its neighbor modes with order $m \pm 1$.
η	Overlap integral.
κ	Coupling constant.
κ_s	Gain compression coefficient.
Λ	Bragg grating period.
λ_{BG}	Bragg wavelength.
λ_m	Wavelength of the longitudinal mode with order m
μ_a	Propagation constant of the active section.
$\tilde{\mu}_{BG}$	Average effective refractive index along Bragg grating.
$\mu_{g,a}$	Group effective refractive index in the active section.
μ_{cladd}	Refractive index of the cladding polymer material.
μ_{core}	Refractive index of the core polymer material.
$\tilde{\mu}_{g,BG}$	Average group effective index along the Bragg grating.
$\mu_{g,p}$	Group effective refractive index in the passive section.
μ_p	Effective refractive index of the passive section.
ν	Frequency
ν_m	Frequency of the longitudinal mode with order m .
τ_p	Photon lifetime in the tunable laser cavity.
$\tau_{p,s}$	Photon lifetime of a solitary active section in a Fabry-Pérot configuration.
$\phi_{BG}(\omega)$	Phase shift induced by the Bragg grating.
$\phi_r(\omega)$	Phase shift induced by the passive section.
$\phi_{r2}(\omega)$	Phase of the wavelength selective reflector.
$\psi(x, y)$	Transversal optical field distribution.
ω_{BG}	Bragg frequency.
ω_m	Angular frequency of the longitudinal mode with order m .
ω_{mod}	Modulation (angular) frequency.
ω_r	Relaxation oscillation (angular) frequency of an external cavity laser.

ω_{r0}	Relaxation oscillation (angular) frequency of the reference solitary semiconductor laser.
$\omega_{r,max}$	Central angular frequency of the frequency-selective reflector in the passive section.
$\omega_{th,min}$	Angular frequency at which the threshold gain of the external cavity laser reaches its minimum value.
$\partial g_{st}/\partial n$	Differential gain.
A	Parameter of the external cavity laser that accounts for the time delay induced by the passive section.
B	Parameter of the external cavity laser that accounts for the wavelength dependence of the reflector in the passive section.
$BW_{\lambda,BG}$	Bandwidth in wavelength of the Bragg grating.
$BW_{\omega,BG}$	Bandwidth in angular frequency of the Bragg grating.
$E_{a,m}$	Energy in the active section corresponding to a certain mode with order m .
$E_m(t)$	Slow-varying electrical field amplitude of a longitudinal mode with order m .
$F = 1 + A + B$	Adiabatic chirp reduction factor.
$F_E(t)$	Langevin noise source for the electrical field.
$F_n(t)$	Langevin noise source for the number of carriers.
f_{3dB}	3-dB small signal modulation bandwidth.
f_r	Relaxation oscillation frequency of the III-V/polymer DBR laser.
f_{r0}	Relaxation oscillation frequency of the reference solitary semiconductor laser.
g	Modal gain.
g_{st}	Gain.
g_{th}	Threshold gain.
h_{core}	Height of the waveguide core.
I_a	Injection current in the active section.
I_{th}	Threshold current.
K_{xy}	Transversal spontaneous emission enhancement factor.
K_z	Longitudinal spontaneous emission enhancement factor.
k_0	Wavenumber in vacuum.

$\langle k \rangle$	Distributed wavenumber along the external cavity tunable laser.
L_a	Length of the active section.
L_{BG}	Length of the Bragg grating.
$L_{BG,eff}$	Effective length of the Bragg grating.
L_{PS}	Length of the phase shifter.
L_p	Length of the passive section between the active section and the wavelength-selective reflector.
$L_{p,eff}$	Effective length of the passive section of the cavity
L_{WG}	Aggregated length of the interconnecting passive waveguides L_{WG1} and L_{WG3}
L_{WG1}	Length of the interconnecting passive waveguide between the active section and the phase shifter.
L_{WG2}	Length of the connecting passive waveguide between the phase shifter and the Bragg grating.
m	Order of the longitudinal mode.
m_{BG}	Order of the Bragg grating.
n	Carrier density.
n_{sp}	Population inversion factor.
n_{th}	Carrier density at threshold.
P_{BG}	Electrical power applied on the Bragg grating microheater.
P_{out}	Output power from the external-cavity reflector.
P_{PS}	Electrical power applied on the phase shifter microheater.
P_{tot}	Total output power emitted by the laser (considering both end facets).
R	Effective reflectivity provided by the passive section (seen from the end of the active section).
$R(n)$	Recombination rate.
R_1	Reflectivity at the rear-end of the active section.
R_{BG}	Reflectivity of the Bragg grating at its Bragg wavelength.
R_{sp}	Spontaneous emission rate.
$r(\omega)$	Effective reflectance provided by the passive section (seen from the end of the active section).
r_1	Reflectance at the rear-end of the active section.
$r_2(\omega)$	Complex reflectance of the wavelength selective reflector.
$r_{BG}(\omega)$	Reflectance of the Bragg grating.

$\langle S_m \rangle$	Average photon number of the longitudinal mode with order m .
$S_{P,cont}$	Continuous tuning slope in electrical power.
$S_{P,corr}$	Correction slope in in electrical power for wavelength stabilization.
$S_{T,cont}$	Continuous tuning slope in temperature.
$S_{T,corr}$	Correction slope in temperature for wavelength stabilization.
T'_{BG}	Temperature variation in the Bragg grating.
T'_{env}	Change in the environmental temperature.
T'_{max}	Maximum temperature increased allowed in the Bragg grating and phase shifters.
TOC_p	Thermo-optical coefficient of the passive section.
TOC_a	Thermo-optical coefficient of the active section.
T'_{PS}	Temperature variation in the phase shifter.
V	Volume of the active section.
$v_{g,a}$	Group velocity of the active section.
$\langle v_g \rangle$	Distributed group velocity along the external cavity tunable laser.
w_{core}	Width of the waveguide core.

D. List of Physical Constants

Listed in order of first appearance in the text:

CONSTANT	SYMBOL	VALUE
Speed of light in vacuum	c	$2.99792458 \times 10^8 \text{ m/s}$
Planck constant	h	$6.626176 \times 10^{-34} \text{ J}\cdot\text{s}$
Electron charge	q	$1.6021892 \times 10^{-19} \text{ C}$

E. Parameters considered for the InGaAsP multi-quantum well active section

In the theoretical calculations performed in Chapter 4 for the calculation of the relaxation oscillation frequency f_r and linewidth $\Delta\nu$, the following values for the multi-quantum well active sections have been considered:

PARAMETER	SYMBOL	VALUE
Effective refractive index	μ_a	3.4
Effective group index	$\mu_{g,a}$	3.8
Power attenuation constant	α_a	1750 m^{-1}
Thickness of the active section	t_a	40 nm
Width of the active stripe	w_a	$2.1 \text{ }\mu\text{m}$
Confinement factor	Γ	0.1
Differential gain	dg_{st}/dn	$1.5 \times 10^{-19} \text{ m}^2$
Linewidth enhancement factor	α	2.5
Population inversion factor	n_{sp}	1.5

References

- [1] M. K. Weldon, *The Future X Network: A bell labs perspective*. Boca Raton, London: CRC Press, 2016.
- [2] J. Lee, B. Bagheri, and H.-A. Kao, "A Cyber-Physical Systems architecture for Industry 4.0-based manufacturing systems," *Manufacturing Letters*, vol. 3, pp. 18–23, 2015.
- [3] C.-H. Lee, W. V. Sorin, and B. Y. Kim, "Fiber to the Home Using a PON Infrastructure," *J. Lightwave Technol.*, vol. 24, no. 12, pp. 4568–4583, 2006.
- [4] A. Banerjee, Y. Park, F. Clarke, H. Song, S. Yang, G. Kramer, K. Kim, and B. Mukherjee, "Wavelength-division-multiplexed passive optical network (WDM-PON) technologies for broadband access: A review [Invited]," *J. Opt. Netw.*, vol. 4, no. 11, p. 737, 2005.
- [5] *5G for Europe: An Action Plan*. [Online] Available: https://ec.europa.eu/newsroom/dae/document.cfm?doc_id=17132.
- [6] A. Tzanakaki, M. Anastasopoulos, I. Berberana, D. Syrivelis, P. Flegkas, T. Korakis, D. C. Mur, I. Demirkol, J. Gutierrez, E. Grass, Q. Wei, E. Pateromichelakis, N. Vucic, A. Fehske, M. Grieger, M. Eiselt, J. Bartelt, G. Fettweis, G. Lyberopoulos, E. Theodoropoulou, and D. Simeonidou, "Wireless-Optical Network Convergence: Enabling the 5G Architecture to Support Operational and End-User Services," *IEEE Commun. Mag.*, vol. 55, no. 10, pp. 184–192, 2017.
- [7] M. Jaber, M. A. Imran, R. Tafazolli, and A. Tukmanov, "5G Backhaul Challenges and Emerging Research Directions: A Survey," *IEEE Access*, vol. 4, pp. 1743–1766, 2016.
- [8] M. H. Eiselt, J. Zou, M. Lawin, C. Wagner, and J.-P. Elbers, "Optical Transceivers for Mobile Front-Haul and PON Applications," in *2017 European Conference on Optical Communication (ECOC)*, Gothenburg, 2017, pp. 1–3.
- [9] T. Nagatsuma, S. Horiguchi, Y. Minamikata, Y. Yoshimizu, S. Hisatake, S. Kuwano, N. Yoshimoto, J. Terada, and H. Takahashi, "Terahertz wireless communications based on photonics technologies," (eng), *Optics express*, vol. 21, no. 20, pp. 23736–23747, 2013.
- [10] K. Roberts, Q. Zhuge, I. Monga, S. Gareau, and C. Laperle, "Beyond 100 Gb/s: Capacity, Flexibility, and Network Optimization," *J. Opt. Commun. Netw.*, vol. 9, no. 4, C12, 2017.
- [11] M. Tonouchi, "Cutting-edge terahertz technology," *Nature Photon*, vol. 1, no. 2, pp. 97–105, 2007.
- [12] M. de Labachellerie and G. Passadat, "Mode-hop suppression of Littrow grating-tuned lasers," (eng), *Applied optics*, vol. 32, no. 3, pp. 269–274, 1993.
- [13] M. G. Littman and H. J. Metcalf, "Spectrally narrow pulsed dye laser without beam expander," (eng), *Applied optics*, vol. 17, no. 14, pp. 2224–2227, 1978.
- [14] H. Ishii, Y. Tohmori, T. Tamamura, and Y. Yoshikuni, "Super-structure-grating (SSG) for broadly tunable DBR lasers," *IEEE Photon. Technol. Lett.*, vol. 5, no. 4, pp. 393–395, 1993.
- [15] V. Lal, J. Summers, N. Kim, S. W. Corzine, P. Evans, M. Lauermann, A. Nguyen, A. Hosseini, M. Lu, J. T. Rahn, M. R. Chitgarha, J. Zhang, J. Osenbach, T. Vallaitis, P. Samra, C. Park, M.

- Kuntz, J. Tang, C. Tsai, H. Sun, R. Schmogrow, D. Pavinski, B. Behnia, P. Mertz, T. Butrie, K.-T. Wu, M. Mitchell, M. Ziari, M. Reffle, D. Welch, and F. Kish, "Extended C-Band Tunable Multi-Channel InP-Based Coherent Transmitter PICs," *J. Lightwave Technol.*, vol. 35, no. 7, pp. 1320–1327, 2017.
- [16] A. Hosseini, M. Lu, R. Going, P. Samra, S. Amiralizadeh, A. Nguyen, J. Rahn, V. Dominic, A. Awadalla, S. Corzine, N. Kim, J. Summers, D. Gold, J. Tang, H.-S. Tsai, K. Weidner, P. Abolghasem, M. Lauermaun, J. Zhang, J. Yan, T. Vallaitis, G. Gilardi, A. Dentai, N. Modi, P. Evans, V. Lal, M. Kuntz, D. Pavinski, M. Ziari, J. Osenbach, M. Missey, A. James, T. Butrie, H. Sun, K.-T. Wu, M. Mitchell, M. Reffle, D. Welch, and F. Kish, "Extended C-band tunable multi-channel InP-based coherent receiver PICs," (eng), *Optics express*, vol. 25, no. 16, pp. 18853–18862, 2017.
- [17] C. Gierl, T. Gruendl, P. Debernardi, K. Zogal, C. Grasse, H. A. Davani, G. Böhm, S. Jatta, F. Küppers, P. Meissner, and M.-C. Amann, "Surface micromachined tunable 1.55 μm -VCSEL with 102 nm continuous single-mode tuning," (eng), *Optics express*, vol. 19, no. 18, pp. 17336–17343, 2011.
- [18] S. Paul, C. Gierl, J. Cesar, Q. Le Trung, M. Malekizandi, B. Kogel, C. Neumeyr, M. Ortsiefer, and F. Kuppers, "10-Gb/s Direct Modulation of Widely Tunable 1550-nm MEMS VCSEL," *IEEE J. Select. Topics Quantum Electron.*, vol. 21, no. 6, pp. 436–443, 2015.
- [19] C. Gierl, T. Gründl, K. Zogal, C. Grasse, H. Davani, G. Böhm, F. Küppers, P. Meissner, and M. C. Amann, "Linewidth of surface micro-machined MEMS tunable VCSELs at 1.5 μm ," in *Conference on Lasers and Electro-Optics 2012*, CTu3N.2.
- [20] G.-H. Duan, C. Jany, A. Le Liepvre, A. Accard, M. Lamponi, D. Make, P. Kaspar, G. Levaufre, N. Girard, F. Lelarge, J.-M. Fedeli, A. Descos, B. Ben Bakir, S. Messaoudene, D. Bordel, S. Menez, G. de Valicourt, S. Keyvaninia, G. Roelkens, D. van Thourhout, D. J. Thomson, F. Y. Gardes, and G. T. Reed, "Hybrid III--V on Silicon Lasers for Photonic Integrated Circuits on Silicon," *IEEE J. Select. Topics Quantum Electron.*, vol. 20, no. 4, pp. 158–170, 2014.
- [21] N. Kobayashi, K. Sato, M. Namiwaka, K. Yamamoto, S. Watanabe, T. Kita, H. Yamada, and H. Yamazaki, "Silicon Photonic Hybrid Ring-Filter External Cavity Wavelength Tunable Lasers," *J. Lightwave Technol.*, vol. 33, no. 6, pp. 1241–1246, 2015.
- [22] L. Liang, J. Hulme, R.-L. Chao, T. Komljenovic, J.-W. Shi, S. Jian, and J. E. Bowers, "A Direct Comparison between Heterogeneously Integrated Widely-Tunable Ring-Based Laser Designs," in *2017 Optical Fiber Communications Conference and Exhibition (OFC)*, W1E.1.
- [23] A. Verdier, G. de Valicourt, R. Brenot, H. Debregeas, P. Dong, M. Earnshaw, H. Carrere, and Y.-K. Chen, "Ultrawideband Wavelength-Tunable Hybrid External-Cavity Lasers," *J. Lightwave Technol.*, vol. 36, no. 1, pp. 37–43, 2018.
- [24] C. G. H. Roeloffzen, M. Hoekman, E. J. Klein, L. S. Wevers, R. B. Timens, D. Marchenko, D. Geskus, R. Dekker, A. Alippi, R. Grootjans, A. van Rees, R. M. Oldenbeuving, J. P. Epping, R. G. Heideman, K. Worhoff, A. Leinse, D. Geuzebroek, E. Schreuder, P. W. L. van Dijk, I. Visscher, C. Taddei, Y. Fan, C. Taballione, Y. Liu, D. Marpaung, L. Zhuang, M. Benelajla, and K.-J. Boller, "Low-Loss Si₃N₄ TriPleX Optical Waveguides: Technology and Applications Overview," *IEEE J. Select. Topics Quantum Electron.*, vol. 24, no. 4, pp. 1–21, 2018.
- [25] J. Park, T. Lee, D. Lee, S. Kim, and Y. Chung, "Hybrid-integrated tunable laser using polymer coupled-ring reflector," *Electron. Lett.*, vol. 44, no. 25, p. 1464, 2008.

- [26] B.-S. Choi, S. H. Oh, K. S. Kim, K.-H. Yoon, H. S. Kim, M.-R. Park, J. S. Jeong, O.-K. Kwon, J.-K. Seo, H.-K. Lee, and Y. C. Chung, "10-Gb/s direct modulation of polymer-based tunable external cavity lasers," (eng), *Optics express*, vol. 20, no. 18, pp. 20368–20375, 2012.
- [27] B.-S. Choi, J. S. Jeong, K.-H. Yoon, K. S. Kim, H. S. Kim, M.-R. Park, O.-K. Kwon, H.-K. Lee, and Y. C. Chung, "Evaluation of Chirp Reduction in Polymer-Based Tunable External-Cavity Lasers," *IEEE J. Quantum Electron.*, vol. 51, no. 1, pp. 1–15, 2015.
- [28] M. Schell, Z. Zhang, N. Keil, N. Mettbach, C. Zawadzki, J. Wang, D. Schmidt, W. Brinker, and N. Grote, "Polymer-based photonic toolbox: Passive components, hybrid integration and polarisation control," *IET Optoelectronics*, vol. 5, no. 5, pp. 226–232, 2011.
- [29] ChemOptics Inc., *Waveguide Resin*. [Online] Available: http://www.chemoptics.co.kr/eng/sub/product_view.php?cat_no=33&idx=16&sw=&sk=&offset=
- [30] F. G. Della Corte, G. Cocorullo, M. Iodice, and I. Rendina, "Temperature dependence of the thermo-optic coefficient of InP, GaAs, and SiC from room temperature to 600 K at the wavelength of 1.5 μm ," *Appl. Phys. Lett.*, vol. 77, no. 11, pp. 1614–1616, 2000.
- [31] S. A. Clark, B. Culshaw, E. J. Dawney, and I. E. Day, "Thermo-optic phase modulators in SIMOX material," pp. 16–24.
- [32] A. W. Elshaari, I. E. Zadeh, K. D. Jons, and V. Zwiller, "Thermo-Optic Characterization of Silicon Nitride Resonators for Cryogenic Photonic Circuits," *IEEE Photonics J.*, vol. 8, no. 3, pp. 1–9, 2016.
- [33] M. M. Rahman and M. F. Hossain, *Thermal performance analysis of polymer optical waveguides for thermo-optic applications: Cox's Bazar, Bangladesh, 21-23 October 2014*. Piscataway NJ: IEEE, 2014.
- [34] M. Takenaka and S. Takagi, "InP-based photonic integrated circuit platform on SiC wafer," (eng), *Optics express*, vol. 25, no. 24, pp. 29993–30000, 2017.
- [35] K. Hirao, K. Watari, M. E. Brito, M. Toriyama, and S. Kanzaki, "High Thermal Conductivity in Silicon Nitride with Anisotropic Microstructure," *J American Ceramic Society*, vol. 79, no. 9, pp. 2485–2488, 1996.
- [36] K. Petermann, *Laser diode modulation and noise*. Dordrecht: Kluwer, 1991.
- [37] K. Petermann, "Calculated spontaneous emission factor for double-heterostructure injection lasers with gain-induced waveguiding," *IEEE J. Quantum Electron.*, vol. 15, no. 7, pp. 566–570, 1979.
- [38] C. Henry, "Theory of spontaneous emission noise in open resonators and its application to lasers and optical amplifiers," *J. Lightwave Technol.*, vol. 4, no. 3, pp. 288–297, 1986.
- [39] R. Kazarinov and C. Henry, "The relation of line narrowing and chirp reduction resulting from the coupling of a semiconductor laser to passive resonator," *IEEE J. Quantum Electron.*, vol. 23, no. 9, pp. 1401–1409, 1987.
- [40] Govind P. Agrawal and R. Roy, "Effect of injection-current fluctuations on the spectral linewidth of semiconductor lasers,"
- [41] C. Henry, "Phase noise in semiconductor lasers," *J. Lightwave Technol.*, vol. 4, no. 3, pp. 298–311, 1986.
- [42] C. Henry, "Theory of the linewidth of semiconductor lasers," *IEEE J. Quantum Electron.*, vol. 18, no. 2, pp. 259–264, 1982.

- [43] G. P. Agrawal and C. H. Henry, "Modulation performance of a semiconductor laser coupled to an external high-Q resonator," *IEEE J. Quantum Electron.*, vol. 24, no. 2, pp. 134–142, 1988.
- [44] U. Feiste, "Optimization of modulation bandwidth in DBR lasers with detuned Bragg reflectors," *IEEE J. Quantum Electron.*, vol. 34, no. 12, pp. 2371–2379, 1998.
- [45] G. Sarlet, G. Morthier, and R. Baets, "Wavelength and mode stabilization of widely tunable SG-DBR and SSG-DBR lasers," *IEEE Photon. Technol. Lett.*, vol. 11, no. 11, pp. 1351–1353, 1999.
- [46] K. Vahala and A. Yariv, "Detuned loading in coupled cavity semiconductor lasers—effect on quantum noise and dynamics," *Appl. Phys. Lett.*, vol. 45, no. 5, pp. 501–503, 1984.
- [47] A. Yariv and M. Nakamura, "Periodic structures for integrated optics," *IEEE J. Quantum Electron.*, vol. 13, no. 4, pp. 233–253, 1977.
- [48] M. Takahashi, Y. Michitsuji, M. Yoshimura, Y. Yamazoe, H. Nishizawa, and T. Sugimoto, "Narrow spectral linewidth 1.5 μm GaInAsP/InP distributed Bragg reflector (DBR) lasers," *IEEE J. Quantum Electron.*, vol. 25, no. 6, pp. 1280–1287, 1989.
- [49] F. Koyama, Y. Suematsu, S. Arai, and T. Tawee, "1.5–1.6 μm GaInAsP/InP dynamic-single-mode (DSM) lasers with distributed Bragg reflector," *IEEE J. Quantum Electron.*, vol. 19, no. 6, pp. 1042–1051, 1983.
- [50] J. Buus, *Tunable laser diodes and related optical sources*, 2nd ed. Hoboken, New Jersey: John Wiley & Sons, 2005.
- [51] A. Liu, Z. Zhang, D. de Felipe, N. Keil, and N. Grote, "Power-Efficient Thermo-Optic Tunable Filters Based on Polymeric Waveguide Bragg Gratings," *IEEE Photon. Technol. Lett.*, vol. 26, no. 3, pp. 313–315, 2014.
- [52] ficonTEC Service GmbH, *A Modular Approach to Machines*. [Online] Available: <https://www.ficontec.com/machine-platforms/>.
- [53] Finetech GmbH & Co. KG, *Flexible Sub-micron Die Bonder*. [Online] Available: <https://www.finetech.de/products/rd-bonders/flexible-sub-micron-die-bonder/>.
- [54] G. Coppola, "Advance in thermo-optical switches: Principles, materials, design, and device structure," *Opt. Eng.*, vol. 50, no. 7, p. 71112, 2011.
- [55] K.-H. Yoon, B.-S. Choi, O.-K. Kwon, S. H. Oh, K. S. Kim, D. M. Kang, Y.-T. Han, and H. K. Lee, "Directly Modulated Tunable External Cavity Laser Transmitter Optical Sub-Assembly," *IEEE Photon. Technol. Lett.*, vol. 26, no. 1, pp. 47–49, 2014.
- [56] C. M. Miller, "Intensity modulation and noise characterization of high-speed semiconductor lasers," *IEEE LTS*, vol. 2, no. 2, pp. 44–50, 1991.
- [57] C. Harder, K. Vahala, and A. Yariv, "Measurement of the linewidth enhancement factor α of semiconductor lasers," *Appl. Phys. Lett.*, vol. 42, no. 4, pp. 328–330, 1983.
- [58] L. B. Mercer, "1/f frequency noise effects on self-heterodyne linewidth measurements," *J. Lightwave Technol.*, vol. 9, no. 4, pp. 485–493, 1991.
- [59] K. M. Abramski, W. Rodzen, P. R. Kaczmarek, L. Czurak, and A. Budnicki, "Laser diode linewidth measurements," in *Proceedings of 2003 5th International Conference on Transparent Optical Networks, 2003.*, pp. 87–90.
- [60] J. L. Zhao, R. M. Oldenbeuving, J. P. Epping, M. Hoekman, R. G. Heideman, R. Dekker, Y. Fan, K.-J. Boller, R. Q. Ji, S. M. Fu, and L. Zeng, "Narrow-linewidth widely tunable hybrid external cavity laser using Si₃N₄/SiO₂ microring resonators," in *2016 IEEE 13th International Conference on Group IV Photonics (GFP)*, pp. 24–25.

- [61] T. Komljenovic, S. Srinivasan, E. Norberg, M. Davenport, G. Fish, and J. E. Bowers, "Widely Tunable Narrow-Linewidth Monolithically Integrated External-Cavity Semiconductor Lasers," *IEEE J. Select. Topics Quantum Electron.*, vol. 21, no. 6, pp. 214–222, 2015.
- [62] U. Dürig, "Fundamentals of micromechanical thermoelectric sensors," *Journal of Applied Physics*, vol. 98, no. 4, p. 44906, <https://aip.scitation.org/doi/pdf/10.1063/1.2006968>, 2005.
- [63] M. Happach, *Concept and realization of Wavelength Locking in Tunable Lasers based on a polymer platform*. Master's thesis, Technische Universität Berlin, 2015.
- [64] M. Happach, D. de Felipe, V. N. Friedhoff, M. Kleinert, Zawadzki, Crispin, W. Rehbein, W. Brinker, M. Mohrle, N. Keil, W. Hofmann, and M. Schell, "Temperature-Tolerant Wavelength-Setting and -Stabilization in a Polymer-Based Tunable DBR Laser," *J. Lightwave Technol.*, vol. 35, no. 10, pp. 1797–1802, 2017.
- [65] M. Kawachi, "Silica waveguides on silicon and their application to integrated-optic components," *Opt Quant Electron*, vol. 22, no. 5, pp. 391–416, 1990.
- [66] ITU-T, "ITU-T Rec. G.694.1 (02/2012) Spectral grids for WDM applications: DWDM frequency grid,"
- [67] R. Dinu, D. Jin, G. Yu, B. Chen, D. Huang, H. Chen, A. Barklund, E. Miller, C. Wei, and J. Vemagiri, "Environmental Stress Testing of Electro–Optic Polymer Modulators," *J. Lightwave Technol.*, vol. 27, no. 11, pp. 1527–1532, 2009.
- [68] V. Katopodis, C. Tsokos, D. de Felipe, M. Spyropoulou, P. Groumas, A. Konczykowska, J.-Y. Dupuy, F. Jorge, H. Mardoyan, A. Pagano, M. Quagliotti, D. Roccato, A. Vannucci, N. Keil, H. Avramopoulos, C. Kouloumentas, T. K. Johansen, A. Aimone, M. Riet, H.-G. Bach, R. R. Müller, J. Renaudier, P. Jennevé, F. Boitier, and M. Tienforti, "Optical terabit transmitter and receiver based on passive polymer and InP technology for high-speed optical connectivity between datacenters," in *Proceedings Volume 10561, Next-Generation Optical Communication: Components, Sub-Systems, and Systems VII; 1056107 (2018)*, p. 6.
- [69] D. de Felipe, M. Kleinert, Zawadzki, Crispin, A. Polatynski, G. Irmscher, W. Brinker, M. Moehrle, H.-G. Bach, N. Keil, and M. Schell, "Recent Developments in Polymer-Based Photonic Components for Disruptive Capacity Upgrade in Data Centers," *J. Lightwave Technol.*, vol. 35, no. 4, pp. 683–689, 2017.
- [70] V. Katopodis, H. Mardoyan, C. Tsokos, D. Felipe, A. Konczykowska, P. Groumas, M. Spyropoulou, L. Gounaridis, P. Jenneve, F. Boitier, F. Jorge, T. K. Johansen, M. Tienforti, J.-Y. Dupuy, A. Vannucci, N. Keil, H. Avramopoulos, and C. Kouloumentas, "Multiflow Transmitter With Full Format and Rate Flexibility for Next Generation Networks," *J. Lightwave Technol.*, vol. 36, no. 17, pp. 3785–3793, 2018.
- [71] G. Carpintero, S. Hisatake, D. de Felipe, R. Guzman, T. Nagatsuma, and N. Keil, "Wireless Data Transmission at Terahertz Carrier Waves Generated from a Hybrid InP-Polymer Dual Tunable DBR Laser Photonic Integrated Circuit," *Scientific Reports*, vol. 8, no. 1, p. 3018, 2018.
- [72] R. H. Pantell, "The laser oscillator with an external signal," *Proc. IEEE*, vol. 53, no. 5, pp. 474–477, 1965.
- [73] C. J. Buczek, R. J. Freiberg, and M. L. Skolnick, "Laser injection locking," *Proc. IEEE*, vol. 61, no. 10, pp. 1411–1431, 1973.

- [74] B. Tromborg, H. Olesen, X. Pan, and S. Saito, "Transmission line description of optical feedback and injection locking for Fabry-Perot and DFB lasers," *IEEE J. Quantum Electron.*, vol. 23, no. 11, pp. 1875–1889, 1987.
- [75] Y. Yoshimizu, S. Hisatake, S. Kuwano, J. Terada, N. Yoshimoto, and T. Nagatsuma, "Wireless transmission using coherent terahertz wave with phase stabilization," *IEICE Electron. Express*, vol. 10, no. 18, p. 20130578, 2013.
- [76] D. de Felipe, M. Happach, S. Nellen, W. Brinker, M. Kleinert, C. Zawadzki, M. Möhrle, N. Keil, T. Göbel, K. Petermann, and M. Schell, "Hybrid polymer/InP dual DBR laser for 1.5 μm continuous-wave terahertz systems," in *Proc. SPIE 9747, Terahertz, RF, Millimeter, and Submillimeter-Wave Technology and Applications IX, February 25, 2016*, p. 974719.
- [77] D. Stanze, A. Deninger, A. Roggenbuck, S. Schindler, M. Schlak, and B. Sartorius, "Compact cw Terahertz Spectrometer Pumped at 1.5 μm Wavelength," *J Infrared Milli Terahz Waves*, vol. 32, no. 2, pp. 225–232, 2011.
- [78] M. Kleinert, Z. Zhang, D. de Felipe, Zawadzki, Crispin, A. Maese Novo, W. Brinker, M. Möhrle, and N. Keil, "Recent progress in InP/polymer-based devices for telecom and data center applications," in *Proc. SPIE 9365, Integrated Optics: Devices, Materials, and Technologies XIX, 93650R, February 2015*, 93650R.
- [79] M. Kleinert, D. de Felipe, Zawadzki, Crispin, W. Brinker, J. H. Choi, P. Reinke, M. Happach, S. Nellen, M. Möhrle, H.-G. Bach, N. Keil, and M. Schell, "Photonic integrated devices and functions on hybrid polymer platform," in *Proc. SPIE 10098, Physics and Simulation of Optoelectronic Devices XXV, 22 February 2017*, 100981A.
- [80] M. Kleinert, F. Herziger, P. Reinke, Zawadzki, Crispin, D. de Felipe, W. Brinker, H.-G. Bach, N. Keil, J. Maultzsch, and M. Schell, "Graphene-based electro-absorption modulator integrated in a passive polymer waveguide platform," *Opt. Mater. Express*, vol. 6, no. 6, p. 1800, 2016.
- [81] M. Kleinert, P. Reinke, H.-G. Bach, W. Brinker, C. Zawadzki, A. Dietrich, D. de Felipe, N. Keil, and M. Schell, "Gbit/s-operation of graphene electro-absorption modulators in a passive polymer waveguide platform for data and telecommunications," 101070P.
- [82] H. Conradi, D. de Felipe, M. Kleinert, M. Nuck, C. Zawadzki, A. Scheu, N. Keil, and M. Schell, "High Isolation Optical Isolator: A new Building Block for PolyBoard Photonic Integrated Circuits," in *2018 European Conference on Optical Communication (ECOC)*, pp. 1–3.
- [83] Z. Zhang, A. Maese-Novo, E. Schwartz, Zawadzki, Crispin, and N. Keil, "301-nm wavelength tunable differentially driven all-polymer optical filter," (eng), *Optics letters*, vol. 39, no. 17, pp. 5170–5172, 2014.
- [84] D. de Felipe, M. Kresse, H. Conradi, M. Kleinert, M. Nuck, C. Zawadzki, A. Scheu, W. Brinker, W. Rehbein, A. Sigmund, M. Moehrle, N. Keil, and M. Schell, "Ultra-Wide Band Tunable Lasers on the PolyBoard Polymer-Waveguide Based Photonic Integration Platform," in *2018 European Conference on Optical Communication (ECOC)*, pp. 1–3.